Biomedical Imaging Using Optical Coherence Tomography

By

Yogesh Verma

Enrolment number: PHYS03200704004

Raja Ramanna Centre for Advanced Technology

Indore-452013

India

A thesis submitted to the

Board of Studies in Physical Sciences

In partial fulfillment of requirements

For the Degree of

DOCTOR OF PHILOSOPHY

of

HOMI BHABHA NATIONAL INSTITUTE

February, 2012

Homi Bhabha National Institute

Recommendations of the Viva Voce Board

As members of the Viva Voce Board, we certify that we have read the dissertation prepared by **Yogesh Verma** entitled **"Biomedical Imaging Using Optical Coherence Tomography"** and recommend that it may be accepted as fulfilling the dissertation requirement for the Degree of Doctor of Philosophy.

Date:

Chairman – Prof. P.D. Gupta, RRCAT, Indore

Date: 29.10.12

Guide – Prof. P.K. Gupta, RRCAT, Indore

Date:

Member 1 – Prof. S. Maiti, TIFR, Mumbai

Date: 29-10-12

Member 2 – Prof. K. S. Bindra, RRCAT, Indore

Date: 29 Oct 2012

External examiner- Prof. R. M. Vasu, IISc, Banglore

Final approval and acceptance of this dissertation is contingent upon the candidate's submission of the final copies of the dissertation to HBNI.

I hereby certify that I have read this dissertation prepared under my direction and recommend that it may be accepted as fulfilling the dissertation requirement.

Date: 29.10.12

Place: RRCAT, Indore

Guide: _____

(Prof. P. K. Gupta)

STATEMENT BY AUTHOR

This dissertation has been submitted in partial fulfillment of requirements for an advanced degree at Homi Bhabha National Institute (HBNI) and is deposited in the Library to be made available to borrowers under rules of the HBNI.

Brief quotations from this dissertation are allowable without special permission, provided that accurate acknowledgement of source is made. Requests for permission for extended quotation from or reproduction of this manuscript in whole or in part may be granted by the Competent Authority of HBNI when in his or her judgment the proposed use of the material is in the interests of scholarship. In all other instances, however, permission must be obtained from the author.

(Yogesh Verma)

DECLARATION

I, hereby declare that the investigation presented in the thesis has been carried out by me. The work is original and has not been submitted earlier as a whole or in part for a degree / diploma at this or any other Institution / University.

(Yogesh Verma)

I dedicate this work

to my parents

and

my school Navodaya Vidyalaya

ACKNOWLEDGEMENTS

I am extremely thankful to my thesis guide *Dr. P. K. Gupta* for his valuable guidance, constant support, encouragement, motivation and sincere interest throughout my entire Ph.D. I am highly obliged to him for his constructive criticism, valuable suggestions, and sharing his abundance of knowledge with me. He was a great support even before he took over the responsibility for supervising me. His foresight and keen scientific intuition was absolutely vital for the progress of this work. I also thank him for proofreading of various drafts of this thesis and synopsis which helped me to present the research work in an effective manner.

I would also like to thank my technical advisor *Dr. K. D. Rao* for his suggestions, continuous support in the planning of experiments, analysis of the experimental data and scientific interpretation of the results.

Without the help and support from *Mr. H. S. Patel*, I would definitely not have got started so quickly in the lab. Thanks for helping me solve all kinds of practical problems in the lab, sharing knowledge and making me comfortable in handling of the required instrumentation.

The work here has been collaborative throughout and there is a huge array of people to thank. My heartiest thank to *Mr. M. K. Swami* for the stimulating scientific discussions at lab as well as at home. I would also like to thank my colleagues especially *Dr. M. Sharma and Mr. K. Sahu* for the discussions and suggestions during the work and for participating in some of the studies included in this dissertation.

I am thankful to *Dr. S.K. Majumder, Ms. B. Jain, Dr. A. Dube, Dr. K. Das, Dr. B. Bose, Dr. S. Raja, Mr. R. Dasgupta, Dr. A. Uppal, Mr. K. M. Khare, Ms R. Srivastava and Ms. S. Ahalawat* for fruitful scientific discussions and for creating scientific atmosphere. Also many thanks to *Mr. R. S. Verma and Ms. P. Sharma* for proof reading the thesis.

Thanks to some of the project trainees *Mr. Hrebesh, Mr. P Cherian, Mr. M. Gautam and Mr. Jimy James* for the fruitful scientific discussions and for participating in some of the studies included in this dissertation. I would also like to thank specifically *Mr. Aneesh Alex* and *Mr. M. K. Suresh* for their involvement and help in studies of imaging Zebrafish eye and brain.

Thanks to *Mr. V. Sharma* and *Mr. Sanjay Singh* for their mechanical and electronic support for day-to-day maintenance of the experimental setups.

I am grateful to former members of LBAID Dr. S. K. Mohanty, Dr. N. Ghosh, and Dr. A. Srivastava for their encouragement and fruitful discussions. Also thanks to Dr. P. Nandi and Ms. M. Bhattacharjee for their support during the experiments.

I wish to thank all other members of Laser Biomedical Applications and Instrumentation Division. I have been benefited one way or the other from their association and timely help.

I would like to thank to members of my PhD advisory committee *Dr. P. D. Gupta*, *Dr. S. Maiti, Dr. S. C. Mehendle and Dr. K. S. Bindra* for their helpful suggestions.

I am thankful to my wife *Anita* for the support and care she had taken during this work. I thank my daughters *Mannat* and *Vani* for providing cheerful atmosphere at home. Last but not the least I would like to express my sincere gratitude to my parents and to my aunts and uncles for their encouragements and never-ending love, and affection to me.

There are many people that I wish to thank who have helped me to complete this thesis. Although I do not mention you all by name, you are not forgotten - thank you all!

Yogesh Verma

Table of Contents

Synopsis

Homi Bhabha National Institute

Ph. D. PROGRAMME

1. **Name of the Constituent Institution:** Raja Ramanna Centre for Advanced Technology
2. **Name of the Student:** Yogesh Verma
3. **Enrolment No. :** PHYS03200704004
4. **Title of the Thesis:** Biomedical Imaging Using Optical Coherence Tomography
5. **Name of the Guide:** Prof. Pradeep Kumar Gupta
6. **Board of Studies:** Physical Sciences

Over the last few decades, optical techniques have received considerable attention in the field of biomedical imaging due to their ability of providing spatial resolutions down to a few micrometers and dispensing with the need of ionizing radiation [1]. Since biological medium is turbid in nature, multiple scattering blurs the image unless the tissue thickness is of the order of scattering mean free path. For optical imaging of objects embedded in a turbid medium, basically two schemes have been used. One scheme is to filter out the multiply scattered light and the other referred to as inverse approach is to map the multiply scattered light at various positions around the object. From the measured transmitted intensities for different source and detector configurations, one can in principle generate a spatial map of the absorption and scattering coefficients leading to imaging of the turbid object. While this approach has the advantage that it can provide larger imaging depth (~ few cm) the resolution is poor (limited to a few mm). In contrast the approaches which

filter out the multiply scattered light can provide higher resolution but with reduced depth of imaging. To filter out the multiple scattered photons, one can exploit the loss of coherence or depolarization of the scattered light or the fact that the scattered light emerges from the tissue in all directions and also takes longer time to emerge as compared to the unscattered (ballistic) or predominantly forward scattered (snake like) components [2]. The latter essentially travel in forward direction and so arrive earlier. Coherence gating filters out the ballistic photons having the highest image information and hence can provide images with the best resolution (down to a few μm). However, since the number of ballistic photons decreases exponentially on propagation through a turbid medium, coherence gating can only be used for imaging of transparent objects (like ocular structure) or subsurface tissue imaging. Optical coherence tomography (OCT), the approach that exploits coherence gating, has emerged as a rapid, non-contact and non-invasive optical imaging method which provides depth resolved cross-sectional images with micrometer scale resolution, which is at least an order of magnitude better than the current frontline biomedical imaging techniques like ultrasound, magnetic resonance imaging, etc. Since its development in early nineties, OCT has found widespread applications in ophthalmology, gastroenterology, dermatology, cardiovascular imaging, etc. [3].

In this thesis we describe the development of various OCT setups (time domain, Fourier domain, polarization sensitive and phase sensitive setups) and their utilization for high resolution (~10-20 μm) biomedical imaging applications such as imaging of different organs of Zebrafish, classifications of cancerous and normal breast tissue sites, non-invasive imaging of wound healing, imaging of tumor spheroids, etc.

The thesis is organized as follows:

In **Chapter 1** of the thesis we provide an overview of the optical imaging methods and highlight the advantages offered by these over the current frontline biomedical imaging modalities like ultrasound, magnetic resonance imaging, etc. We also discuss the basic theory of OCT and review the state of art of the OCT technology.

In **Chapter 2** we discuss in detail the slow speed time domain OCT (TDOCT) setup developed by us that used a motorized translation stage based optical delay line for depth scanning. The major advantage of this setup was the large scan range suitable for imaging over long path lengths as required for imaging of all the structures of eye. The axial resolution of the setup was ~10 µm limited by the bandwidth of the superluminescent diode and the 10x microscope objective used to focus the light beam on the sample surface limited the lateral resolution to ~ 20 µm. Use of the shorter focal length objective lens would improve lateral resolution but at the cost of imaging depth. To address this problem we investigated the use of tapered fiber tips (which have been shown to generate Bessel like beams with large depth of focus) for enhancing lateral resolution of OCT setup without significantly compromising the depth of imaging. The results on the use of tapered fiber tip for visualization of intracellular structures of Elodea densa plant leaf (which could not be resolved without the use of tapered fiber) are also described. Next we describe the developments carried out to obtain polarization sensitive measurements in the TDOCT setup. This was done because polarization sensitive measurements help monitor, in addition to the structural features of the tissue, the ordering of birefringent constituents (collagen, tendon, etc) of the tissue [4]. The advantage of using a single detector for the measurement of both the orthogonal polarizations and the details of the development of these setups are also presented in this Chapter.

The use of a linear translation stage based optical delay line in the slow speed TDOCT setup developed by us results in long image acquisition times. It takes about a minute to acquire an image. Faster image acquisition is needed for the use of OCT to perform *in-vivo* imaging. The development of a rapid scanning Fourier domain optical delay line and its incorporation in the reference arm, which allowed acquisition of images at 8 frames per second, is detailed in **Chapter 3.** A significant drawback of the TDOCT setup is that while all the depths of the sample are illuminated, data is collected sequentially only from one depth at a time and the back-scattered light coming from other axial locations contributes to noise. This drawback is avoided in a more sophisticated Fourier domain OCT (FDOCT) approach where the interferometric signal is optically dispersed on a linear detector array and Fourier transform of the interference spectrum is used to retrieve the axial (depth) information from all depths simultaneously. The Fourier domain approach not only improves signal to noise ratio but also eliminates the need for scanning in the reference arm and facilitates enhanced image acquisition speeds [5]. A FDOCT setup was therefore also developed by us. Details of the set up and its characterization are also presented in this Chapter.

In **Chapter 4** we describe the results of our studies on the use of TDOCT setup for non-invasive, high resolution imaging of the Zebrafish eye structures. Interest in this work stems from the fact that Zebrafish, a vertebrate model organism, is widely used to understand ocular development and a variety of diseases like retinal detachment and blindness [6]. It is known that the spherical lens of Zebra fish has a gradient refractive index profile for correcting the large spherical aberrations to be expected from a spherical lens. There exists considerable interest in determining the refractive index profile of crystalline lenses. Several techniques are employed for this purpose such as the Abbe refractometer and laser ray tracing methods. These require either sectioning or resection of

the lens. Magnetic resonance imaging (MRI) can be used for noninvasive measurement of the refractive index profile of the fisheye lens. However, it is not suitable for measuring the refractive index in the core region of the lens due to the absence of free water [6]. We have used OCT to not only image the various ocular structures of the eye such as cornea, iris, eye lens and retina with resolution of ~10 µm but also successfully demonstrated use of OCT for non-invasive measurement of the refractive index profile of the eye lens. For the latter we exploited the fact that since OCT provides direct measurement of the optical path length the gradient refractive index profile can be retrieved by iterative fitting of optical path calculated by ray tracing method with that experimentally measured using OCT at various lateral locations of the sample. The details of the measurements of ocular parameters of Zebrafish eye such as corneal and retinal thicknesses, integrated refractive index and refractive index profile of the lens were described in this Chapter. The chapter also discusses 3D optical imaging of brain with resolution significantly better than obtained by other techniques like MRI and computed tomography. Another advantage offered by OCT is that, the faster image acquisition using OCT helps avoid artifacts arising because of the motion of the sample during imaging time. The three dimensional images of Zebrafish brain reconstructed using two dimensional OCT images clearly show the major structures of the brain such as bulbus olfactorius, telencephalon, tectum opticum, cerebellum, frontal bone and eminentia granularis. These results are also presented in this Chapter.

The resolution of conventional OCT systems utilizing superluminiscent diodes (~ 10-15 µm) is not sufficient to discriminate cytological differences between the normal and the abnormal tissues. However, it is pertinent to emphasize that, most early cancers arise in epithelial tissue and are associated with alterations in both epithelial cells and stroma [7]. Since collagen fibers, the main scatterers in the stroma underlying the epithelium, are

birefringent it is expected that neoplastic changes would lead to changes in the polarization parameters which can be monitored by polarization sensitive OCT measurements. Further, there also exist significant structural differences between the normal and the abnormal tissues of different organs. For example while the normal breast tissue is composed of large lipid filled cells and hence has low attenuation the abnormal tissues exhibit dense scattering effects. These differences can also be monitored by OCT. Indeed there is a considerable interest to use OCT as intra-operative image-guidance to identify the tumor margins during surgical treatment. We have therefore investigated the use of the OCT and PSOCT setups for cancer diagnosis. While based on the intensity image, we could discriminate abnormal breast tissue sites from normal sites, the intensity images could not discriminate between malignant and the benign tumor tissue sites. However, since the collagen matrix is disordered in malignant breast tumor tissue while it is much more ordered in the fibroadenoma. The retardance images obtained from PSOCT for benign tumor could easily discriminate benign from malignant tumor. Details of these studies are presented in **Chapter 5**. Another approach used by us to discriminate normal and abnormal breast tissue sites was based on well known fact that breast tumor tissues are much stiffer than normal tissue. Indeed this forms the basis for use of the manual palpation as a diagnostic method for detection of breast tumor. We carried out OCT based elastographic measurements to measure the Young's modulus of normal, cancerous and benign breast tumor sites. The measured stiffness coefficients of benign and malignant tissue samples were found to be about two and four times higher than normal tissue samples respectively. The details of the experimental arrangements to recording the spatial displacements on application of axial loading and the results obtained are presented in this Chapter.

Multi-cellular tumor spheroids, model system for solid tumors, closely mimic their

structural, metabolic, functional, and growth patterns [8]. They are being widely used for testing of drugs being explored for treatment of solid tumors. For studying the response of tumor spheroids to drugs, the most widely used method is to measure their size and volume by microscopy. Noninvasive techniques that could periodically monitor the size and the shape of spheroids accurately are required. We have therefore explored the use of OCT to monitor the growth dynamics of tumor spheroid. The study showed that in comparisons with microscopy (which provide only 2D information) the volume estimates provided by OCT were in much better agreement with the total cell count of tumor spheroids measured using hemocytometer. Details of these measurements are also discussed in chapter 5.

Since PSOCT can monitor changes in the ordering of collagen matrix it can be used for non-invasive monitoring of the healing of wounds. In clinical practice, wound size, colour, odour, and drainage are used for gross evaluation of wound healing. These methods, however, do not provide structural information below the wound surface and can be very subjective. Histology is the standard method for obtaining the structural details of the wound tissues however biopsy is disruptive, may contaminate the wound, and also introduces a new wound, thereby prohibiting repeated assessment of the healing process in the same wound. To facilitate a timely decision for correct therapy, it is important to accurately monitor the morphological changes in the infected wounds using non-invasive tools. In **Chapter 6** we describe the use of OCT setups developed by us for monitoring wound healings in mice models and compare these results with the corresponding histological measurements.

Since OCT can provide direct measurement of the optical path length (OPL) by having prior knowledge of geometrical thickness of the medium, refractive index of the medium can be measured. However, the resolution of the OPL measured by a standard OCT setup

is limited to the coherence length of the source (a few micrometers). Therefore the accuracy of refractive index measurement by this approach for an imaging depth of a few mm is limited to ~ 10^{-3}. To further improve the accuracy of refractive index measurements the resolution with which OPL is measured needs to be improved. This can be done if phase information is retrieved in addition to the measurement of the amplitude of the interference fringes. In **Chapter 7** we describe the development of a phase contrast common path FDOCT to carry out phase sensitive OCT measurements for retrieval of nanometer scale OPL changes were beyond the restriction imposed by the coherence length of the source [9]. These precise OPL measurements, retrieved from the unwrapped phase data, were employed to demonstrate the refractive index sensing of biomimetic material (glucose solution in water having intralipid as the scattering medium) and single biological cells (keratinocyte).

In **Chapter 8** we summarize the thesis with a brief discussion on the possible future research work.

References

1. J.C. Hebden, S.R. Arridge, D.T. Delpy, “Optical imaging in medicine: 1. Experimental techniques”, Physics in Medicine and Biology, 42, 825 – 840 (1997).
2. C. Dunsby and P. M. W. French, “Techniques for depth-resolved imaging through turbid media including coherence-gated imaging”, J. Phys. D: Appl. Phys., 36, R207–R227 (2003).
3. B. Bouma, and G. Tearne, Handbook of Optical Coherence Tomography. Marcel Dekker, 2002.
4. Johannes F. de Boer and T E Milner, “Review of polarization sensitive optical coherence tomography and Stokes vector determination”, Journal of Biomedical Optics 7, 359–371 (2002)
5. R. Leitgeb, C. K. Hitzenberger, and A. F. Fercher, “Performance of Fourier domain vs. time domain optical coherence tomography”, Opt Exp, 11,889-894 (2003).
6. A. S. Glass, and R. Dham, , “The Zebrafish as model organism for eye development”. Ophthalmic Res. 36, 4–24 (2004).
7. K. Sokolov, R. Drezek, K. Gossage, and R. R. Kortum, “Reflectance spectroscopy with polarized light: is it sensitive to cellular and nuclear morphology”, Opt. Exp. 5, 302–317 (1999).
8. R. M. Sutherland, J. A. McCredie, W. R. Inch, “Growth of multicellular spheroids in tissue culture as a model of nodular carcinomas”. J Natl Cancer Inst 46,113–120 (1971).
9. M. A. Choma, A. K. Ellerbee, C. Yang, T. L. Creazzo, J. A. Izatt, “Spectral domain phase microscopy”, Opt. Letters, 30 1162-116 (2005).

List of Publications

Journals Articles

(Included in the thesis)

1. Use of common path phase sensitive spectral domain optical coherence tomography for measurement of refractive index.
   Y. Verma, P. Nandi, K. D. Rao, M. Sharma, and P. K. Gupta
   App. Opt.50, E7-E12 (2011).

2. Determination of elastic properties of resected human breast tissue samples using optical coherence tomographic elastography.
   A. Srivastava, **Y. Verma**, K. D. Rao and P. K. Gupta
   Strain 47, 75–87 (2011).

3. Imaging of human breast tissue using polarisation sensitive optical coherence tomography
   Y. Verma, M. Gautam, K. D. Rao, M. K. Swami and P. K. Gupta
   Laser Physics 21, 2143-48, (2011).

4. Non-invasive assessment of healing of bacteria infected and uninfected wounds using optical coherence tomography.
   K. Sahu, **Y. Verma**, M. Sharma, K. D. Rao, P. K. Gupta.
   Skin research and technology 16, 428 (2010)

5. Real-time *in-vivo* imaging of adult Zebrafish brain using optical coherence tomography.
   K. D. Rao, A. Alex, **Y. Verma**, S. Thampi, P. K. Gupta
   J Biophotonics. 2(5):288-91, (2009).

6. Optical coherence tomography using a tapered single mode fiber tip.
   Y. Verma, K. Divakar Rao, S. K. Mohanty, and P.K. Gupta.

Laser Physics Letters, 4, 686-689 (2007)

7. Measurement of gradient refractive index profile of crystalline lens of fisheye *in-vivo* using optical coherence tomography.
   Y. Verma, K. D. Rao, M. K. Suresh, H.S. Patel and P.K. Gupta
   Applied Physics B. 87, 607-610 (2007)

8. Imaging growth dynamics of tumor spheroids using optical coherence tomography.
   M. Sharma, **Y. Verma**, K. D. Rao, R. Nair and P. K. Gupta.
   Biotechnology Letters, 29, 273-278 (2007).

9. Non-invasive ophthalmic imaging of adult Zebrafish eye using optical coherence tomography.
   K. D. Rao, **Y. Verma**, H. S. Patel and P. K. Gupta,
   Current Science, 90, 1506, (2006).

(Not included in the thesis)

10. Single mode fiber based polarization sensitive optical coherence tomography using swept laser source.
    P. Sharma, **Y. Verma**, K. D. Rao, and P. K. Gupta,
    Journal of Optics 13, 115301-06 (2011).

11. Binary tissue classification studies on resected human breast tissues using optical coherence tomography images.
    M. Bhattachrjee, P. C. Ashok, K. D. Rao, S. K. Majumder, **Y.Verma**, and P.K.Gupta
    Journal of Innovative Optical Health Sciences, 4, 59-66 (2011).

12. Effect of He-Ne laser irradiation on hair follicle growth cycle of swiss albino mice.
    S.Shukla, K Sahu, **Y. Verma**, K. D. Rao, A. Dube, and PK Gupta.
    Skin Pharmacol Physiol, 23, 79–85 (2010).

In Edited Volumes:

1. *In-vivo* imaging of adult Zebrafish using optical coherence tomography.
   Y. Verma, K. D. Rao, A. Alex, and P. K. Gupta
   Proc. SPIE OCT Microscopy, 71390H (2008); DOI:10.1117/12.814914.

2. Effect of He-Ne laser irradiation on hair follicle growth in testosterone treated mice investigated with optical coherence tomography and histology.
   S. Shukla, **Y. Verma**, K. Sahu, K. D. Rao, A. Dube, and P. K. Gupta
   KIRAN (A Bulletin of Indian Laser Association), Vol. 19, no.1, p. 31-34, 2008.
   The paper was adjudged by ILA as one of the five best posters presented at NLS-07.

3. Tapered single mode fiber tip for high lateral resolution imaging in Optical Coherence Tomography.
   Y. Verma, K. D. Rao, S. K. Mohanty and P. K. Gupta.
   The International Biomedical Optics Symposium (BiOS) San Diego USA, SPIE p. 64360Y, 2007.

4. Optical Coherence Tomography.
   K. D. Rao, **Y. Verma** and P. K. Gupta
   KIRAN (A Bulletin of Indian Laser Association), Vol. 17, no.3, p. 69-74 , 2006.

Conference Presentations / Publications:

5. Use of common path phase sensitive spectral domain optical coherence tomography setup for refractive index measurements.
   Y. Verma, P, Nandi, K. D. Rao, M. Sharma, and P. K. Gupta.
   International conference on opto-electronics, fiber optics and photonics, held at Guwahati, December 2010.

6. Swept source based fiber optic polarization sensitive optical coherence tomography setup for tissue birefringence.
   P. Sharma, **Y. Verma**, K. D. Rao, and P. K. Gupta

International conference on opto-electronics, fiber optics and photonics, held at Guwahati, December 2010.

7. Combined Raman spectroscopy-optical coherence tomography for analysis of tissue pathology.
   S. K. Majumder, **Y. Verma**, K. Divakar Rao, M. K. Swami and P. K. Gupta
   International conference on opto-electronics, fiber optics and photonics, held at Delhi, 2009.

8. Polarization Sensitive Optical Coherence Tomography for Imaging of Human Breast Tissue.
   Y. Verma, M. Gautam, K. D. Rao, M. K. Swami and P. K. Gupta
   Fifth International Symposium on Modern Problems of Laser Physics (MPLP) August 24-30, 2008, p 199-200, Novosibirsk, Russia.

9. A new approach for mueller matrix measurement using fiber based optical coherence tomography.
   M. K. Swami, **Y. Verma**, S. Manhas, K. D. Rao, N. Ghosh and P. K. Gupta.
   International Conference on Optics within Lifesciences OWLS-10, Biophotonics Asia, July 2-4, 2008, Singapore.

10. Analysis of optical coherence tomography images for binary classification of resected human breast tissues.
    K. D. Rao, P. C. Ashok, M. Bhattacharjee, **Y. Verma**, S. K. Majumder and P. K. Gupta
    International Conference on Optics within Lifesciences OWLS-10, Biophotonics Asia, July 2-4, 2008, Singapore.

11. Polarization Sensitive Optical Coherence Tomography using a single detector and dual reference beams.
    Y. Verma, M. K. Swami, K. D. Rao and P.K. Gupta.
    Saratov Fall Meeting (SFM), September 25-28,2007, Saratov, Russia.

12. Effect of He-Ne laser irradiation on hair follicle growth in testosterone treated mice investigated with optical coherence tomography and histology.
    S. Shukla, **Y. Verma**, K. Sahu, K. D. Rao, A. Dube, and P. K. Gupta.
    Proc. DAE-BRNS National Laser Symposium, December 17-20, 2007, Vadodara.

13. Tapered single mode fiber tip for high lateral resolution imaging in Optical Coherence Tomography.
    Y. Verma, K. D. Rao, S. K. Mohanty and P. K. Gupta.
    BIOS San Diego USA 2007.

14. Non-invasive measurement of graded refractive index profile of Zebra fish lens *in-vivo* using Optical Coherence Tomography.
    Y. Verma, K. D. Rao, M. K. Suresh, H. S. Patel and P. K. Gupta.
    Eighth international conference on opto-electronics, fiber optics and photonics, held at Hyderabad, December 2006.

15. Imaging growth dynamics of tumour spheroids using optical coherence tomography.
    M. Sharma, **Y. Verma**, K. D. Rao, R. Nair and P. K. Gupta.
    Eighth international conference on opto-electronics, fiber optics and photonics, held at Hyderabad, December 2006.

Figure Captions

Table captions

CHAPTER 1: INTRODUCTION

Abstract: In this chapter we provide an overview of the optical imaging methods and highlight the advantages offered by these over the current frontline biomedical imaging modalities like ultrasound, magnetic resonance imaging, etc. We also discuss the basic theory of OCT and review the present state of the art of the OCT technology.

1.1 Biomedical optical imaging: an overview

The current frontline non-invasive biomedical imaging techniques, like X-ray imaging, Computed Tomography (CT-scan), Magnetic Resonance Imaging (MRI), Ultrasound and radioisotope imaging have limited spatial resolution (> a few hundred μm) [1]. In contrast, optical imaging techniques, that use visible and near infrared region of electromagnetic radiation, can provide micrometer scale image resolution. Further, unlike radiological techniques (X-ray imaging, CT-scan, radioisotope imaging, etc.) which use ionizing radiation, optical techniques are inherently safe. Since different constituents of tissues have distinct absorption or scattering properties at NIR wavelengths, optical techniques can also provide functional information [2]. Because of these advantages, optical techniques have received considerable attention in the field of biomedical imaging in the last few decades [3, 4, 5]. The major difficulty with optical imaging techniques is that, propagation of light through tissues is severely affected by multiple scattering which leads to image blurring [2, 4]. For this reason, thin sections of the imaging samples (thickness < mean free path for scattering) are used in microscopy. For optical imaging of thick samples, two schemes have been used. One scheme is to filter out the multiply scattered

(diffuse) light and the other referred to as inverse approach, utilizes the multiply scattered light measured at various positions around the object. From the measured transmitted intensities for different source and detector positions, one can in principle generate a spatial map of the absorption and scattering coefficients leading to imaging of the turbid object. This approach has the advantage that it can provide larger imaging depth (~ few cm) but the achievable resolution is poor (limited to ~ a few mm). In contrast, the approaches which filter out the multiply scattered light and use unscattered light can provide higher resolution but with reduced depth of imaging. To filter out multiply scattered photons, one can exploit the loss of coherence or depolarization of the scattered light or the fact that the scattered light emerges from the tissue in all directions and also takes longer time to emerge as compared to the unscattered (ballistic) or predominantly forward scattered (snake like) components. The different optical techniques used for biomedical imaging are briefly discussed in the following paragraphs:

Spatial filtering: This is one of the simplest schemes that exploit the fact that scattering of light photons often leads to a change in its direction. It is therefore possible to filter out a major fraction of the scattered light by spatial filtering technique [5]. For this, a lens is employed to produce the Fourier spectrum of the spatial distribution of light on the exit surface of a trans-illuminated object. By removing the high order frequencies using a spatial filter (an aperture), an image can be produced using only the light emitted at angles close to the normal to the exit surface of the object [2]. However, the spatial filtering technique is severely hindered by the detection of photons which are scattered back along the original direction of propagation. It is for this reason the spatial filtering techniques are used in combination with other gating techniques (time, polarization, coherence gating, etc.) in most of the systems used for imaging through scattering medium.

Time gating: This scheme exploits the fact that the multiply scattered light travels longer path in the scattering medium and thus takes longer time to emerge as compared to the unscattered components, which essentially travel in the forward direction and thus arrive earlier. Therefore, time gating offers a means to discriminate the ballistic or snake photons against the multiply scattered diffuse light. The ultrafast time gate (~ ps) required to isolate weakly scattered photons from the majority of light transmitted through thick turbid media are realized using fast detectors (streak cameras, etc.) or by the use of certain nonlinear optical phenomena to implement the fast optical shutter [4]. In the later approach, only that part of the signal which is temporally and spatially coincident with the reference pulse is detected because the reference pulse opens an intensity dependent nonlinear shutter. Therefore a time gate with the same duration as the optical pulse can be achieved [2, 4].

Polarization gating: This method exploits the fact that the multiply scattered light gets depolarized as against the ballistic components, which maintain their initial state of polarization. This method efficiently selects unscattered or weakly scattered photons by selecting the component of light which is co-polarized with the incident light. It has been shown that the surface image information is almost completely carried by the co-polarized image whereas the photons which penetrate deeper into the tissue experience more scattering events, thus tend to have a cross-polarization component also. Demos and Alfano [6] have demonstrated the improvement of image contrast in surface or slightly beneath the surface imaging by use of a linearly polarized incident light and subtracting the image acquired with cross-polarized light from the one obtained with co-polarized light. Similarly for imaging the structures underneath the skin orthogonal polarization component can be used. The orthogonal polarisation imaging has been used to image the veins and micro-vessels in the live samples [7].

Coherence gating: The coherence properties of radiation provide a powerful means to discriminate against multiply scattered light by exploiting the fact that while unscattered photons retain coherence or phase information, these properties are destroyed by multiple scattering. Coherence gating requires temporal and spatial overlap of the light reflected from the turbid medium and a reference beam to produce interference for filtering out the ballistic photons from the scattered photons. Since number of ballistic photons decay exponentially, these techniques utilize heterodyne detection to detect weak ballistic signals and achieve shot-noise limited detection. The most widely employed coherence gated technique is **Optical Coherence Tomography (OCT)**, which uses low coherence interferometry for coherence gating and heterodyne detection [8,9]. Because of its high sensitivity in excess of a 100 dB and a few micrometer axial resolution, coherence gated imaging has found widespread applications in ophthalmology, gastroenterology, dermatology, and cardiovascular imaging, etc. Motivated by the promises of this technique, several studies have been carried out in the recent past and continue in present for addressing the potential applications of this technique in biomedical imaging and its technological issues such as improvement in resolutions, sensitivity, image acquisition rate and contrast of imaging. In the following sections we provide an overview of the state-of-the-art of OCT technology.

1.2 Basic Theory of Optical Coherence Tomography

OCT has emerged as a rapid, non-contact and non-invasive optical imaging method which provides depth resolved cross-sectional images with micrometer scale resolution [10]. OCT is analogous to the ultrasound imaging except that it measures echoes and time delays of light instead of sound. Since the speed of light (~ 3×10^8 m/s) is significantly higher than the speed of sound, direct time of flight imaging is not possible with the

present electronic devices [11]. OCT relies on low coherence interferometry for indirect measurement of depth ranging of echoes. These measurements of depth ranging with light were originally used in the field of optical coherence-domain reflectometry, a 1-D distance mapping technique that was developed to localize reflections from faults in fiber-optic networks. Sooner its potential of depth resolved imaging of layered medium was recognised and applied to biological applications. The existing hardware with the telecommunications industry has allowed rapid development of OCT technology which helped to evolve it from a research technology to a practical biomedical imaging technology.

1.2.1 OCT signal

OCT systems utilize low coherence interferometry for depth resolution. The most widely used configuration involves a fiber optic Michelson interferometer and a super luminescent diode (SLD) as the low coherence source. A schematic of a Michelson interferometer is shown in Figure 1.1. The light from SLD is split into the sample and reference arms of the interferometer and the back reflections from the reference and sample arms recombine and generate interference fringes at the detector. Assuming that $E_0 = |E_0| e^{j(wt-kz)}$ is the electric field of source light and E_R and E_S are the amplitudes of the electric field from reference and sample arm respectively, the intensity at the detector at any instant can be described as:

$$I_D \propto |E_R + E_S|^2 \tag{1.1}$$

$$I_D \propto |E_R|^2 + |E_S|^2 + 2|E_R||E_S|\mathrm{Re}[\Upsilon(\tau)]\cos(\frac{2\pi}{\lambda_0} 2z) \tag{1.2}$$

where $2z$ is the round trip optical path difference between reference and sample arms, λ_0 is the wavelength of the source and $\Upsilon(\tau)$ is the complex degree of coherence of the electric fields.

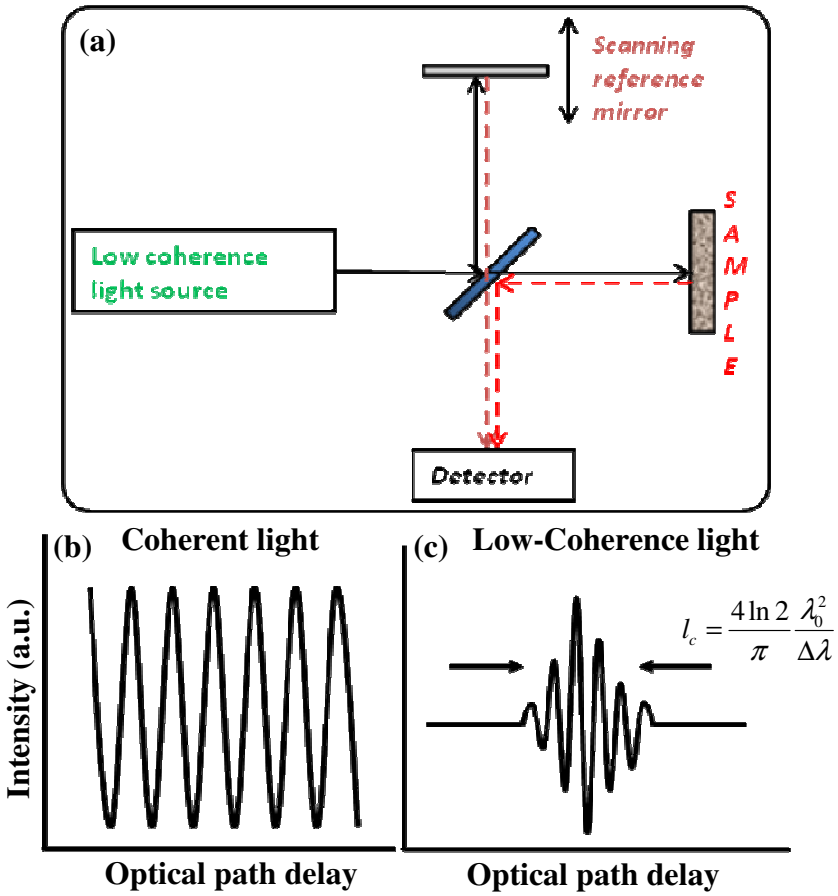

Figure 1.1: (a) Schematic of a low coherence interferometry setup. (b) Interference pattern observed for a high coherent light source. Interference is observed for longer distance due to long coherence length. (c) Interference pattern observed for a low coherent source. Interference is observed for short distance due to smaller coherence length.

The complex degree of coherence $\Upsilon(\tau)$ can be defined as the normalized autocorrelation function of the electric field emitted by the light source [12]:

$$\Upsilon(\tau) = \frac{\left\langle E^*(t)E(t+\tau)\right\rangle}{\left\langle E^*(t)E(t)\right\rangle} \tag{1.3}$$

The time delay τ between the light reaching the detector from sample and reference arms is related to the optical path difference between both the arms of the interferometer. The degree of coherence defines the temporal delay (or path delay) up to which the two light beams can interfere. The position of the reflecting interface in the sample arm can be determined with a resolution that depends on the width of the complex coherence function γ (τ) which is inversely proportional to the power spectral density according to the Wiener–Khintchine theorem [12]. From this, it can be concluded that the broader the bandwidth of the light source used, narrower is the complex degree of coherence and hence better is the resolution of the OCT system (see Figure 1.1 b & c). The coherence length ($l_c = c\tau_c$) of the source, a physical quantity, can be defined as the FWHM of the modulus of the complex temporal coherence function i.e. $\left|\Upsilon(\tau_c)\right| = \left|\Upsilon(0)\right|/2$. For the normalized Gaussian power spectral density it can be defined as:

$$l_c = \frac{4\ln 2}{\pi}\frac{\lambda_0^2}{\Delta\lambda} \tag{1.4}$$

where λ_0 is the center wavelength of the source and $\Delta\lambda$ is 3 dB spectral bandwidth of the light source. Figure 1.1 b and c show the interference patterns observed for a coherent and low coherence source respectively. For the coherent source which has long coherence length, the interference is observed for longer distance whereas for low coherence source the interference pattern is observed for a shorter distance. To achieve better axial resolution, spectrally broader sources are used in OCT system. In case of biological samples which have multiple layers, the back-scattered light comes from all the depths. However, the interference occurs only when the path lengths in reference and sample arms

match within the coherence length of the source. The reflectivity profile along the depth of the sample is acquired by varying the optical delay of reference arm mirror. The measured intensity at the detector for a varying optical path delay in reference arm is

$$I_D(t) \propto \left|E_R\right|^2 + \left|E_S\right|^2 + 2\left|E_R\right|\left|E_S\right| \mathrm{Re}[\Upsilon(\tau)] \cos(\frac{2\pi}{\lambda_0} 2z(t)) \tag{1.5}$$

Here the first and second terms of the right hand side of the equation 1.5 are the incoherent reflections of reference and sample fields respectively while the third term corresponds to the interference of the light between sample and reference fields. Optical path scanning with uniform velocity v in the reference arm therefore allows probing the sample at different depths and generates amplitude modulated interference signal with a carrier frequency determined by the speed of the reference path scanning. The intensity at the photodiode for time varying optical path length ($z = vt$) can be described as:

$$I_D(t) \propto \left|E_R\right|^2 + \left|E_S\right|^2 + 2\left|E_R\right|\left|E_S\right| \mathrm{Re}[\Upsilon(\tau)] \cos(\frac{2\pi}{\lambda_0} 2vt) \tag{1.6}$$

This carrier frequency, $f_c = 2v / \lambda_0$, also known as Doppler frequency arises due to the Doppler shift in the optical frequency by moving the reference arm mirror. The strength of the oscillating signal corresponds to the ballistic component of the reflected light. The magnitude of the back-scattered or sample reflectivity can be obtained by demodulating the amplitude modulated interference signal [8, 11]. The depth resolved reflectivity of the sample can be obtained by varying the optical path length in reference arm. This is referred to as A-scan following the ultrasound imaging terminology. Two dimensional cross-sectional images are generated by acquiring a number of sequential A-scans for numerous adjacent positions of the sample along a transversal direction. These two dimensional cross-sectional images are named as B-scan images [11]. For visualization,

the detected interference amplitude data is digitized and displayed as a two-dimensional gray-scale or false color image on the computer screen. Since our eye has limited ability to differentiate the gray levels, these images are often displayed in false color map to enhance the variation of reflectivity in the displayed images. In case of gray scale, the white color represents the highest reflectivity while the black color represents the lowest reflectivity. Similarly for false color images, the color map is chosen following the rainbow pattern where highest intensity value is represented by white or red color while the lowest intensity is represented by black or blue color. These two or three dimensional images with a few micrometer resolutions reveal the fine details of sub-surface tissue architecture and help in diagnosis of various diseases. The transparency of eye makes it an ideal candidate for OCT imaging. Owing to this, initially OCT was used for ophthalmic imaging but in a very short time span, its usage has expanded to image a range of scattering tissues like skin, teeth, oesophagus, etc. for which the depth of imaging is limited to a couple of mm only. Further, in combination with minimally invasive delivery technologies like endoscope, catheters, etc., it is also being used for *in-vivo* imaging of internal organs such as human gastrointestinal tract, cardiovascular imaging, urinary and genital tracts [13].

1.2.2 Important parameters of OCT imaging

1.2.2.1 OCT Resolutions

One of the specific advantages of OCT is that unlike microscopy and other imaging methods, in this technique the axial and transverse resolutions are decoupled. The depth resolution of the OCT system, defined as the smallest distance that can be discriminated between two tissue discontinuities, is half the coherence length of the source as the light

undergoes double pass in the sample arm. In case of a Gaussian light source, it can be expressed as:

$$\Delta z = \frac{l_c}{2} \approx 0.44 \frac{\lambda_0^2}{\Delta\lambda} \tag{1.7}$$

where λ_0 is the center wavelength of the source and $\Delta\lambda$ is full width at half maximum (FWHM) bandwidth of the light source. While the axial resolution is purely decided by the coherence length, which is inversely proportional to the source bandwidth, the transverse resolution is determined by the objective lens used to focus the incident beam on the sample surface. The transverse resolution (Δx) is defined as the waist size of the focused probe beam, which is the transverse distance up to which intensity has fallen to $1/e^2$ of the central peak value. For Gaussian beam profile the transverse resolution or focus spot can be defined as [11]:

$$\Delta x = \frac{4 f \lambda_0}{\pi D} \tag{1.8}$$

where λ_0 is the center wavelength of the light, D is the aperture of the objective lens (or beam diameter on the objective lens) and f is the focal length of the objective lens. Figure 1.2 shows the transverse resolution for high and low numerical aperture objective lenses. It also shows the trade-off between transverse resolution (Δx) and depth of field (b). The high (or low) transverse resolution can be obtained by using a large (or small) numerical aperture objective lens without affecting axial resolution. This decoupling enables a high depth resolution even at sites like the retina of the eye not accessible by high numerical aperture (NA) beams.

$$\Delta x = \frac{4\lambda}{\pi}\left(\frac{f}{d}\right)$$

$$b = 2z_R = \frac{\pi(\Delta x)^2}{2\lambda}$$

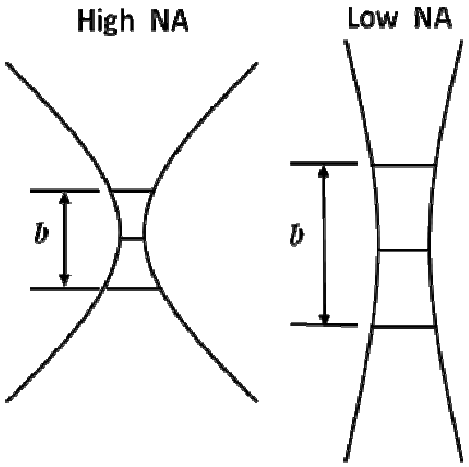

Figure 1.2: Transverse resolution for low and high numerical aperture (NA) focusing lens and the trade-off between transverse resolution vs. depth of field.

1.2.2.2 Scanning modes

There are different scanning mechanisms that can be used for OCT imaging depending upon the imaging system and application [11 - 14]. Cross-sectional images may be acquired using either depth-priority or transverse-priority scanning. In depth-priority scanning, A-scans are acquired at successive transverse positions. This is known as A-scans based B-scans. As shown in Figure 1.3 (a), in these B-scans the fast scanning is performed in depth direction while transverse scanning is significantly slower than depth scanning. Sometimes the transverse priority scanning is also used where the fast scanning is performed in transverse, either x or y direction, and slow scanning is performed in depth direction. These images are referred as transverse priority B-scans or T-scan based B-scans (shown in Figure 1.3 (b)). It is also possible to image in *enface* plane. For that the transverse image (in xy-plane) is generated by successive scanning in x and y direction for a given constant depth (shown in Figure 1.3 (c)). This scanning mechanism is similar to the confocal imaging and known as C-scan or *enface* mode of imaging. The three-dimensional tomogram of the backscattered intensity distribution within the sample can be

obtained by recording a number of B-scans along the unused third orthogonal axis of the sample.

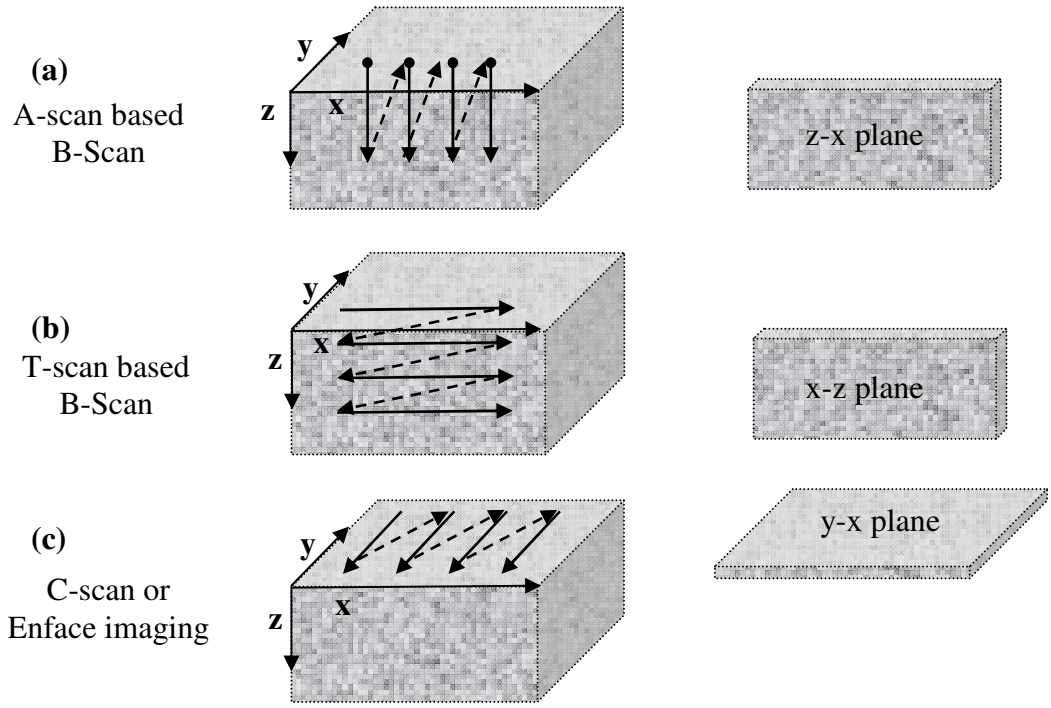

Figure 1.3: Different scanning configurations used in OCT. (a) A-scan based B-scan which results in z -x plane imaging (z-fast & x-slow scan), (b) T-scan based B-scan which results in x-z plan imaging (x-fast & z-slow scan), (c) C-scan or enface imaging which results in y-x plane imaging (y-fast & x-slow scan). Red arrows (solid) represent fast scan direction while blue arrows (dash) represent slow scan direction.

The most widely used scanning mechanism in OCT is depth priority scanning that provides cross-sectional images, analogous to generally used vertical sections of histology. However, in this geometry lateral resolution is often compromised to get deeper depth information. For imaging of samples with lateral resolution compared to that available with microscopy, *enface* imaging that supports the use of higher NA objective lenses is preferred. *Enface* mode of imaging is also suitable for coupling OCT with other imaging modalities like confocal, fluorescence microscopy, etc.

1.2.2.3 Imaging speed

Imaging speed is an important parameter of any imaging system. Depending upon the configuration of OCT imaging engine, imaging time of OCT system ranges from a few tens of seconds to a few microseconds. Since an OCT image consists of two dimensional arrangements of pixels having interference intensity information, the imaging speed is decided by the speed at which these image pixels are acquired. To generate cross-sectional images in OCT, a raster scanning is typically performed. For this both fast and slow scanning arrangements are required (see Figure 1.3). The imaging speed is ultimately determined by the speed of the fast scanner and the number of fast scans required for an OCT image. The initial OCT systems used linear translation based scanning systems which were considerably slow. The use of resonant scanner based delay line which can scan at ~ 1-4 kHz scan rate could provide video rate images but with limited ~125 fast scans (A-scans for depth priority imaging) per image. In the recent past, Fourier domain OCT imaging systems (discussed in the next section) have been developed which can provide 3D OCT imaging with ~100 kHz scan rate.

1.2.2.4 Sensitivity

Sensitivity, signal to noise ratio (SNR) and sometimes dynamic range are the terms used in OCT literature to define the system's capability to detect the smallest back-reflections originated from the tissue. These back-reflections arising due to small refractive index variation in tissue are very weak. However, interferometry enables optical heterodyne gain by multiplying the weak sample electric field with the strong reference arm electric field which results in an increase in the magnitude of the interference or oscillating term and thereby improves the sensitivity of the detection. Also the scanning reference arm generates a Doppler shift in the reference arm optical frequency. The amplitude of the

back-scattered light is measured by electronic filtering at the Doppler frequency. These features of OCT enables high sensitivity or SNR of the order of 10^{-9} -10^{-10} of incident power. Because of significant larger exponential term it is generally represented in dB scale i.e. 90-100 dB.

The SNR of an OCT system can be expressed as [11]:

$$Sensitivity(SNR) = 10\log\left(\frac{\eta P}{h\upsilon NEB}\right) \tag{1.9}$$

where η is the quantum yield of the detector, P is the detected power from sample, hυ is photon energy, and NEB is the noise equivalent bandwidth. The main sources of noise in OCT are thermal noise, shot noise, and excess intensity noise [11, 15]. Figure 1.4 shows the individual SNR for these noises as a function of reference reflectivity. It can be concluded from the figure that, while the excess intensity noise dominates for high reference mirror reflectivity (*Rr*), thermal noise dominates for low *Rr*. Between these two extreme regimes is the optimum *Rr*, at which the SNR approaches the shot-noise limit as closely as possible. The shot noise limited regime is optimum operation window for OCT systems.

A higher SNR for OCT system will lead to a greater imaging depth and better image quality of OCT images. To achieve better SNR the power from sample (or source power) should be higher and the NEB should be lower. NEB depends on the imaging speed of the system and optical bandwidth of the source ($\Delta f = v.\Delta\lambda/\lambda^2$). High imaging speed (or high speed reference scanning) and large spectral bandwidth of the source result in high NEB and thus degrade SNR. Hence there is a trade off between SNR and imaging speed of the system for a given power and bandwidth of the source. In order to achieve

high imaging speed for a given source power we need to compromise on sensitivity and/or axial resolution of the system.

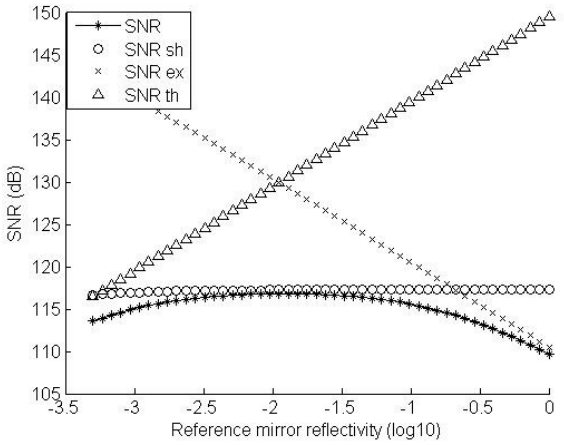

Figure 1.4: SNR as a function of reference-arm reflectivity . Also shown are the signal-to-thermal -noise ratio (SNRth), the signal-to-shot-noise ratio (SNRsh), and the signal-to-excess-intensity noise ratio (SNRex).

1.2.2.5 Imaging depth

The imaging depth of the OCT system is defined as the maximum depth, the back-scattered light coming from which can still generate an interference signal with amplitude above the noise level. This is determined by the scattering and absorption property of the sample and the SNR of the OCT system. In NIR spectral region (650 nm to 1300 nm), where tissue absorption is small the imaging depth is determined primarily by scattering. Therefore, while whole eye can be imaged (due to transparency of ocular structures), the imaging depth is limited to a couple of mm for the scattering tissue like skin. Use of source at longer wavelength will lead to larger imaging depth because scattering varies as $1/\lambda^n$ where n varies from 1 to 4 depending upon size of scatterer. Further, increase in imaging depth is possible with use of optical clearing agents like glycerol and propylene glycol which reduce scattering due to index matching [16].

1.3 OCT *vis-a-vis* other biomedical imaging techniques

In Table 1.1, we provide a comparison of resolution and imaging depth of OCT with the other imaging techniques like ultrasound, X-ray imaging, MRI, and confocal microscopy. Microscopy, a "gold standard" due to its very high resolution imaging capability, requires thin sections (a few micrometers) of tissue to reject the scattering effects. Confocal microscopy, which utilizes point illumination and spatial pinhole to reject out of focus light, can provide diffraction limited resolution with imaging depth of ~200 µm. OCT fills the gap between the confocal microscopy and ultrasound imaging. It can provide higher resolution than ultrasound and greater depth of imaging than confocal microscopy. Unlike CT-scan and MRI, OCT system is inexpensive and portable and can provide high resolution images in real time.

Table 1-1: A comparison of biomedical imaging techniques [1,11].

Imaging Technique	**Resolution**	**Depth**	**Contrast Mechanism**	**Invasiveness**	**Remark**
Microscopy	~ λ/2	Only thin sections	Absorption	Thin sections	Gold standard
Confocal Imaging	~λ/2	~200 µm	Scattering	Non-contact	Diffraction limited
OCT Imaging	~2-20 µm	~1-3 mm	Scattering	Non-contact	Portable
Clinical Ultrasound Imaging	~100 µm	~ few cms	Scattering	Contact	Portable
Clinical MRI (3-40 MHz)	~ 0.1-1mm	No restriction	H-ion	Non-contact	Bulky
Clinical CT-Scan (X-ray)	~0.1-1mm	No restriction	Absorption	Ionizing radiation	Bulky

1.4 Variants of OCT imaging

Over the last several years, in order to achieve better performance of imaging system, several configurations of OCT technology such as Fourier domain OCT, full field OCT, quantum OCT, etc. have been developed [8,9,11]. Among them Fourier domain OCT (FDOCT) has evolved as the most fruitful technique till now. Since the demonstration of better SNR capabilities of FDOCT in 2002-2003 by several groups [17 - 20], it has replaced TDOCT as basic approach of building OCT systems.

1.4.1 Time domain and Fourier domain OCT

In the interference term of equation 1.2, both k ($=2\pi/\lambda$) and path difference z appear inside the cosine term. Variation of either k or z leads to amplitude modulation of light from which depth information can be retrieved. In TDOCT configuration, the depth information is realized by measuring the interference signal as a function of optical delay Δz (or time). In TDOCT approach, while all the depths of the sample are illuminated, data is collected sequentially only from one depth at a time and the back-scattered light coming from other axial locations, outside the coherence gate, only contribute to the background or noise. In contrast, FDOCT approach uses a fixed reference arm and the interferometric signal is spectrally dispersed on a linear detector array. The Fourier transform of the measured interference spectrum in k-space is used to retrieve the axial (depth) information from all the depths simultaneously. Thereby, the Fourier domain approach not only improves signal to noise ratio but also eliminates the need for scanning in the reference arm and facilitates enhanced image acquisition speeds. Currently two methods exist to perform FDOCT imaging which requires measurement of interference signal in k-space (i.e. interference spectrum). This can be implemented by either using a broadband source and a

spectrometer (spectral domain approach) or by using a swept source (tunable laser) and a photodiode (swept source or optical frequency domain approach) [8, 14].

1.4.2 Functional OCT

The TDOCT and FDOCT approaches rely on the intrinsic variation of refractive index to avail the morphological information of the tissue constituents. Apart from imaging morphological features, OCT can also probe functional or pathological aspects that alter the amplitude, phase and polarization of the scattered light. This additional information may be intimately related to functional disturbances, which usually precede morphological changes and could be useful for early diagnosis of diseases. In this context, different versions of OCT systems such as polarization sensitive OCT, Doppler OCT, spectroscopic OCT, second harmonic generation (SHG) OCT, Coherent anti-Stokes Raman spectroscopy (CARS) OCT, elastography OCT, etc. have been developed to provide functional information like flow velocity, birefringence, molecular information of the tissue and stiffness of the tissue sample under study [8, 9]. However, among these OCT technologies, polarisation sensitive and Doppler OCT are the OCT technologies which moved furthest while the spectroscopic, SHG-OCT, CARS-OCT, and elastography OCT need further advancements for research as well as clinical acceptance.

1.4.2.1 Polarization-sensitive OCT

In contrast to conventional OCT, in which only the magnitude of the backscattered light is imaged, polarisation sensitive OCT (PSOCT) gives access to additional physical parameters like birefringence. Basically, it is the combination of OCT with polarimetry. The PSOCT measurement apparatus is similar to that of TDOCT or FDOCT, except that it allows measurements to be made for two orthogonal polarizations by incorporation of some polarizing elements like linear polarizer and quarter wave plates and a polarizing

beam-splitter (PBS). Hee *et al*. (1992) were the first to develop a polarisation sensitive low-coherence reflectometer and demonstrate depth resolved birefringence measurements in different samples like a wave plate, an electro-optic modulator and calf coronary artery [21]. This technique was later extended by de Boer *et al*. (1997) for two-dimensional mapping of the birefringence within a biological sample and used to demonstrate the birefringence changes in laser induced thermally damaged tissue [22]. Several biological tissues containing collagen and elastin fibers such as muscle, tendons exhibit birefringence. Propagation of light through these samples alters the polarization state of the light. In addition to the structural features of the tissue, polarization sensitive measurements can also be used for monitoring the ordering of birefringent constituents of the tissue [23]. It is being used for wide variety of applications in dentistry, ophthalmology dermatology, etc. [24, 25].

1.4.2.2 Doppler OCT

As we discussed in the previous section, the motion of reference mirror results in Doppler shift in the frequency of reference light which appears as beat signal when the interference between reference and sample field occurs at the detector. This Doppler frequency is linear with the relative motion of the reference and the sample and hence can be used to determine an object's velocity. This principle of Doppler shift of light scattered from moving particles is being exploited by laser Doppler velocimetry for the determination of flow velocities. Combining these approaches with OCT imaging leads to Doppler OCT (DOCT) which simultaneously gives access to structural data and velocity profiles of flowing, scattering media, and most importantly also of flowing media embedded in scattering structures [8, 26]. Doppler OCT imaging has been demonstrated on tissue phantoms, embryos, small animal skin-flap models, etc. and also on *in-vivo* blood flow in

the skin and in retina [27]. However, at present the maximum probing depth of the OCT system limits imaging to blood vessels close to the surface of organs.

1.4.2.3 Spectroscopic OCT

Spectroscopic optical coherence tomography (SOCT) is also a functional extension of OCT which performs depth-resolved spectroscopic measurements in addition to the morphology of the tissue, making it possible to differentiate tissue pathologies or functional state by their spectroscopic properties [11]. Spectral information can be obtained by measuring the full interference signal and using appropriate digital signal processing. Since there are two mechanisms for the modification of the light spectrum in tissue: scattering and absorption, therefore, depending on the contrast mechanism, the applications of SOCT imaging can be classified into two imaging modes: absorption-mode SOCT and scattering-mode SOCT. Endogenous (melanin, haemoglobin, etc.) or exogenous (contrast-enhancing dye) materials with characteristic absorption profiles can be used to provide spectroscopic contrast based on wavelength dependant absorption [28]. Similarly, wavelength-dependant scattering alters the spectral modulations present in spectroscopic OCT signal which can also be used for enhancement of contrast in OCT image [28].

1.5 OCT Applications

OCT and its variants are widely used in the field of biomedical imaging and diagnosis. One of the first applications was for imaging in ophthalmology [29, 30]. Ophthalmology is still the dominating field for OCT applications. Numerous basic as well as clinical studies, using both OCT and PSOCT, have been performed in the last decade which have established OCT as a valuable tool for the diagnosis and monitoring of retinal diseases

such as glaucoma, macular edema [29], macular hole [31], age related macular degeneration, etc. [32].

OCT is also being used in dermatology for imaging subcutaneous layers of the skin like of stratum corneum, epidermis and upper dermis [33]. OCT can identify the skin appendages (hair, sebaceous glands, sweat glands, nails) and blood vessels and helps in non-invasive monitoring of cutaneous inflammation and hyperkeratotic conditions [34]. Srinivas *et al*. [35] employed PSOCT to monitor burn depth in animal model and showed its potential to monitor thermal injury induced denaturization of the collagen in the skin which results in reduction of tissue birefringence. Yang *et al*. [36] used a Doppler OCT system for real-time monitoring of the micro-structural and micro-vascular tissue changes induced by laser thermal therapy.

The high scattering property of biological tissues limits the imaging depth to about a couple of mm only. However, in conjunction with the endoscopic and catheter-based procedures, the internal organs of the body such as gastro intestinal tract and intracoronary artery can be approached [13]. High resolution and high speed imaging are the important features of OCT that helps in detection of early neoplastic changes. The tissue architectural changes associated with early neoplasia can be observed by high resolution (a few micrometer) OCT. It can be used as a guiding tool for biopsy to reduce the false negative rates. Studies have also been performed to explore the use of OCT as a surgical guidance [37,38]. However, the development of OCT for cancer detection will require detailed studies to investigate its capability to visualize and identify clinically relevant pathologies. Advances in OCT technology have made it possible to use OCT in other specifications like dentistry, gynaecology, urology, etc. [39,40].

OCT has established itself as an imaging modality of choice for ophthalmic and dental applications. Numerous research applications of OCT technology in a broad range of fields as well as continuing development of the technology itself are continually emerging. OCT systems are also being engineered to be compact, low cost, and suitable for applications in research and in clinical environment.

CHAPTER 2: DEVELOPMENT OF TIME DOMAIN OCT AND PSOCT SETUPS

Abstract: In this chapter we first describe the time domain OCT setup developed by us. The results of our investigation on the use of tapered fiber tip for enhancing the lateral resolution of the OCT setup without significantly compromising the depth of imaging is discussed next. Finally, we describe the development of polarisation sensitive time domain setup to image the birefringent constituents (collagen, tendon, etc.) of the tissue in addition to the structural features of the tissue.

2.1 Choice of components

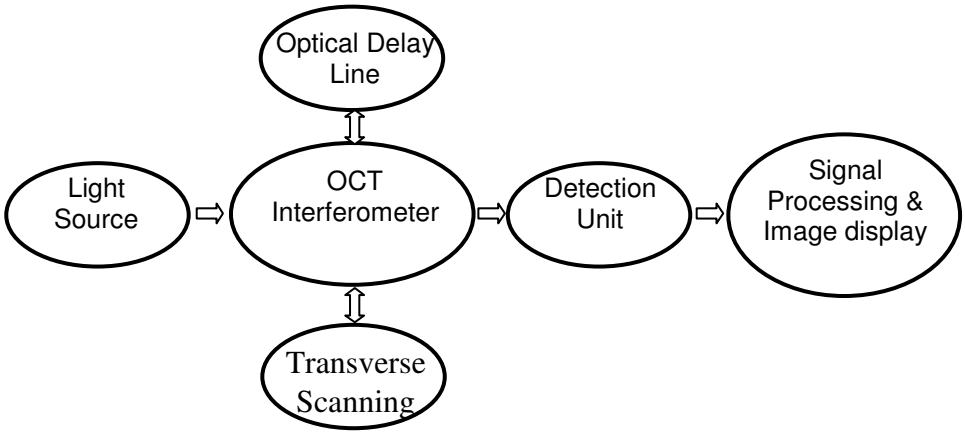

Figure 2.1: Different modules of an OCT imaging system

The important modules of an OCT system are shown in Figure 2.1. These include light source, interferometer, optical delay line for depth ranging, transverse scanning

mechanism for lateral imaging, detection unit for the measurement of interference fringes and hardware and software for data acquisition, signal processing and image display unit.

2.1.1 **Light source**

The performance of an OCT system is inherently depends on the light source used. The important criterion for the selection of the light source is that its wavelength should be in NIR region where tissue absorption is minimum. Further, it should have low temporal coherence, high power in single transverse mode and high spatial coherence. The first light sources used in low coherence interferometry were multimode laser diodes operating below threshold [41]. Later Huang *et al*. 1991 used superluminescent diode as a broadband light source for OCT imaging [10]. Till date, SLD is the most popular light source in OCT systems, as it provides broad bandwidth light with high spatial coherence. This is achieved by amplification of the spontaneous emission due to higher injection currents used [42]. The other sources are Kerr-lens mode-locked femto-second pulsed lasers (Ti-sapphire and Cr- forsterite) which provide broad spectrum and high power in infrared regime. These are the sources for OCT systems when ultrahigh resolution or high source power is required. Other notable source suitable for OCT applications with high output power are the photonic crystal fibers [8]. However, SLDs are still the dominating light sources in OCT due to its relative simplicity, compactness, robustness, and low cost. Therefore, we opted to use SLD as a light source for development of a portable OCT system in our laboratory.

2.1.2 OCT interferometer

The most commonly used interferometer configuration for OCT is the Michelson interferometer. It splits the input light into two parts, one of which is used as reference beam while the other as sample beam, and collects the back-reflected lights from both the arms for interference. The interferometer can be realized either in free space geometry

using optical elements or by the use of single mode fiber couplers [43]. In OCT applications, fiber based interferometers are most commonly employed since these offer distinct advantages in terms of system alignment, robustness, handling and portability. Further, fiber optic interferometer offer ease of integration with the endoscopic catheter for imaging internal tracts of the body. Other advantage of the single mode fiber implementation of the interferometer is its automatic assurance of the spatial overlap of the sample and reference light field on the detector. Use of single mode fibers also acts as spatial filters to remove any light that is scattered from the lowest order mode into higher order modes and thus preserve interference fringe contrast. Owing to these significant advantages of fiber optic interferometers, we used 50/50 fiber couplers (2×2) to realize Michelson interferometer for the development of OCT system.

2.1.3 Delay line

In a TDOCT system, optical path delay in reference arm needs to be varied for depth ranging. The scanning range should be large enough to cover the desired axial imaging range. The scanning speed should be high and uniform over the path length scan. It should have low hysteresis and dispersion effects [11]. A comparison of the various types of delay lines and their important features are tabulated below [11].

A DC motor based linear translation delay line offers large scanning range (~ 50 mm or more) with positioning accuracy of a fraction of the coherence length of the source. This is advantageous for imaging larger depth of samples like whole eye. For this reason we used a DC-motor based linear translating delay line for reference arm scanning.

Table 2.1: Various delay lines used in OCT systems and their important parameters.

Delay line scheme	**Repetition rate**	**Scan range**	**Duty cycle**	**Other remark**
Liner translation (retroreflector)	few Hz	Several cms	~100%	Larger depth scan Low repetition rate
Piezo-stretcher	~500 Hz	~few mm	~60 %	Fast but suffers hysteresis
Galvo-scanner based	10-30 Hz	~ few mm	>67%	Moderate
Rotating retro reflector	~50 -100 Hz	~ few mm	~ 2-20 %	Very high carrier frequency
RSOD	~1-4 kHz	~ few mm	~67%	Support high speed imaging

2.1.4 Transverse scanning

To get two dimensional cross-sectional images successive depth scans are performed at various lateral location of the sample. This can be realised either by scanning the beam on the sample surface or by scanning the sample itself. The important parameters for transverse scanner in OCT are the speed and the size of scanner. Since most of the OCT systems acquire depth priority B-scans, which use fast axial scanning and slow transverse scanning, size of the transverse beam scanner is a more critical parameter compared to its speed. The size of the scanner should be compatible with the free space available for the scanning mechanism. In our OCT setup, successive A-scans were recorded by moving sample using a motorized translation stage. Therefore the lateral range of the imaging is not limited by the field of view of objective lens used to focus the probe beam.

2.1.5 Detection unit, signal processing and image display

The OCT interference signal which consists of an envelope of width ~l_c superimposed on a carrier frequency is detected by a photodiode. The carrier frequency f_c can also be interpreted as the Doppler shift caused by the moving reference mirror, which creates a beat frequency at the photo-detector after mixing with un-shifted light returning from the layers of the sample. A trans-impedance amplifier was used to convert the interferometric photocurrent signal into a voltage signal and amplification of it. A band pass filter, centred at the carrier frequency f_c, separates the oscillating interferometric signal from the DC photocurrent and noise. The amplitude or envelope of the oscillating AC signal can be obtained either with a demodulator or by mixing the interferometric signal by a sinusoidal reference at the carrier frequency f_c followed by low-pass filtering. The measured envelope is subsequently digitized and stored on a computer for display of the OCT images.

In our OCT setup, we have employed a photodiode module which has a built in trans-impedance amplifier and a band pass filter. Envelope of this band pass filtered interference signal was measured using a lock-in amplifier. The lock-in amplifier first amplifies the input signal and then mixes the interference signal with a sinusoidal signal at carrier or Doppler frequency f_c generated by a built in local oscillator. The envelope of the interference signal is digitized with a data acquisition card for display of the images on computer screen.

2.2 System implementation

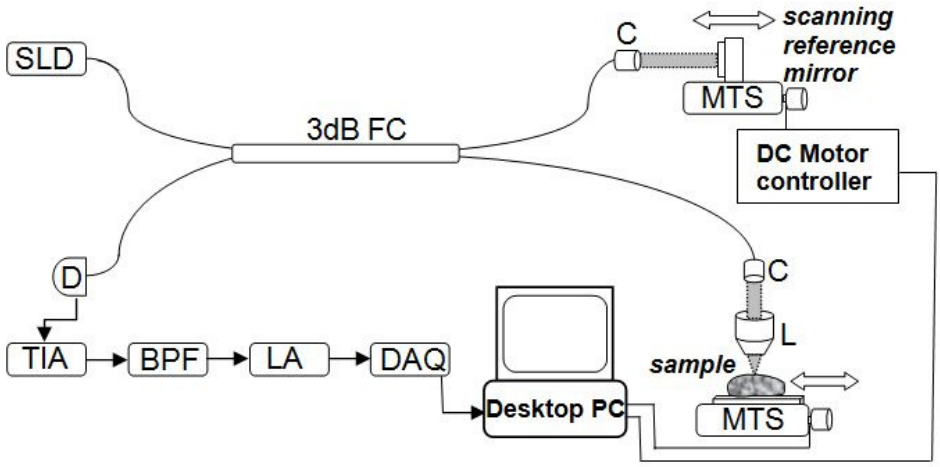

Figure 2.2: Schematic of OCT setup. BPF-bandpass filter; C-collimator lens; D-detector; DAQ-data acquisition card; FC-fiber coupler; LA-lockin Amplifier; MTS-motorized translation stage; SLD-superluminescent diode; TIA-transimpedence amplifier.

Figure 2.2 shows the schematic of the OCT setup developed by us. It employs a 5 mW SLD light source operating at 840 nm centre wavelength with ~ 40 nm bandwidth. The output of the SLD was coupled into a fiber based Michelson interferometer which makes use of a 50/50 fiber splitter (2 x 2) designed for the wavelength used. The Michelson interferometer equally splits the input beam into reference and sample arms. The light beam in the sample arm was collimated using a 4.5 mm focal length aspheric lens and focused onto the sample with a 10X microscopic objective lens. The same collimator and focussing objective assembly collect the backscattered light from sample and pass to the interferometer for detection. Similarly in the reference arm of the interferometer, a 4.5 mm focal length aspheric lens was used to collimate the beam and a reference mirror reflects the collimated beam back to the interferometer. The interferometer recombines the back reflected sample and reference beams and generates interference fringes at the photodiode.

The interference occurs only when the optical path between the reference and sample arms are matched within the coherence length of the source. To get depth information the optical path length in reference arm was varied by scanning reference mirror back and forth with a uniform velocity (~ 20 mm/s) using a DC motor based linear translation stage. The moving reference mirror results in 45 kHz Doppler shift to the reference light and produces beat frequency on interference. The detected amplitude modulated interference signal was amplified using a trans-impedance amplifier (TIA) and band pass filtered around 45 kHz. An envelope of the interference was obtained by demodulating the interference signal using a lock-in amplifier. The interferogram envelope was digitized and acquired in a PC using a data acquisition card (DAQ). For obtaining 2D images, transverse scanning was done by scanning the sample using a stepper motor. The motorized translational stage is controlled directly by the personal computer. Software based on LabView has been developed to set the desired imaging parameters and control the entire setup.

2.3 Labview Software

LabView 6.1, a graphical programming development tool from National Instruments (NI) was used for interfacing the OCT system with a computer, DC-motor controller (for depth scanning), stepper motor controller (for transverse scanning) and NI-DAQ card. Front panel of the program (shown in Figure 2.3) designed for user interface helps in setting all the desired imaging parameters. The LabView code synchronizes and controls the scanning motors in the reference and sample arms and generates the OCT intensity images from the acquired data sets. It initializes the scanning motors and takes care of all the parameters to be provided to the OCT system such as scan range, scan speed, number of pixels for the given image size, etc. It displays the acquired data in the intensity image

format and saves the measured data in the form of data file. The important information of the image such as axial and transverse scan range, number of steps and number of averaging (used if any) are logged in as a header to the data file. The image acquisition parameters retrieved from the header are used to determine the size and the aspect ratio of the image when analysing the saved data at a later time point. Figure 2.4 shows the flowchart that explains the flow of control in the Labview program or virtual instrument to acquire and display the OCT image. The OCT images, which are spatial distribution of amplitude of back-scattered light, were displayed either in gray scale or false-colour coded.

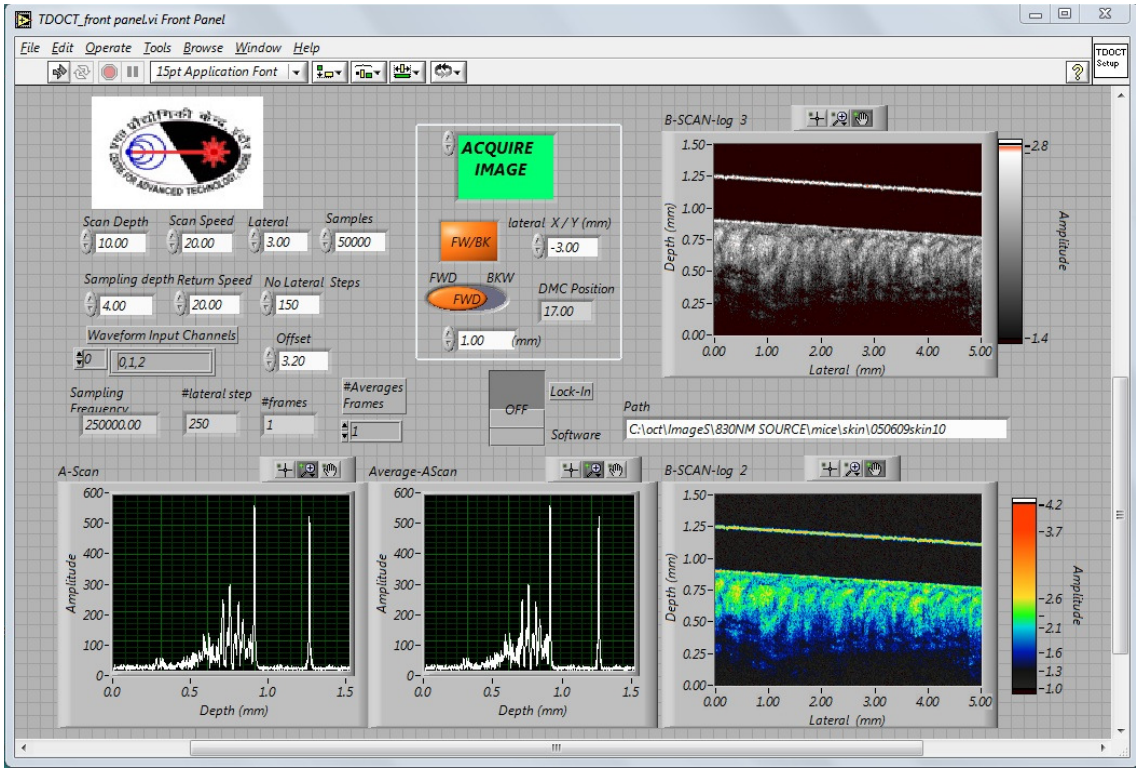

Figure 2.3: Front panel of the TDOCT setup used for setting up the desired imaging parameters and display of OCT images

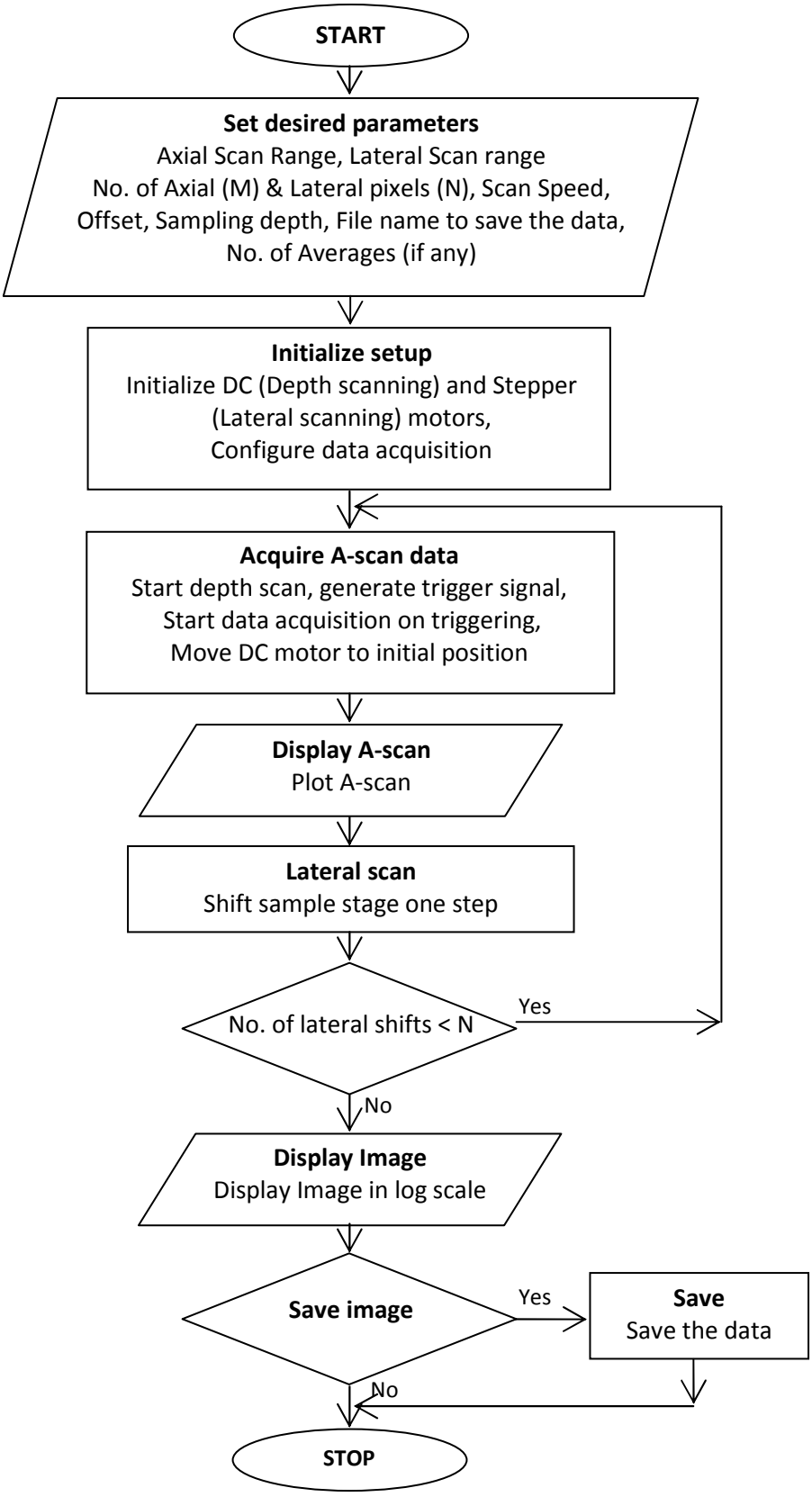

Figure 2.4: Flow of control in the Labview program (.vi) to acquire and display the OCT image.

2.4 System characterization

In Figure 2.5 a, we show a typical interferogram signal (red waveform) obtained using a mirror in the sample arm of the interferometer. The corresponding demodulated envelope is also shown in the Figure 2.5 a (white waveform). The height of the envelope represents the amplitude of the back-scattered light while the width of envelope (enlarged portion is shown in Figure 2.5 b) can be used to get the axial resolution of the setup. From this we estimate an axial resolution of ~ 11 µm for our setup. The lateral resolution (Δx) of the setup is determined by focal spot size on the sample, i.e., $\Delta x = (4f\,\lambda/\pi d)$, where f is the focal length of the imaging lens and d is the diameter of the beam on the lens. The estimated value of lateral resolution for 10× microscopic objective was ~17 µm.

The SNR of the OCT system was measured by using a mirror in the sample arm. To avoid saturation of the detector the sample light was attenuated with a neutral density filter. The detector gain was adjusted until the output signal was just below the saturation limit of the detector. The SNR can be measured as the ratio between the amplitude of the interference signal and the standard deviation (σ) of the noise as given below:

$$SNR = 20\log\left(\frac{Signal}{\sigma}\right) + 2\times NDfilter(dB) \qquad (2.1)$$

The measured SNR for the OCT system was ~100 dB.

Figure 2.5 c shows the interferogram of a microscopic cover slip with two peaks (interferogram envelops) corresponding to the air–glass and glass–air interfaces. From the measured peak separation of 227 µm (optical path length) and assuming glass refractive index ~ 1.5, the thickness of coverslip was estimated to be ~ 152 µm, which was in good agreement with the value measured using a calliper.

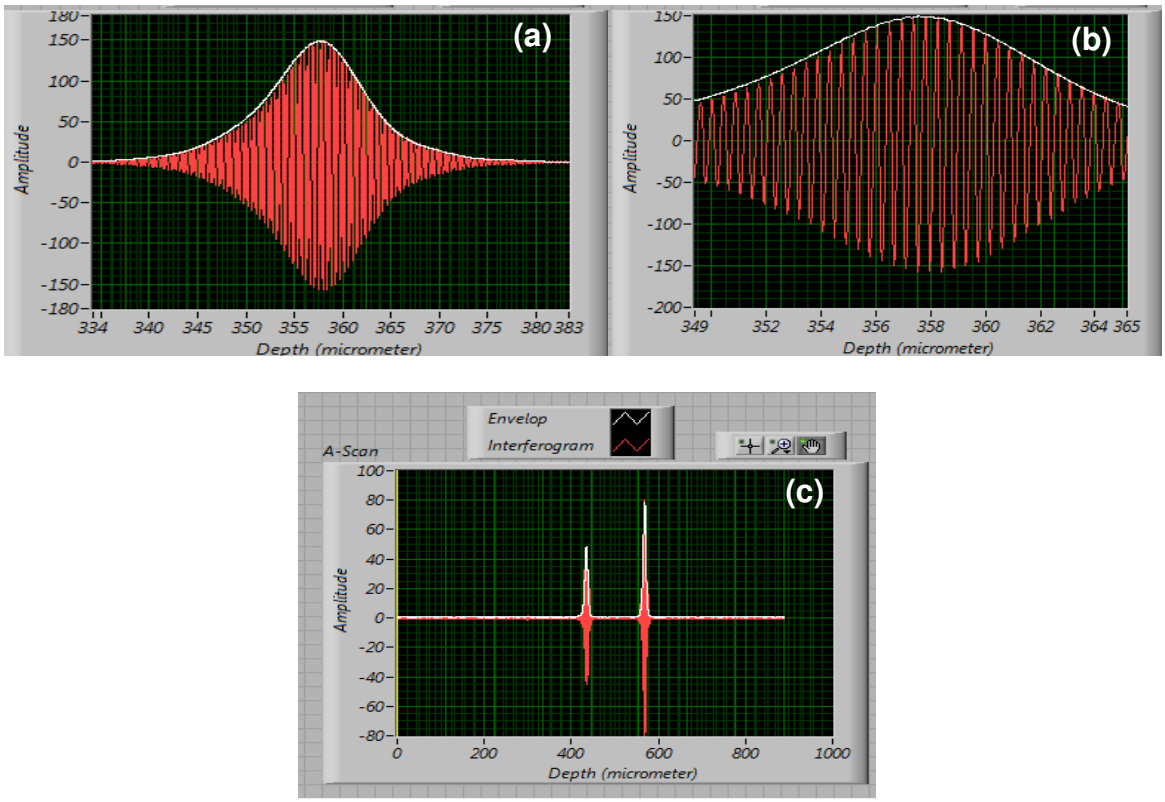

Figure 2.5: (a) Typical interferogram acquired using the set-up and its demodulated envelope. (b) Zoomed view of interferogram and its envelope (c) OCT signal or A-scan of a microscopic cover slip showing two peaks for front and back interface of the coverslip.

Figure 2.6 shows some representative images acquired with the OCT setup. Figure 2.6 (a) shows the 2D cross-sectional OCT image of human finger pad. The reddish color visible at the surface of tissue show the highest back scattered intensity owing to the large refractive index mismatch at air-tissue (1 and 1.34) interface. Inside the tissue, the layered structure of the skin is visible. The two distinct layers are known as epidermis and dermis of the skin. The measured thickness of the epidermis was found to be ~ 250 µm. The imaging depth obtained for the skin images was about ~ 600 µm. Figure 2.6 (b) shows the OCT image of the human nail. Different anatomical features of the nail fold such as nail plate, nail bed, epidermis and cuticle are differentiated in OCT image. Figure 2.6 (c) shows an

OCT image of a formalin fixed intact Zebrafish eye. Various ocular structures of the eye such as cornea, iris, lens and retina of the eye are clearly visible in the imaged.

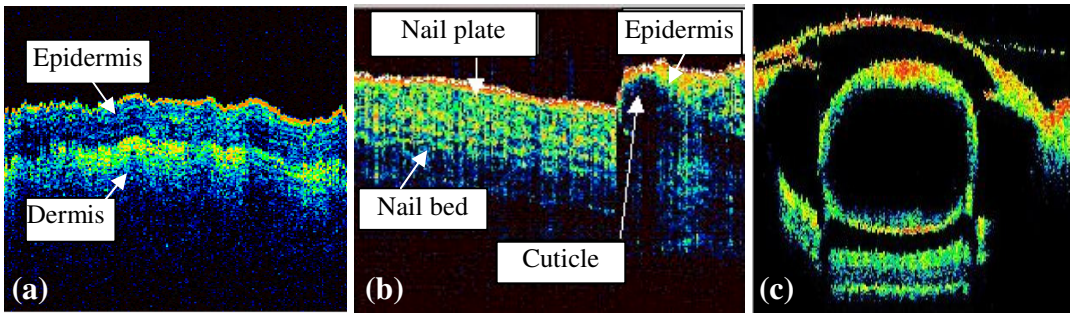

Figure 2.6: OCT images of (a) human skin, (b) nail and (c) Zebrafish eye acquired with the developed OCT setup. Image size: a & b: 2 mm x 3 mm; c: 3 mm x 2 mm.

2.5 Improvement in Lateral resolution

As discussed previously, the axial resolution of OCT is determined by the source coherence length and the lateral resolution by the spot size at the sample surface. Conventional OCT systems typically achieve lateral resolutions in the range of 20-30 µm using low numerical aperture imaging objectives. Use of the shorter focal length objective lens would improve lateral resolution but at the cost of imaging depth. To address this problem we investigated the use of tapered fiber tips for enhancing lateral resolution of OCT setup without significantly compromising the depth of imaging.

A single mode optical fiber (Thorlabs, USA) appropriate for 840 nm was used for preparing the tapered tips. One end of the fiber was connectorized with FC connector for joining it with the sample arm of the 2x2 optical fiber coupler. The other end of the mechanically cleaved bare single mode fiber was dipped into 40% Hydrofluoric (HF) acid containing a protective layer of Toluene at the top (Figure 2.7 (a)). The tip formation takes place at the interface of the etching liquid and the protecting over layer. As described by

Hoffmann et al. [44] the cone angle of the fiber tip is determined by the contact angle of HF with the fiber. The etching process is self-terminating and the cone angle is influenced by the liquid used as protection layer. In order to have large cone angle we used Toluene as the protection layer. Fig. 2.7 (b) shows a microscopic image of the prepared tip, recorded using an inverted microscope (Zeiss, Axiovert 135 TV) with a Leica camera (Model: DC 350F). From the acquired image, the cone angle of the tip was measured to be ~ 27^0.

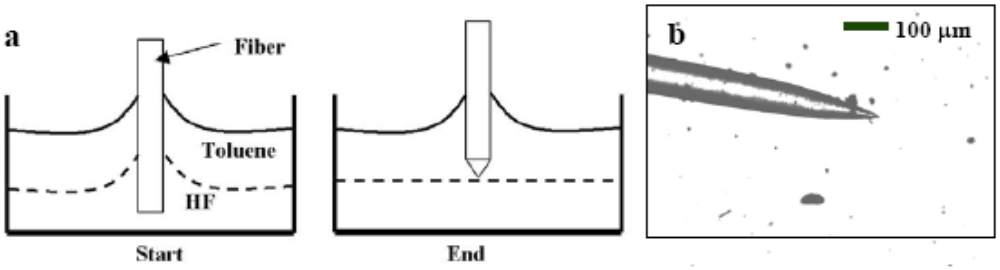

Figure 2.7: (a) Schematic of the chemical etching process, (b) Microscopic image of the tapered tip

Figure 2.8 shows the sample arm of the interferometer modified to incorporate the tapered fiber tip. In the modified interferometer, the collimation and focusing optics in the sample arm was replaced with a fiber having fibertip. To minimize the dispersion effects, the optical path in reference arm was compensated as far as possible by adding appropriate fiber length and thus minimize air path. The measured free space axial resolution for the modified interferometer was ~16 µm.

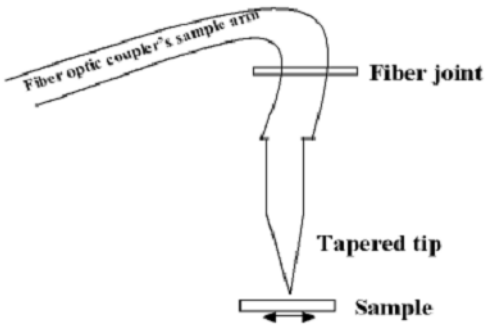

Figure 2.8: Modified sample arm with the tapered tip.

The tapered region of the fiber can be modelled as equivalent to a lensed fiber. Starting with the fundamental mode of the single mode fiber with core size ~9 μm, $E_{fund} \approx \exp\left(\frac{-(X^2+Y^2)}{\omega^2}\right)$ where ω is the mode field size, the electric field propagating from the tip at any observation point (x_o, y_o) can be described as [45]:

$$E(x_o, y_o) = \frac{\exp(ikz)}{i\lambda z} \exp[i\frac{k}{2z}(x_o^2 + y_o^2)] \int_{-\infty}^{\infty}\int_{-\infty}^{\infty} \{E(x_1, y_1) \exp[i\frac{k}{2z}(x_1^2 + y_1^2)]\} \exp[-i\frac{2\pi}{\lambda z}(x_o x_1 + y_o y_1)] dx_1 dy_1 \quad (2.2)$$

where E (x_1,y_1) is the field at the point (x_1,y_1) on the conical aperture. E (x_1,y_1) can be calculated using the fundamental mode field E_{fund} and accounting for the phase acquired along the taper region. Figure 2.9 (a-c) show the beam profiles of the SLD beam transmitted through the tapered fiber measured at distances of 50 μm, 100 μm and 200 μm from the tapered tip respectively. Figure 2.9 (d-f) show the corresponding calculated transmitted intensity profiles. We have used a core size of 9 μm, cone angle of ~ 27^0 and air as the surrounding medium for these calculations. The slight asymmetry noticed in the

measured profiles may be attributed to the quality of the tip, since the chemically etched tips are sensitive to environmental influences such as vibrations, temperature drifts, etc., during the etching process. This can further be improved by modified etching procedures such as etching the fiber through the acrylate jacket [46], tube etching [47], reverse- tube etching [48] and dynamic etching [49]. The simulated beam profiles are in reasonable agreement with experimentally measured profiles. Two factors are responsible for the observed deviation between the experimentally measured and theoretically estimated beam profiles. First, leakage from the tapered region of the fiber which was not accounted for in the simulation, second, the shape of the fiber tip fabricated using chemical etching process may deviate from perfect conical shape as has been assumed in the theoretical simulations.

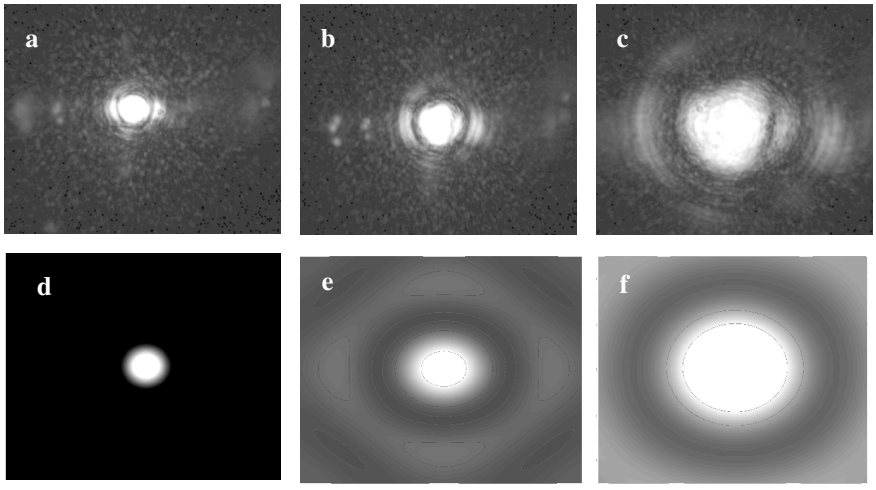

Figure 2.9: Beam profiles of the laser beam transmitted through the tapered fiber measured at distances distance of (a) 50 µm , (b) 100 µm and (c) 200 µm from the tip; Calculated spatial mode profile at (d) 50 µm, (e) 100 µm and (f) 200 µm. Images (a-f) are in same magnification. Image size: 25 µm x 25 µm.

The transverse intensity distribution of the calculated beam profiles, are shown in Fig. 2.10 (a) for the distances of 50 µm, 100 µm and 200 µm. The beam waist is found to be increasing with increase in axial distance from the tip. However, the rate of increase in the

beam waist is slower compared to the beam spread when a microscopic objective 20X is used as shown in Figure 2.10 (b).

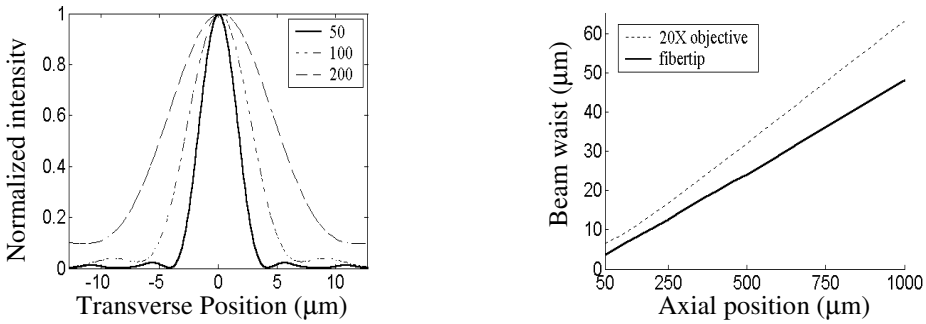

Figure 2.10: (a) Beam profiles of the laser beam transmitted through the tapered fiber measured at distances distance of 50 μm, 100 μm and 200 μm. (b) Beam waist as a function of axial distance from tip.

Figure 2.11 shows the results of the use of the modified OCT set-up to image different objects. Figure 2.11a shows OCT image of the scattering medium when the imaging tip is dipped in the intralipid placed on a cover slip. The reflection from the cover slip is also seen in the image. Figure 2.11b shows the OCT image of the scattering from an infrared viewing card. In order to verify that the OCT set-up incorporating the tapered fiber is able to image through biological tissues, we used the set up to image *Elodea densa* plant leaf. The choice was made because the cells are large (~ 100 μm x 40 μm x 30 μm) and have a large number of chloroplasts having typical size of 6 μm [50] which is lower than the lateral resolution available with our conventional OCT set up and larger than the tapered tip size.

Figure 2.11 c shows the OCT image of a plant leaf (*Elodea densa*) taken with a tapered tip and Figure 2.11 d shows the processed image after applying minimum filter using National Institute of Health (NIH)'s public domain software ImageJ. The

rectangular boxes in Figure 2.11 c outline the cell boundaries. Figure 2.11 e shows the *Elodea densa* section taken using a conventional OCT set up with 10X microscopic objective (lateral resolution ~17 μm) with a selected region (size comparable with Figure 2.11 d), marked inside box, shown separately in Figure 2.11 f. The image taken using the tapered tip shows intracellular structures (black spots being the chloroplasts), which could not be visualized by the conventional setup. The resolution therefore is enhanced using the fiber tip probe, without the need of high NA microscopic objectives.

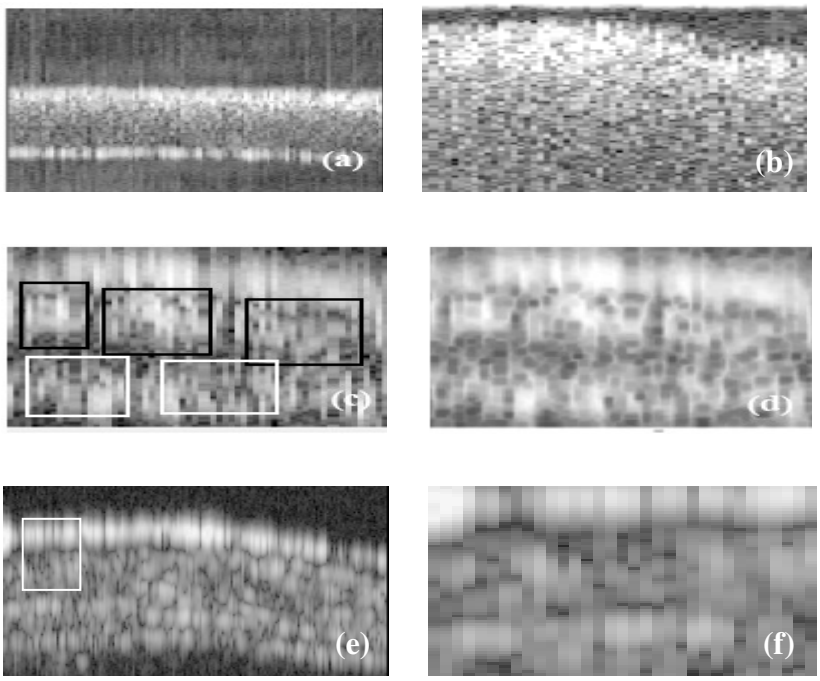

Figure 2.11: OCT images with the modified set-up with the tapered fiber tip (a-d): (a) Scattering from intralipid placed on coverslip. (b) OCT image of scattering from infrared viewing card; Image size (a & b):0.4 mm (depth) x 0.2 mm (lateral). (c) OCT image of plant leaf *Elodea densa* and (d) after applying minimum filter using ImageJ software. Image size (c & d): 0.1 mm (depth) x 0.2 mm (lateral). (e) OCT image of *Elodea densa* taken with conventional OCT set-up with 10 X microscopic objective. Image size: 0.2 mm (depth) x 1.0 mm (lateral). (f) Expanded image of the marked region; size 0.1 mm (depth) x 0.2 mm (lateral).

The sensitivity of the fiber-tip incorporated OCT set-up, as characterized by the SNR of the interferogram, can be increased by using tips with larger cone angle and

further application of metal coating outside the tapered region to reduce the losses [44]. Further, the tapered fiber tip OCT setup is most suitable for M-mode imaging of dynamic processes spatially localized in very small regions of biological tissues.

2.6 Development of Polarization sensitive OCT setup

The basic OCT system relies on the spatial variation of refractive index that modifies the amplitude of the light and provides contrast to the OCT images. Many biological structures have properties such as birefringence, optical rotation and diattenuation which can modify the polarisation state of the incident light. Incorporation of polarization sensitive measurements with OCT makes it capable of visualizing the polarization contrast stemming from optical polarization properties of samples. We have developed a PSOCT setup which measures the depth-dependent changes in the polarization state of detected light to determine the polarization parameters of a sample. In this setup, the sample is illuminated by a circular polarized beam and the birefringence of the sample can be obtained by measuring the envelope of the interferometric signal in linear orthogonal components [21]. A circularly polarized incident state is preferred in order to keep the measurements independent of the orientation axis of the sample. In fiber based setups, it is difficult to propagate (or deliver) a circular polarization state at the sample surface, as environmental stress change the polarization state of the light travelling through the fiber. Therefore, a free-space optical system was developed for the measurement of tissue birefringence.

2.6.1 System description

Figure 2.12 shows the schematic of a single detector based free space PSOCT setup. A SLD having centre wavelength 840 nm and bandwidth ~ 40 nm was used as a light source.

The output of the SLD was collimated and passed through a linear polarizer (P) to get vertically (V) polarized light beam and then split into reference and sample arms using a non-polarizing beam splitter (NPBS). In the reference arm, another non-polarizing beam splitter (NPBS2) splits the incident linearly polarized light into two beams. One of the reference beam, reflected from the NPBS2, passes through a QWP2 with its fast axis oriented at 45° and reflected back by a mirror (M2) to provide horizontally (H) polarized reference light in round trip. Another reference beam, transmitted through the NPBS2, gets reflected from mirror (M1) to provide V polarized reference beam. Both mirrors were mounted on the same translation stage such that the optical path lengths in reference arm for H and V polarized light differ by ~ 2 mm, greater than the imaging depth for the source wavelength. In the sample arm the linearly polarized light passes through a QWP with its fast axis oriented at 45° to the incident vertical polarization to produce circularly polarized light. A 10X microscopic objective lens then focuses the circularly polarized light onto the sample surface. The light scattered from the sample, in general has an arbitrary (elliptical) polarization state determined by the optical properties of the sample, and returns through the focusing optics and the QWP. This light recombines with the H and V polarized reference beams in the detection arm, and produces temporally and spatially shifted horizontal and vertical components of interference signals I_H and I_V respectively. This arrangement offers the advantage that a single detector can be used to detect interference signals in the two orthogonal channels. This helps to ensure that the sensitivity and noise in both the polarization channels remains the same [51]. The detected interference signals are amplified and band pass filtered. A lock-in amplifier (EG & G 7265) was used for demodulation of the interferogram. The demodulated signal was digitized with a data acquisition card (NI PCI 6110). All subsequent data processing and display of images were performed in the software. The logarithm of the amplitudes of the acquired data are

displayed and stored on a personal computer. The estimated axial and lateral resolutions were ~ 11 µm and ~ 17 µm respectively. The image acquisition time was ~ 100 sec for an image consisting of 1000 (depth) x 100 (lateral) pixels. The measured SNR of the setup was ~ 93 dB.

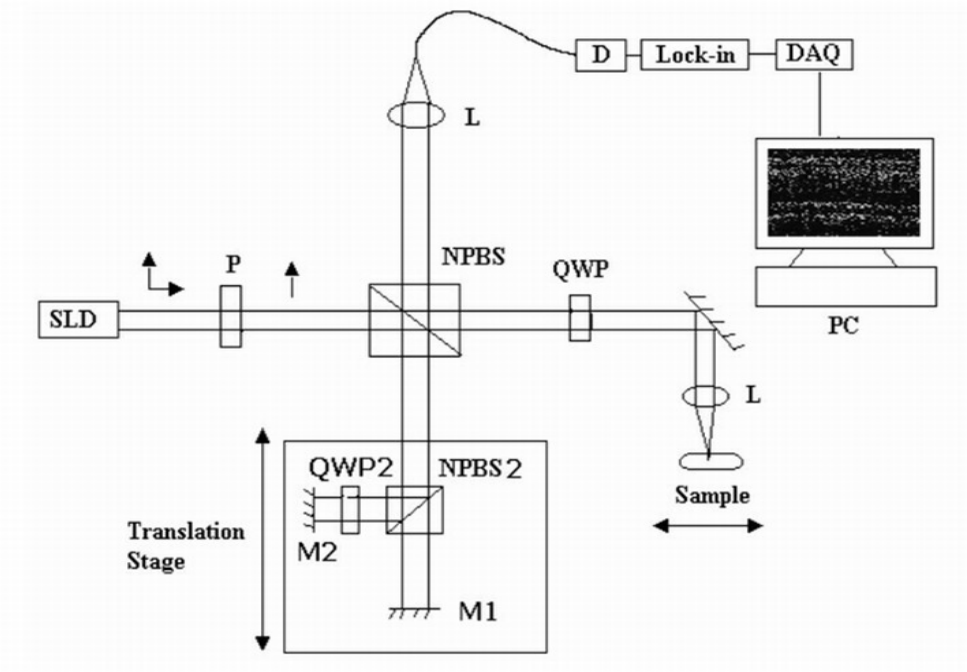

Figure 2.12: Schematic of single detector based polarization sensitive optical coherence tomography setup. D- Detector; L- lens; M1,M2: Mirrors; NPBS- Nonpolarizing beam splitter; P- Polarizer; QWP- Quarter wave plate; SLD- Superluminescent Diode.

2.6.2 Calculation of the polarization states:

The Jones matrix formulation can be employed for describing the polarization state of the light passing through the different optical components of the interferometer [52]. The polarization state of the light after passing through a horizontal linear polarizer can be defined by a Jones vector

$$\mathbf{E} = E_0 \begin{pmatrix} 1 \\ 0 \end{pmatrix} \tag{2.3}$$

where $E_0 = A_0(k)\exp[i(\omega t)]$ is the scalar electric field and $A_0(k)$ is the field amplitude as a function of wave number $k=2\pi/\lambda$. A non-polarizing beam splitter splits the linearly polarized input light into the reference and the sample arms. In the sample arm of the interferometer, the horizontally polarized light is passed through a *QWP* with fast axis oriented at 45^o with respect to the horizontal axis. The Jones matrix of *QWP* (fast axis at 45^o) can be expressed as

$$J_W = \frac{1}{\sqrt{2}} \begin{bmatrix} 1 & i \\ i & 1 \end{bmatrix} \tag{2.4}$$

After passing through the *QWP,* the electric field vector is

$$\frac{1}{\sqrt{2}} \begin{bmatrix} 1 & i \\ i & 1 \end{bmatrix} . \frac{E_0}{\sqrt{2}} \begin{pmatrix} 1 \\ 0 \end{pmatrix} = \frac{E_0}{2} \begin{pmatrix} 1 \\ i \end{pmatrix} \tag{2.5}$$

which denotes a circularly polarized light. If the sample is assumed as a linear birefringent material having birefringence Δn with fast axis oriented at an angle Φ with respect to the horizontal, it can be expressed as [51]:

$$J_S = \begin{bmatrix} \exp(i\delta/2)\cos^2(\Phi) + \exp(-i\delta/2)\sin^2(\Phi) & 2i\sin(\Phi)\cos(\Phi)\sin(\delta/2) \\ 2i\sin(\Phi)\cos(\Phi)\sin(\delta/2) & \exp(-i\delta/2)\cos^2(\Phi) + \exp(i\delta/2)\sin^2(\Phi) \end{bmatrix} \tag{2.6}$$

where δ (= $2\pi . \Delta n / \lambda_0$) is the phase retardance experienced in travelling a distance d in the tissue. Assuming the sample reflectivity $R_S(d)$, the back scattered electric field that returns to the beam splitter after traversing a distance d in the sample can be expressed as:

$$E_S(d) = J_W J_S \sqrt{R_S(d)} J_S J_W E_0 \tag{2.7}$$

$$E_S(d) = \frac{1}{\sqrt{2}} \begin{pmatrix} \sin(\delta)\exp(2i\Phi) \\ \cos(\delta) \end{pmatrix} \sqrt{R_S(d)} E_0 \exp(-i2kl_s) \tag{2.8}$$

where $l_S = l_0 + d$ is the optical path length travelling from the beam splitter to the sample surface (l_0) and in the sample d, $R_S(d)$ is the sample reflectivity at a given depth d. In the reference arm of the interferometer, the linear polarized light splits in two parts E_{R1} and E_{R2} by a beam splitter (NPBS2). One of them passes through a QWP2 oriented at 45° with respect to the horizontal axis and returns through the same wave plate after getting reflected from the reference arm mirror M2 (see Figure 2.12). After passing through the beam splitter, the sample and the reference arm beams (E_{R1} and E_{R2}) in the detection arm can be expressed as:

$$E_S = \frac{1}{2}\begin{pmatrix}\sin(\delta)\exp(2i\Phi)\\ \cos(\delta)\end{pmatrix}\sqrt{R_S(d)}E_0\exp(-i2kl_s) \tag{2.9}$$

$$E_{R1} \cong \frac{E_0}{2}\begin{pmatrix}1\\0\end{pmatrix}\exp(-i2kl_{r1}) \quad \text{and} \quad E_{R2} \cong \frac{E_0}{2}\begin{pmatrix}0\\1\end{pmatrix}\exp(-i2kl_{r2}) \tag{2.10}$$

where E_{R1} and E_{R2} are H and V polarization electric field in reference arm and l_{r1} and l_{r2} (= $l_{r1} + \Delta l$) are the optical path for the different beams in reference arm with offset Δl. The sample and reference arm electric fields (equation 2.9 and 2.10) recombine and generate interference fringes, which can be written as:

$$\langle E_{SR}\rangle^2{}_H = \langle E_S + E_R\rangle^2{}_H = \left\langle \frac{E_0}{2}\left(\sqrt{R_S(d)}(\sin(\delta)\exp(2i\Phi))\exp(-i2kl_S) + \exp(-i2kl_{r1})\right)\right\rangle^2 \tag{2.11}$$

$$\langle E_{SR}\rangle^2{}_V = \langle E_S + E_R\rangle^2{}_V = \left\langle \frac{E_0}{2}\left(\sqrt{R_S(d)}(\cos(\delta))\exp(-i2kl_S) + \exp(-i2kl_{r2})\right)\right\rangle^2 \tag{2.12}$$

The orthogonal polarization components of interference signals at the detector are:

$$I_H \approx \frac{E_0^2}{4}\left(1 + R_S(d)\sin^2(\delta) + \sqrt{R_S(d)}\sin(\delta)\cos 2(\Phi + k\Delta l_{r1})\right) \tag{2.13}$$

$$I_V \approx \frac{E_0^2}{4}\left(1 + R_S(d)\cos^2(\delta) + \sqrt{R_S(d)}\cos(\delta)\cos 2(k\Delta l_{r2})\right) \tag{2.14}$$

After lock-in demodulation, the obtained orthogonal polarization interference signals are

$$I_H \approx \sqrt{R_S(d)}\sin\delta \quad \text{and} \quad I_V \approx \sqrt{R_S(d)}\cos\delta \tag{2.15}$$

Conventional OCT images (or the reflectivity map) and accumulated phase retardation (δ) images of the sample can be obtained as per the following relations:

$$R_s(d) = I_H^2 + I_V^2 \tag{2.16}$$

$$\delta(z) = \arctan[I_H(z)/I_V(z)] \tag{2.17}$$

It can be observed from the above relations that only intensity measurement (amplitude measurement) is sufficient to determine the phase retardation between the orthogonal polarization components of light. The fast axis orientation (Φ) can also be determined by measuring the phase difference of the interferometric signals (eq. 2.9 and 2.10) that requires phase sensitive OCT measurements [53].

2.6.3 Characterisation of PSOCT setup

For calibration of the PSOCT setup, phase retardations of quarter wave plates designed for three different wavelengths (532 nm, 665 nm and 1054 nm) were measured. The comparison of the phase retardation value measured by PSOCT setup and with the conventional polarimetry method [52] using a combination of polarizer, analyzer and sample wave plate is shown in the Table 2.2.

Table 2.2: Comparison of phase retardation measured with polarimetry and PSOCT.

Quarter wave plate Design wavelength(nm)	Measured Phase retardation using polarimetric method(degrees)	Measured Phase retardation using PSOCT(degrees)
532	57	55.5
665	67.5	68
1054	73	69.7

The phase retardations for these wave plates at 840 nm were measured using the experimental configuration shown in Figure 2.13. The light output from SLD source was passed through a polarizer and an analyzer. The orientation of the analyzer was set to get null intensity. The wave plate (WP) of unknown retardation (for 840 nm wavelength) was inserted in between the polarizer and analyzer. The inserted WP was rotated to get the minimum intensity. After that the WP was rotated by 45° from its optic axis. The co-polarized (I_o) and cross-polarized (I_{90}) components of the intensity of the light passing through polarizer, wave plate and analyser were measured using a photodiode. The retardation of the wave plates were measured using the following formula [52]:

$$\delta = \cos^{-1}\left(\frac{(I_0 - I_{90})}{(I_0 + I_{90})}\right) \tag{2.18}$$

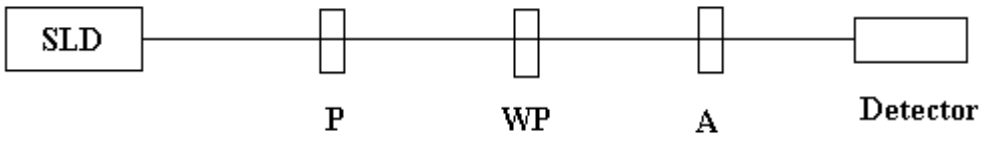

Figure 2.13: Experimental Set up for measuring Phase retardation of wave plate (WP). SLD: Superluminescent diode; P: Polarizer; A: Analyzer.

The small deviation between the PSOCT and polarimetric measurements can be attributed to the errors in setting of wave plate axis at desired orientation and also due to the slight offset of design wavelength of polarizing optics from the source wavelength. As mentioned earlier circularly polarized light was used in the sample arm of the interferometer to keep the phase retardation measurements independent of the optic axis orientation of the sample. To verify that the phase retardation is independent of the

orientation axis, the phase retardation value of a wave plate was measured for its different fast axis orientations (Figure 2.14). The measured mean value of the phase retardation is 68.3° with standard deviation of 1.7° .

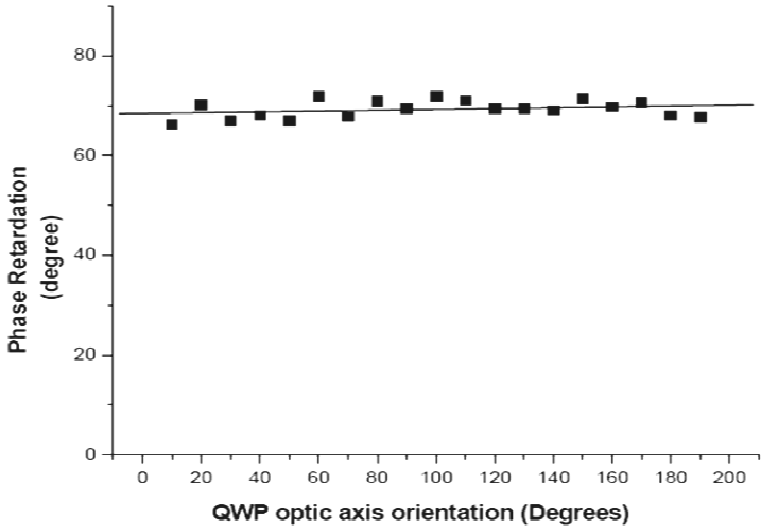

Figure 2.14: Measurement of phase retardation of wave plate (design wavelength 665 nm) for various orientations of fast axis.

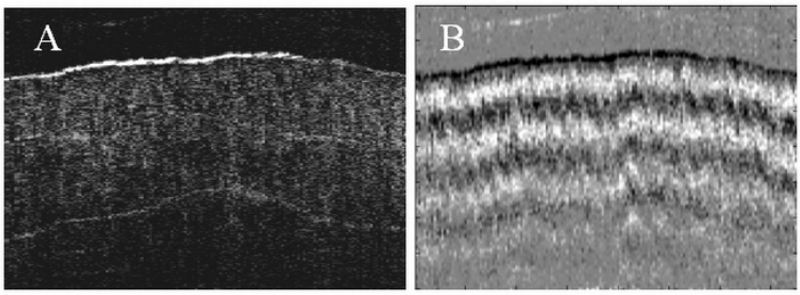

Figure 2.15: Intensity (a) and cumulative round-trip phase retardation (b) images of chicken breast tissue in-vitro. Image size: 1.2 mm (depth) × 3 mm (lateral).

Figure 2.15 (a) & (b) show the intensity and cumulative round trip phase retardation image of chicken breast tissue in-vitro. The phase retardation map of the sample is gray-scale coded from 0 to 90 degrees. While the intensity image shows the scattering information of the tissue, the birefringence of the tissue sample is depicted in the phase retardation image. Because of the cumulative nature, it shows periodic changes in the phase retardation [54]. The birefringence can be determined by measuring the average distance between the two consecutive white bands (corresponding to π phase retardation). The measured average distance 200 ± 22 µm corresponds to the birefringence value $2 \pm 0.3\times10^{-3}$. The observed average distance of ~ 200 µm for π phase retardation is in agreement with the reported literature [55].

2.7 Summary

A time domain linear translation stage based fiber coupled OCT setup has been developed which can provide two dimensional cross-sectional images with ~11 µm and ~17 µm axial and lateral resolutions respectively. The setup is capable of acquiring images at a rate of one image per minute limited by the scanning speed of the linear translation stage. However, it has the advantage that a larger depth scan can be performed which would be suitable for imaging less scattering samples. An effort was also made to improve the lateral resolution by incorporating the chemically etched fiber tip in the sample arm of the interferometer. Using the modified setup, imaging of the intracellular structure like chloroplast of the elodea densa plant cell (corresponding to lateral resolution ~3 µm) was demonstrated. For utilization of polarisation contrast, a PSOCT setup was developed in free space geometry. The PSOCT provides two dimensional map of phase retardation (or birefringence) in addition to the structural features of the tissue.

CHAPTER 3: DEVELOPMENT OF HIGH SPEED OCT SETUPS

Abstract: For clinical applications of OCT and for reducing motion-artefact during imaging of living objects, high-speed image acquisition is essential. In this chapter we first describe the development of a high speed OCT setup by incorporation of a rapid scanning Fourier domain optical delay line (FDODL) in TDOCT system (discussed in chapter 2) to achieve image acquisition at 8 frames per second (with 500 A-cans per image). Development of a more sophisticated Fourier domain OCT imaging setup with image acquisition speed of 10 frames per second (with 1000 A-cans per image) and a better signal to noise ratio is discussed next.

3.1 Time Domain High Speed Imaging Setup

3.1.1 Implementation of rapid scanning FDODL

In time domain OCT, a high speed scanning delay line is required in the reference arm of the interferometer in order to produce real time imaging. Use of a retro-reflector translated by a linear translation stage or a galvanometer-based translation system can provide axial scan rate of a few axial scans/s to ~ 100 axial scans/s [56]. Piezo-electric fiber stretcher based delay line has been used to achieve scan rates of ~ 600 scans/s. However, for near

real time imaging, say 10 frames per second with 500 A-scans per frame, about 5000 A-scans/sec are required [57]. Further, the translation of the retroreflector at high speed also leads to a higher modulation or carrier frequency (~ 100 MHz) which degrades detection sensitivity [11]. Therefore, methods based on dispersive delay lines have been used which not only provide a control over the modulation frequency but also help in controlling the dispersion mismatch between the reference and sample arm of the OCT interferometer [58]. This scheme makes use of the well known fact that an addition of a linear phase ramp in the frequency domain results in a group delay in the time domain. This is described by the following equation [58]

$$f(t-t_0) = F(\omega)e^{-j\omega t_0} \tag{3.1}$$

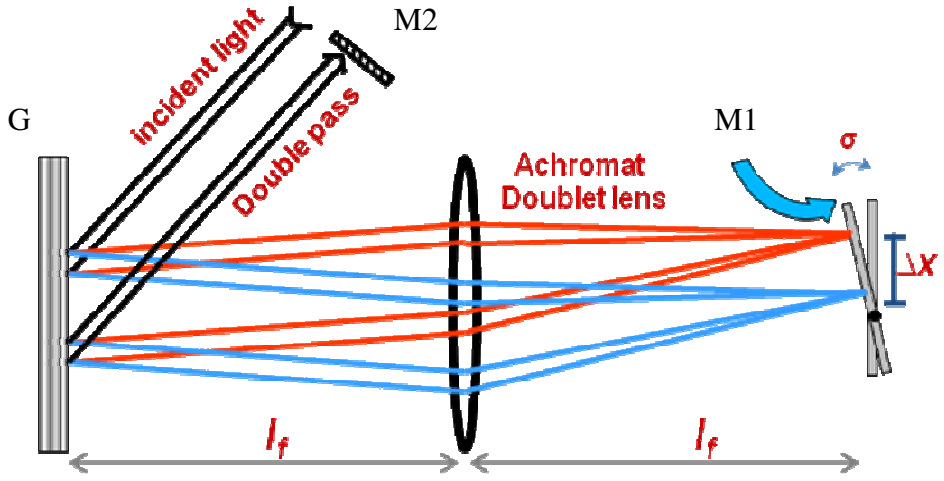

Figure 3.1: Ray diagram of the rapid scanning FDODL. G-grating; M1-resonant scanning mirror; M2-Double pass mirror [58].

A schematic of the FDODL is shown in Figure 3.1. A collimated broadband light is incident on the diffraction grating at an angle θ such that the diffracted light propagates

normal to the grating. The grating G is placed at the back focal plane of an achromat doublet lens. The dispersed light is focussed on a mirror (resonant scanner mirror) which is placed at the front focal plane of the lens. Since the light is spectrally dispersed by the grating, different wavelength components of the light focus at spatially shifted location of the mirror resulting in a line on the scanning mirror (M1). The scanning mirror imposes a linear phase ramp on the spectrum and reflects the light back through the lens, which re-collimates the spectrum onto the grating. The grating then diffracts the beam (in a reverse manner) and passes to the double-pass mirror. The reflected light from the double-pass mirror (M2) follows its original path in reverse direction. From the grating equation, it follows that the grating diffracts the spectral component $\Delta\lambda$ (i.e. λ-λ_0) into the angle $\Delta\theta=\Delta\lambda/p.cos\theta$ where p is the grating period and $\Delta\theta$ is the difference between the diffraction angle of the wavelength components λ and λ_0. The phase shift $\phi(\lambda)$ as a function of wavelength (λ) for a given mirror tilt angle (σ) and a lateral shift (x) of the beam with respect to the pivot of the tilt mirror can be obtained following the grating equation and the ABCD matrix of the lens and free space (l_f) propagation of light. The phase shift $\phi(\lambda)$ can be expressed as [58]

$$\phi(\lambda)) = \frac{8\pi\sigma x}{\lambda} + \frac{8\pi\sigma l_f(\lambda - \lambda_0)}{p\lambda} \tag{3.2}$$

or

$$\phi(\omega) = \frac{4\sigma x\omega}{c} + \frac{8\pi\sigma l_f(\omega - \omega_0)}{p\omega} \tag{3.3}$$

where ω_0 is the center angular optical frequency. From the above equation the phase delay ($t_\varphi = \varphi(\omega_0)/\omega_0$) due to the tilted mirror can be shown as

$$t_\varphi = \frac{4\sigma x}{c} \tag{3.4}$$

Similarly the group delay ($t_g = d\varphi(\omega)/d\omega$) for $\omega=\omega_0$ can shown to be

$$t_g = \frac{4\sigma x}{c} - \frac{4\sigma l_f \lambda_0}{cp} \tag{3.5}$$

Thus the path length delay ($\Delta l_g = t_g.c$) can be expressed as

$$\Delta l_g = 4\sigma \left[x - \frac{l_f \lambda_0}{p} \right] \tag{3.6}$$

The first term in equation (3.6) represents the path length differences observed due to angular displacement of mirror. The second term of the equation 3.6 dominants over the first term yielding significantly larger path length delays even for small angular displacements. Using equation 3.4 and 3.6 it can be observed that the group path length difference is mainly governed by the design parameters i.e. l_f and p hence the offset x of the beam from the pivot of the tilt mirror, only affects the phase path length difference ($4\sigma x$) or the carrier frequency of the interference signal. This decoupling of the phase delay and group delay provides an important advantage that the carrier frequency of the interference signal could be set within the signal conditioning or the sampling frequency of digitization even for a high scan speed which is not possible for the mechanical translating scanners [58].

The other advantage of this scheme is that if the normal angle of the grating deviates from the optical axis of the lens, Group Velocity Dispersion (GVD) is introduced as the grating is also displaced from the focal plane of the lens [11]. Hence moving lens and resonant scanner simultaneously towards or away from the grating, the dispersion between the reference and sample arm of the interferometer can be minimized. This would help control the degradation of the axial point spread function due to unknown dispersion encountered in the sample.

For our design parameters 600 lines/mm grating rulings (grating pitch p=1.66 μm), l_f ~ 50 mm, 1-2 degree scan angle with 2 kHz repetition rate of the resonant scanner, λ_0 = 1310 nm and $\Delta\lambda$ = 43 nm the achievable parameters of the delay line are scan range ~ 3.5 mm, A–Scan rate 4 kHz (considering data acquisition for both backward and forward scan) and carrier frequency ~1.5 MHz.

The 4 kHz scan rate is sufficient to image at 8 frames per second with each frame consisting of 500 A-scans per frame. Even higher frame rate 16 (or 32) fps can also be achieved for lesser number of A-scans 250 (or 125) per frame. The scan range, 3 mm in this case, can be further increased by increasing the scan angle of the resonant scanner. This scan range is sufficient to image scattering biological tissue like skin. It should be noted that the carrier frequency and bandwidth of the OCT interference signal are also significantly higher for these delay lines therefore the sensitivity of the OCT measurements is compromised. This arises because at high speed data acquisition, the system dwell time per pixel decreases. Therefore, for a given input power a lesser number of photons are collected by the detector corresponding to one pixel location. To compensate for this, a higher power optical source is required to provide adequate illumination in a short amount of time. To improve the signal quality a balanced detection scheme was used. In Michelson interferometer only half of the light from reference arm and sample arm reaches to detector. The other half that returns towards the source is wasted. Further, in practical situations, the reference-arm light is significantly attenuated to optimize the SNR. To utilize the source power efficiently, the Michelson interferometer was replaced with a Mach-Zehnder interferometer, where using fiber optic circulators and unbalanced couplers, more power is directed to the sample which otherwise is lost in reference arm attenuation [59]. The details of the system implementation are discussed in the following section.

3.1.2 System implementation

A schematic of the real time TDOCT setup is shown in Figure 3.2. The system utilized a high power broadband SLD optical source (Dense Light, Singapore). The source has center wavelength 1310 nm with full-width at half-maximum 43 nm and 18 mW optical power in single mode fiber. Light coming from the source was introduced into a fiber based Mach-Zehnder interferometer which includes an 80/20 input coupler, two identical circulators one leading to the sample arm while the other leading to the reference arm, and a 50/50 detection coupler. The unbalanced coupler (80/20) pass the 80 percent source light to sample arm circulator (port 1) and the remaining 20 percent to the reference arm circulator (port 1). The sample arm comprises of a fiber collimator lens, a galvo-scanner mirror and a stationary assembly of relay lenses was used to deliver the light onto the sample. In reference arm of the interferometer, we employed a FDODL for a high speed depth scanning. The polarization controllers were used in the reference and sample arms to optimize the interference signal. The back reflected light from the sample and reference arms coupled back to the port 2 of the corresponding circulators. These circulators pass all the back-reflected light (via port 3) coming from both the reference and sample arms to a 50/50 coupler which equally distribute the OCT interference light to an adjustable gain trans-impedance InGaAs balanced photo-receiver. Since the interference signals at the two photodiode of the balanced detector are out of phase, the differential output of the balanced detector cancels the common mode noise and doubles the interference signal which leads to improvement of SNR. [43,59]. The output of the balanced detector was fed into a band pass filter and amplified further using a demodulating logarithmic amplifier. The demodulating logarithmic amplifier demodulates the amplitude modulated interferometric signal and detects envelope of the OCT interference signal. The output from the logarithmic amplifier was low pass filtered and then digitized using a frame

grabber board (Data Translation 3152, USA). The acquired data were used to generate cross-sectional images to display on the screen. The axial and lateral resolutions of the system are ~20 µm and the measured SNR of the system was ~ 92 dB. The theoretically estimated values of axial and lateral resolutions were ~ 17 µm and ~ 20 µm respectively and for SNR ~ 98 dB. The experimental values are quite close to the estimation. Some loss of resolution may arise due to deviation from the perfect matching of dispersion in sample and reference arms which leads to broadening of interferogram. Similarly losses in fiber will result in lower SNR than the theoretical estimated value.

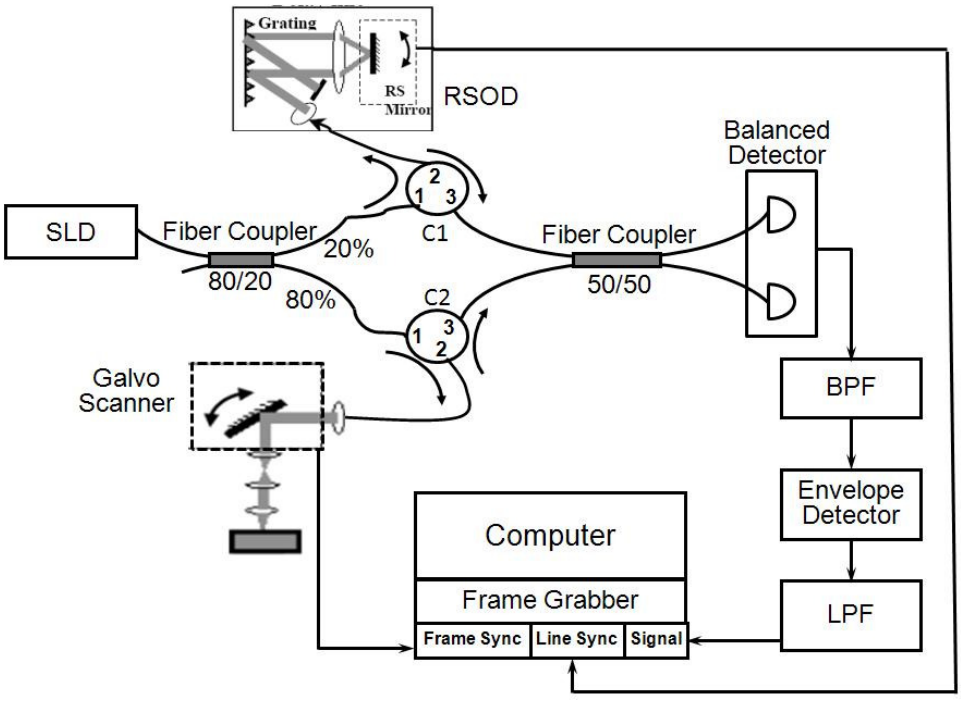

Figure 3.2: Schematic of time domain high speed OCT system. BPF: band pass filter; C1 & C2: circulators; LPF: low pass filter; RSOD: rapid scanning optical delay line; SLD: superluminescent diode.

A photograph of the OCT system is shown in Figure 3.3 (a). For ease in *in-vivo* imaging of various external parts of the body a hand held probe was developed. A photograph of the handheld probe suitable for dermatological applications is shown in the Figure 3.3 (b). A

typical image of the finger pad acquired with hand held probe is also shown in Figure 3.3 (c). Various anatomical structures of skin such as epidermis, dermis and sweat gland are distinguished in the OCT image. The diameter and the length of the dermal probe were ~ 30 mm and ~ 50 mm respectively. An oral probe of diameter ~15 mm and length ~150 mm was also designed for *in-vivo* imaging of oral cavity. The schematic of the oral probe is shown in Figure 3.3 (d).

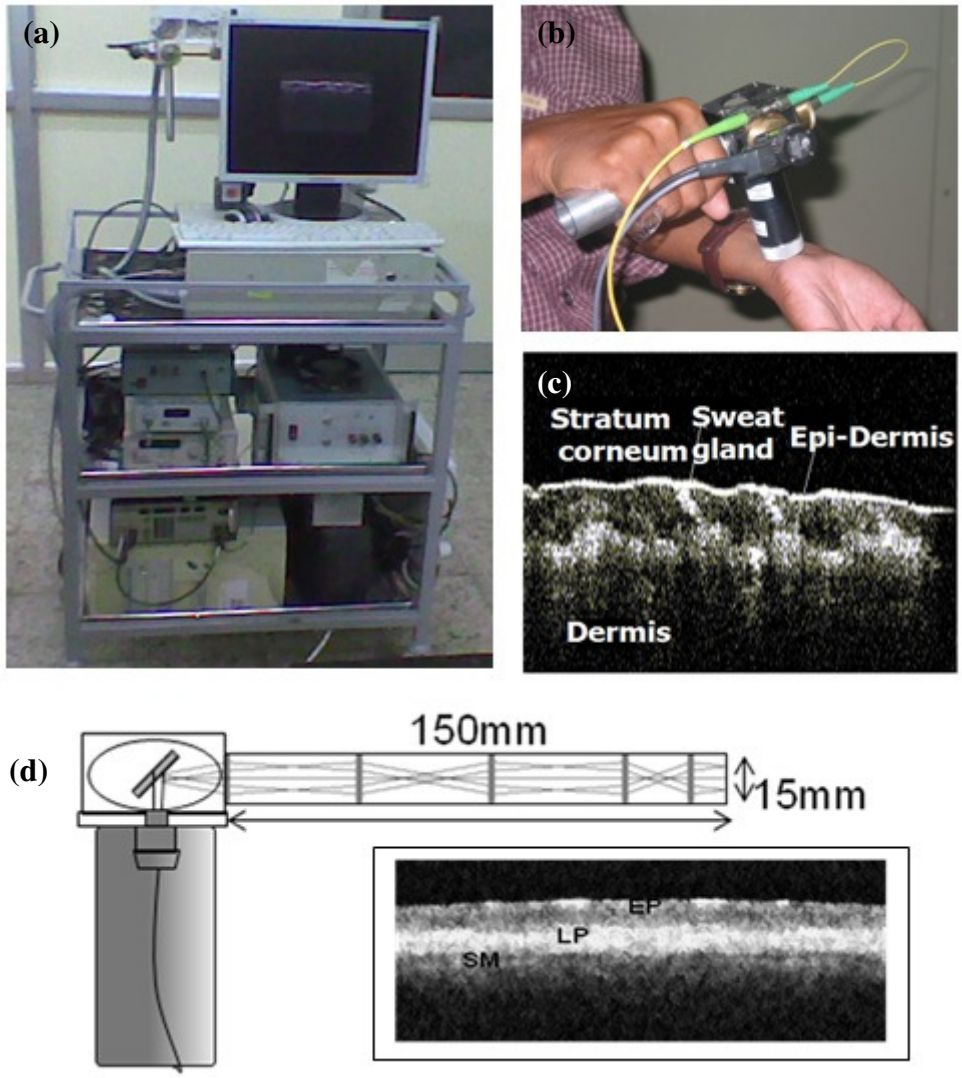

Figure 3.3: (a) photograph of the high speed OCT system; (b) photograph of hand held probe for *in-vivo* imaging of dermatological samples; (c) an OCT image of finger pad acquired with the hand held probe (size: 2.5 mm x 3 mm); and (d) the schematic of the developed oral probe with an image of oral mucosa (size: 2.5 mm x 3 mm).

Figure 3.4 shows a few representative OCT images acquired with high speed OCT system, (a) is an OCT image of a 0.2 mm pitch treaded screw and (b) is an image of oral mucosa. Different layers of the oral mucosa such as lamina propia, epithelium and sub mucosa are visible in the image. OCT images of nail, nail fold and palm are also shown in Figure 3.4 (c-e). Figure 3.4 (f) clearly shows the presence of a blister and the disjunction of the epidermis from the dermal layer and the signal free region due to edema.

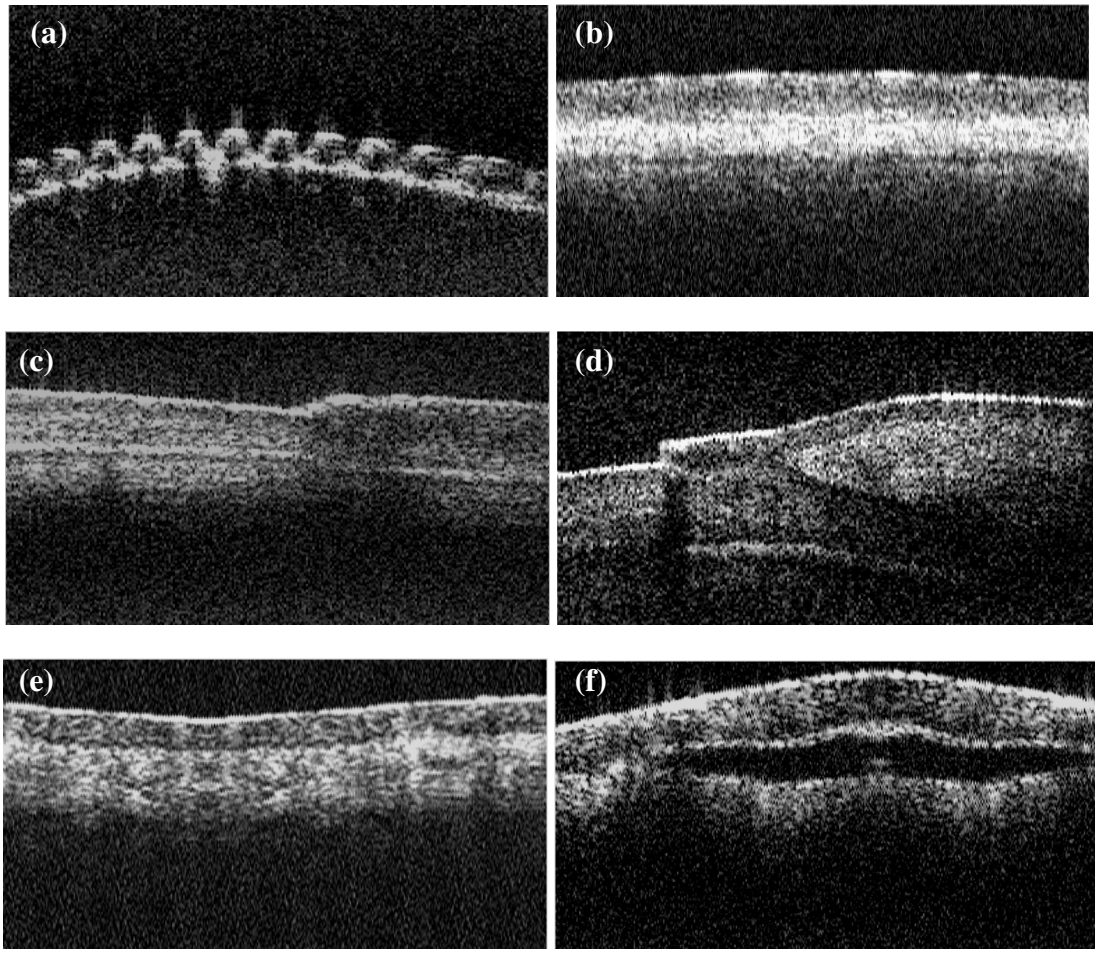

Figure 3.4: OCT images of (a) treaded screw (size: 2 mm x 2.5 mm), (b) oral mucosa, (c) finger nail, (d) nail-finger junction, (e) palm and (f) palm with blister. Size: a-f 2 mm (depth) x 2.5 mm (lateral).

3.2 Fourier domain OCT setup

Imaging speed of the TDOCT system is limited by the speed of reference arm scanning and because of higher repetition rate, reference arm scanning leads sensitivity degradation [60]. Fourier domain depth ranging allows high imaging speed without compromising the sensitivity. Although this concept of depth ranging was demonstrated within a couple of years of time domain OCT development, it took about a decade to fully understand and demonstrate that the Fourier domain detection has a better sensitivity advantage over time domain detection [17,18]. A prime reason for this delay could be the unavailability of the fast imaging devices (CCD) required to support the high speed imaging [14].

In FDOCT detection approach, the interference of the reference and sample arm light is optically dispersed on a linear detector array and Fourier transform of the interference spectrum is used to retrieve the depth information. Therefore, information about the entire axial structure of the object is collected simultaneously in "single shot" eliminating the need for scanning in the reference arm which also facilitates enhanced image acquisition speeds [61, 9]. Owing to its superior sensitivity over the conventional TDOCT, it has undergone rapid development and has proved to be a promising technique for clinical and biological applications [8].

Figure 3.5 shows the basic scheme of FDOCT setup. Light from a low coherent source is split into the sample and reference arms of the interferometer and the back reflections from the stationary reference mirror and sample recombine to generate interference fringes. In FDOCT approach a spectrograph is used in the detection arm of the interferometer which disperses the light and records the spectrum of the interference signal. The measured wavelength component of the interference intensity signal can be written as:

$$I_D(k) \propto S(k)\left[\left|E_R\right|^2 + \left|E_S\right|^2 + 2\left|E_R\right|\left|E_S\right|\mathrm{Re}[\Upsilon(\tau)]\cos(\frac{2\pi}{\lambda_0}2z)\right] \tag{3.7}$$

where *S(k)* is spectral intensity distribution of the light source, *2z* is the round trip optical path difference between reference and sample arms, λ_0 is the wavelength of the source and $\Upsilon(\tau)$ is the complex degree of coherence. The first term of the above equation corresponds to the intensity of the reflected reference beam which is barely the measurement of source spectrum. The second term corresponds to the beams reflected from different layers within the sample. However, the amplitude of this term is very small in comparison to other terms. The third term represents the interference of the reference beam with sample beam. For a given optical path difference between reference and sample arms, the measured interference signal is a cosine function of modulation frequency. The depth resolved back scattering information of the sample is encoded in modulation frequencies superimposed on the light source spectrum such that the amplitude of each cosine is proportional to the sample reflectivity. The modulation frequency (in *k*-domain) varies linearly with an increase in the optical path delay between reference and sample fields. The depth resolved reflectivity profile of the sample can be obtained by performing the Fourier transform of the recorded modulated spectrum. It should be noted that the Fourier domain OCT can also be implemented using a swept laser source and a single photodiode. Instead of dispersing the interferometric light signal by means of spectrograph, the interference spectrum can also be measured by sweeping the wavelength of the swept laser and measuring the interference signal using a single detector. Both of these approaches provide the interference spectrum which can be Fourier transformed to obtain depth resolved scattering. The first approach is generally referred as spectral OCT (also spectral radar) while the later is known as swept source OCT (also optical frequency domain OCT).

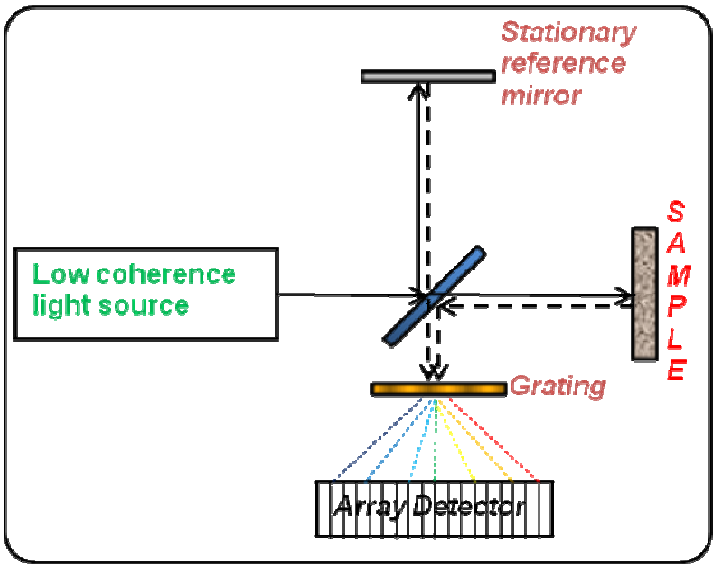

Figure 3.5: Basic scheme of FDOCT approach.

Figure 3.6 (a) shows a typical interference spectrum for a mirror like object which can be called as interference signal in *k*-domain. The FFT of the measured spectrum provides the depth resolved reflectivity profile in spatial domain, as shown in Figure 3.6(b). Two mirror peaks one on either side of the center peak (located at the centre of the plot in the spatial domain) corresponding to the negative and positive optical path delay. Similarly Figure 3.6 (c and d) show the interference spectrum for a multilayer sample and corresponding depth profile after performing FFT. It should be noted that to avoid the overlapping of the desired signal from the negative distance (or negative frequency signal) and zero delay peaks, it is general practice to keep the object surface away from reference plane with an offset z_0 (~ 2 or 3 times of l_c).

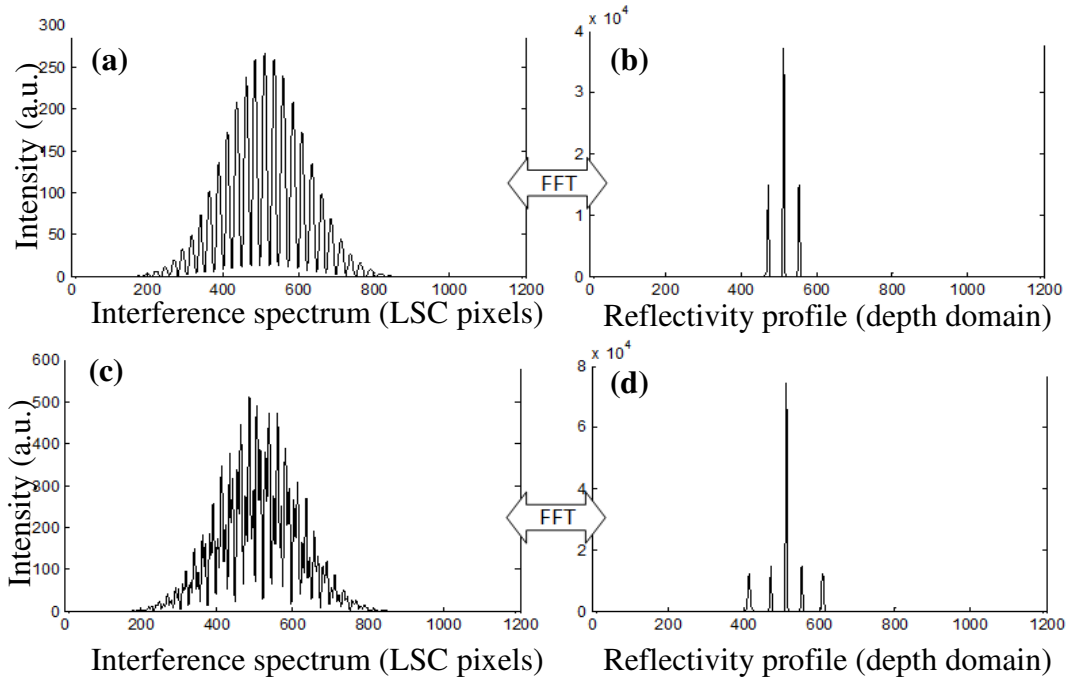

Figure 3.6: Typical interference spectrum (a, c) and corresponding A-scan (b, d) after performing FFT.

The axial and lateral resolution of the FDOCT system is similar to the TDOCT system. The axial (δz) and lateral resolutions are determined by the coherence length of the source and the NA of the objective lens respectively. In a FDOCT system, the output intensity spectrum $I(\lambda)$ is a set of N discrete data points corresponding to an intensity measurement at each detector in the CCD or photodiode array. The Fourier transformation of the recorded intensity spectrum results in a series of N discrete data points. Since the recorded intensity spectrum is a real valued sequence, FFT of this is conjugate symmetric, therefore only half of the data sets i.e. N/2 is available for depth information. From equation 3.7 it can be observed that a large optical delay between the object and reference beams will result a high modulation frequency in the spectrum. According to the sampling theorem the sample frequency of the photodiode array has to be twice as large as the highest occurring frequency in the spectrum. For z_{max} the period of the cosine fringes is

$\delta k n z_{\max} = \pi$ where n is the refractive index of the medium. Hence the maximum achievable distance is $z_{\max} = \pi / (n\delta k)$ [61]. For $|\delta k| = 2\pi\delta\lambda / \lambda^2$

$$z_{\max} = \frac{1}{4n}\left(\frac{\lambda_0^2}{\delta\lambda}\right) \tag{3.8}$$

Hence, for a source having centre wavelength λ_0 = 800 nm and bandwidth $\Delta\lambda$ = 50 nm, and detector array consists of N ~ 1000 elements the achievable maximum axial scan depth for a sample is z_{max} ~ 2 mm. The maximum axial scanning depth scales linearly with the number of detector elements. Therefore imaging range can be increased by increasing the number of pixels of the detector array. It should also be noted that the higher pixel numbers of the detector array leads to better sensitivity of the measurements because the amplitude of the Fourier component is proportional to the number of illuminated pixels of the camera times the modulation depth of the spectrum. However the larger pixel number takes longer time to execute FFT and affects image display rate.

3.2.1 System implementation

Figure 3.7 shows a schematic of the FDOCT setup. A 5 mW superluminescent diode source with FWHM of 40 nm centred at 840 nm was used as a light source. A 2x2 3 dB single mode fiber coupler was used to realize a Michelson interferometer. At the distal end of the sample arm a lens collimates the beam and a galvo-scanner driven with a saw-tooth waveform was used for transverse beam scanning on the sample. A focussing lens focused the beam on the sample surface with estimated spot size of ~20 μm. In reference arm of the interferometer the collimated light was reflected by a static reference mirror. The light returned from the two arms was recombined and directed to the spectrometer placed at the detection arm of the interferometer. In the spectrometer, the interfered beam was first collimated with a 50 mm focal length lens and then dispersed by a volume phase

transmission holographic grating of 1200 lines/mm (Wasatch Photonics, UT, USA). A 150 mm focal length imaging lens Fourier transform the dispersed beam onto the line scan camera (2048 pixels, 14 µm pixel size Atmel, CA, USA). The line scan camera (LSC) was operated at 10 kHz readout rate corresponding to the 100µs integration time. A frame trigger generated by a function generator in synchronization to that saw tooth waveform was used to trigger the data acquisition. The data from the LSC was digitized by a PCI-1428 (National Instruments, TX, USA) camera link image acquisition board. NI-IMAQ software was used under LabView™ environment for data acquisition and subsequent processing.

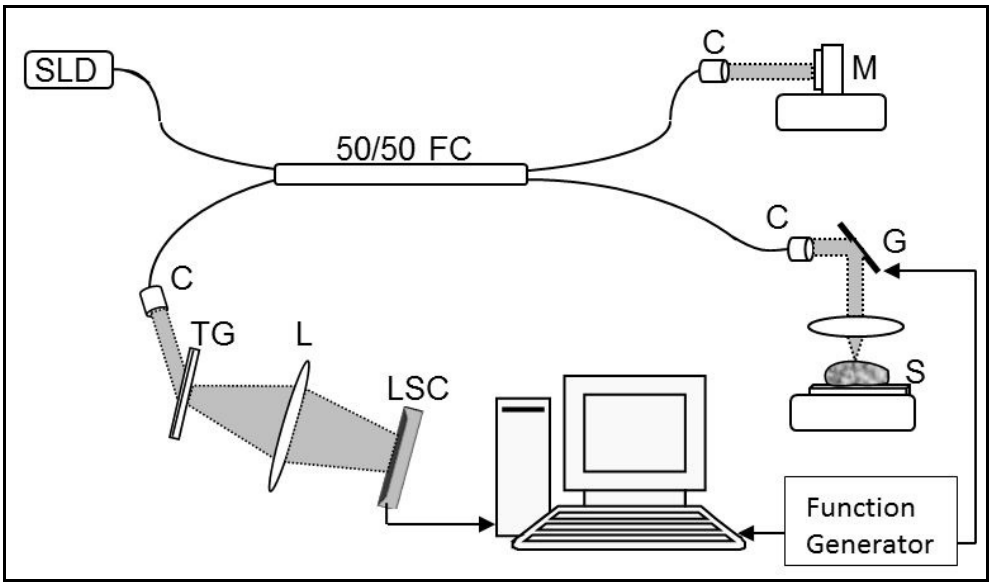

Figure 3.7: Schematic of FDOCT setup. C: collimator lens; G: galvo-scanner; L: imaging lens; LSC: line scan camera; M: reference mirror; S: sample; SLD: superluminescent diode; TG: transmission grating.

Since the physical distance z is conjugate to wave number k, the depth profile (A-scan) is obtained by taking Fourier transformation of the measured interference spectrum.

It should be noted that the data collected by the spectrometer are sampled with equal wavelength increments and are not evenly spaced in *k*-domain since $k \propto 1/\lambda$. This leads to a broadening of the PSF function with the increase of the optical delay between sample and the reference. Figure 3.8 (a) shows the A-scans measured for different optical distances between the reference mirror and an object (first interface of a thick glass plate). The depth resolution degrades as the optical distance between object and reference mirror increases. A proper depth profile can be obtained only after interpolating the acquired data and making interference spectrum evenly spaced in *k*-domain [60]. Hence the acquired spectra are pre-processed prior to FFT in Labview graphical tool. The pre-processing first reduces the DC background and fixed pattern noise. For that an average of 1000 reference spectrum, acquired at the time of imaging by blocking the sample path, is subtracted from each acquired interference spectrum. The DC subtracted interference spectrum is transformed from evenly sampled λ to evenly sampled *k*-domain by means of cubic spline interpolation. The FFT of the resultant data was then taken to construct the structural images. Figure 3.8 (b) shows the set of A-scans where FFT is performed after re-sampling of the measured spectrum. It can be observed that the axial resolution as well as the amplitude of the A-scans was significantly improved. The time taken to process a single 2D image (containing 800 spectra corresponding to different lateral location of the sample and 1024 pixels per spectrum) with DC subtraction, interpolation and FFT is approximately ~5 seconds. For realtime (online) display of the acquired images FFT is performed directly on the acquired interference spectrum and the other processing is done off-line on the saved data. In online mode the display rate of the images is ~10 Hz for an image consisting of 512 (axial) x 1000 (lateral) pixels. By further increasing the read out rate of the LSC (maximum ~29 kHz for our LSC) it can perform video rate imaging. The system is capable of performing OCT imaging with measured sensitivity of ~ 95 dB. The

measured axial resolution of the FDOCT setup is ~12 µm with achievable imaging depth close to 2 mm.

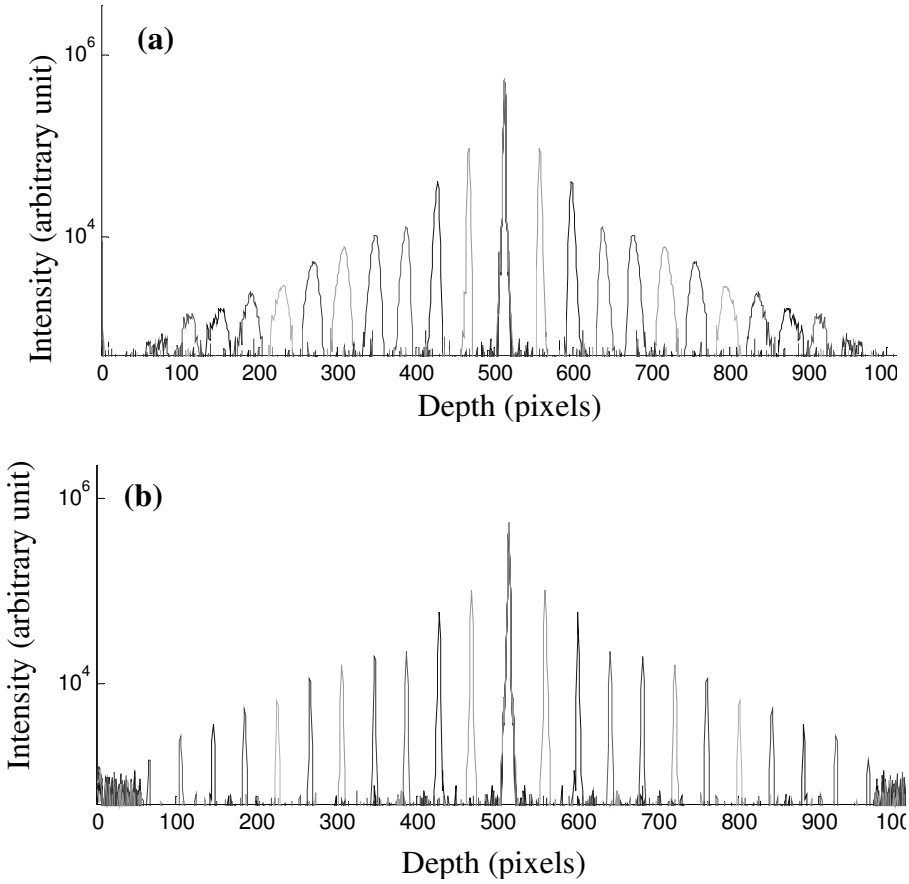

Figure 3.8: Set of A scans measured for different optical delays between the reference mirror and object. (a) FFT performed without resampling and (b) after resampling.

Figure 3.9 shows the representative OCT images of biological tissues using FDOCT setup at 10 Hz frame rate. The OCT image of (a) human nail fold, (b) skin (back side of the finger), (c-d) finger pad, and (e) onion is shown in the figure. The sweat gland and thick epidermal layer (due to thicker stratum corneum) with ridges of the finger is seen in the image (c) and (d). The significant difference between the thicknesses of the epidermis is observed in the images acquired from finger pad and the skin from the back

side of the finger. The realtime *in-vivo* imaging ability of the FDOCT setup with sensitivity sufficient to image biological as well as non-biological objects makes it a valuable tool for research as well as clinical importance.

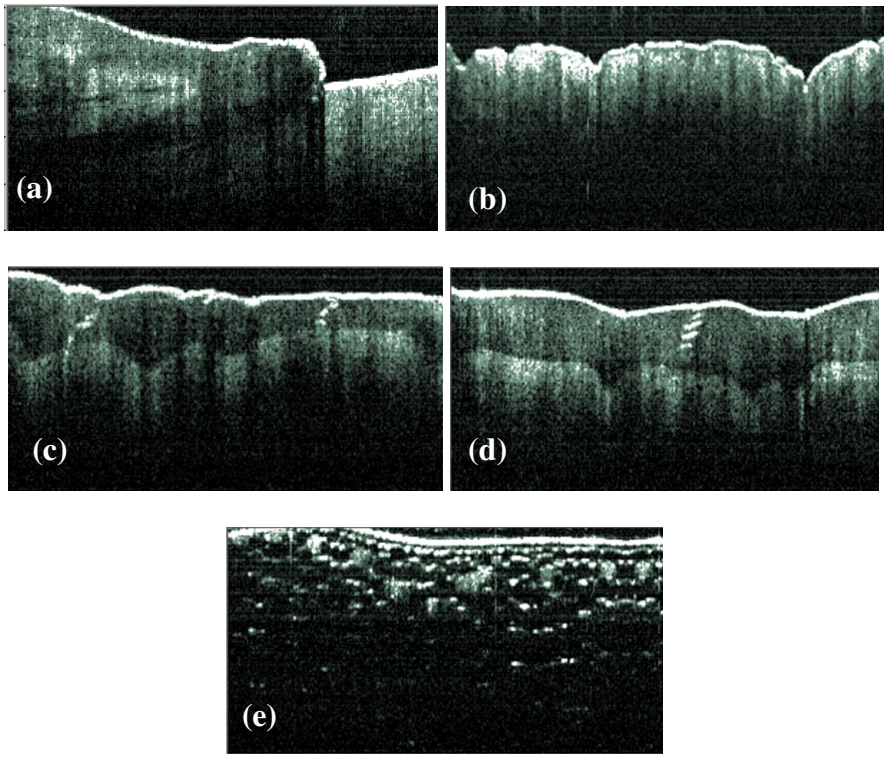

Figure 3.9: OCT images of biological tissue samples (a) nail fold, (b) skin back side of the finger, (c and d) finger pad and (e) onion using FDOCT setup. Image size 1.25 mm (depth) x 3 mm (lateral).

3.3 Summary

A TDOCT setup operating at 1310 nm was developed to provide high resolution (~ 20 µm) high speed image acquisition required for the use of OCT to perform *in-vivo* imaging. The setup employed a rapid scanning Fourier domain optical delay line which provides 4 kHz A-scan rate and allows acquisition of images at 8 frames per second (an image

consisting of 500 A-scans per image). Hand held probes were also developed for imaging of dermatological and oral cavity tissues. To further improve the imaging speed and axial resolution without sacrificing the sensitivity, FDOCT setup was developed. The FDOCT setup measures the backscattered interference light in *k*-space which can be transformed in spatial or depth domain by performing the Fourier transform of the interference spectrum. These setups were used to demonstrate *in-vivo* OCT imaging of various biological tissues.

CHAPTER 4: UTILIZATION OF TDOCT SETUPS FOR IMAGING ZEBRAFISH

Abstract: In this chapter we describe the results of our studies on the utilization of TDOCT setups for non-invasive, high resolution imaging of the different organs of Zebrafish, a vertebrate model system widely used for studies on ocular development and a variety of human diseases. The ocular images obtained using TDOCT setups could be used to measure corneal and retinal thickness and refractive index profile of the lens. A three dimensional iso-surface model of Zebrafish brain was also reconstructed using high resolution (~ 20 μm) two dimensional OCT images and the major structures of the brain could be clearly seen.

4.1 Introduction

Zebrafish, a popular aquarium fish (Figure 4.1) has life cycle of about 2-3 years. At the age of 3 months it is sexually reproductive and lays 100–200 rapidly developing embryos per week in each clutch [62,63]. The embryos develop externally to the mother and are also completely transparent for the first few days which facilitate easy observation of embryonic development using microscopy. These features of Zebrafish make them a good system for laboratory experiments [64,65]. Zebrafish has also proved to be an important model organism particularly for the developmental research which includes formation of neural connections in the retina and brain, understanding the visual behaviour and the

underlying mechanisms of retinal image formation, etc. Various mutants have been identified in Zebrafish that have relevance to human disease like retinal defects. For studies in these areas, measurement of several ocular parameters of the Zebrafish, like refractive index of the crystalline lens, mean retinal thickness, etc. are required. Most of these measurements have been carried out on extracted eye samples [66]. We have investigated the use of OCT for non-invasive measurements of the ocular parameters and for imaging of other internal organs like brain.

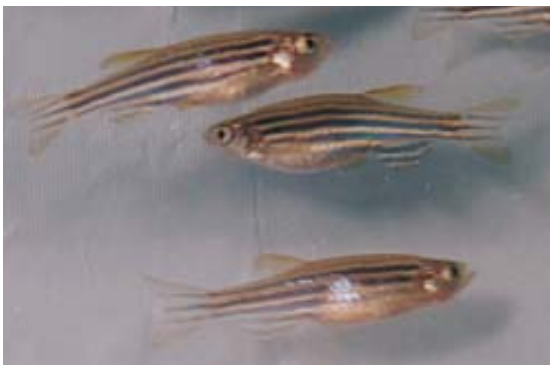

Figure 4.1: A photograph of adult Zebrafish.

4.2 Non-invasive imaging of intra-ocular structures of adult Zebrafish eye

Zebrafish were procured from local suppliers. For *in-vivo* imaging, the fish was anaesthetized using clove oil following the protocol given by Grush *et al.* [67]. Briefly, clove oil was dissolved in ethanol (1 : 10) and then mixed in 1 liter of water in a glass tank, such that the clove oil concentration was about ~ 75–100 ppm. The fish lost physical movement within 10 minutes. When the fish showed no response to physical stimulus, it was transferred to a petri dish for imaging. The fish was observed to revive within ~ 1 h after which it was transferred to a freshwater tank. In Figure 4.2 *a,* we show the *in-vivo*

OCT image of the whole eye of the anesthetized Zebrafish. While the cornea, the anterior angle region, and the retina are clearly seen, the lens is not visible in the image due to index matching of the lens surface with the surrounding fluid. During the course of several experiments, it was found that the lens could be imaged with better contrast after dipping the fish in a petri dish containing 10% formalin solution for ~ 15–30 min. In Figure 4.2 *b*, we show the image of the fish eye after it was dipped in 10% formalin solution. The lens (L) as well as other ocular structures like cornea (C), iris (I), and retina (R) can be clearly seen.

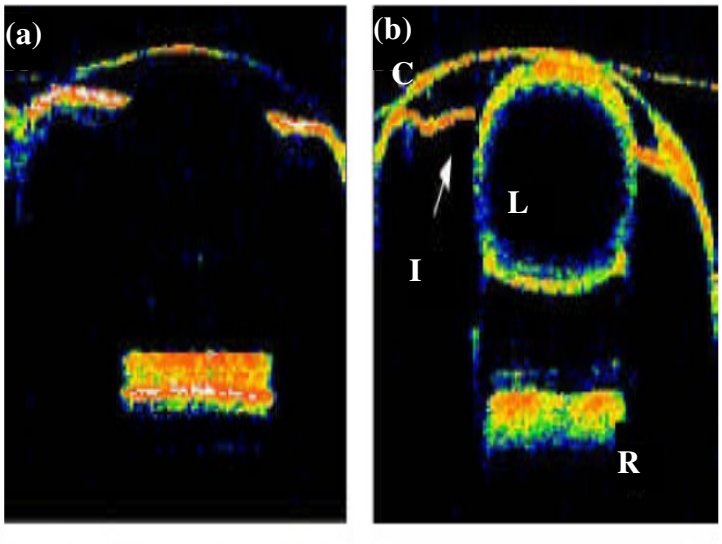

Figure 4.2: OCT images of whole eye of Zebrafish (a) under anesthesia, and (b) ~ 30 minutes dipped in 10% formaline solution. Image size: 3 mm (depth) and 2 mm (lateral). Abbreviations: L-lens, C-cornea, I-iris, and R-retina.

Figure 4.3 (a) shows the *in-vivo* image of the cornea of Zebrafish. The image features are in good agreement with the reported images of Zebrafish eye obtained using light microscopy [68]. Corneal thickness in fish is an important parameter that is affected by environmental stress and infection. The maximum corneal thickness was measured to be ~ 34 µm. Assuming a corneal refractive index of 1.33, the geometrical thickness of

Zebrafish cornea, in the region where the OCT light is perpendicular to the cornea, turned out to be 26 µm (± 11 µm). In their experiments on Zebrafish cornea extracted from dissected eyeballs, Swamynathan *et al*. [68] estimated its thickness to range from 16 to 20 µm. The difference in the two measurements may be due to the difference in the protocol and may illustrate the usefulness of *in-vivo* measurements. It should be noted that since the resolution of our set-up is ~ 11 µm, we could not resolve the epithelium layer of the cornea, which has thickness of ~ 8 µm [68]. Use of an ultra-high resolution OCT set-up will be required for quantitative comparison of corneal thickness and microstructures therein. The anterior chamber angle is another important parameter in the structure of the eye. Narrowing of this angle increases the risk of glaucoma. Non-invasive measurement of anterior chamber angle is therefore vital for characterization of structural changes in the anterior region and changes in the intraocular pressure (IOP). *In-vivo* imaging of the anterior chambers of different mutant variants of Zebrafish may help in better understanding of the genesis of glaucoma. Figure 4.3b shows the *in-vivo* OCT image of the anterior region of the eye. The anterior chamber angle of the cornea with the iris is clearly visualized. Figure 4.3c shows the expanded OCT scan of the Zebrafish retina with the layered structure. Due to the small retinal thickness and poor axial resolution compared to histology, only broad categorization is possible. The first reflective interface posterior to the lens at the top of the image in Figure 4.3c represents the anterior border of the retina (vitreo–retinal interface) with the retinal nerve fibre layer (RNFL) at the vitreous interface. The outermost band is thought to be that of the retinal pigment epithelium (RPE) choriocapillaris complex showing high scattering. Assuming a retinal refractive index of 1.38 and considering the band above RPE, the retinal thickness can be estimated as 123 ± 11 µm. For comparison a mean retinal thickness of ~ 85 µm for wild-type Zebrafish was

reported by Link *et al*. [69]. The difference in these values could be due to the fact that the measurements reported by Link et al. were on resected eyes.

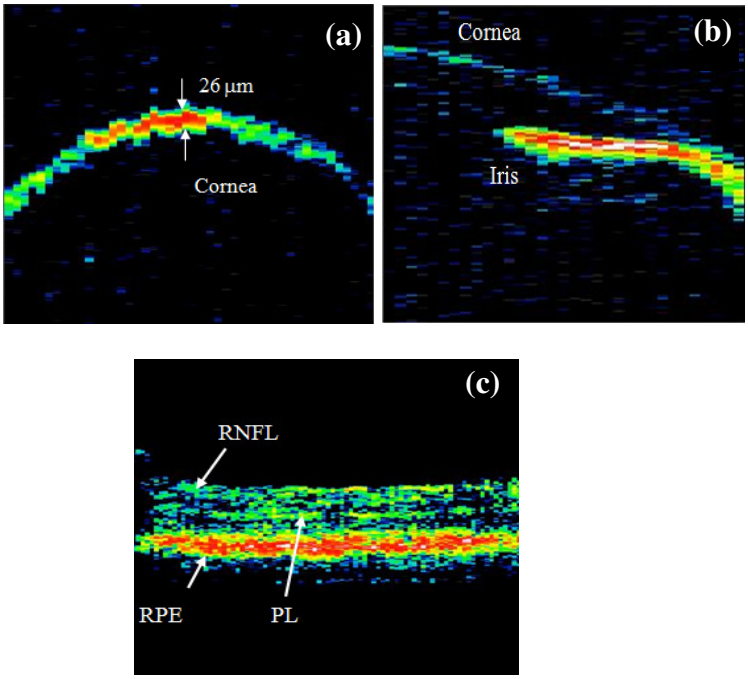

Figure 4.3: (a) *In-vivo* OCT image of cornea of Zebrafish. Image size 0.4 mm (depth) x 0.9 mm (lateral); (b) *In-vivo* OCT image of anterior angle of the cornea with the iris of Zebrafish. Image size 1.3 mm (depth) x 0.7 mm (lateral); (c) *In-vivo* OCT image of retina of Zebrafish. Image size 1 mm (depth) x 0.7 mm (lateral).

In Figure 4.4 we show the OCT image of the whole eye of a Zebrafish, dipped in 10% formalin solution. Along the apex of the lens (when the OCT beam was exactly perpendicular to the cornea) some scattering inside the lens was also seen, indicating that the crystalline lens has gradually varying refractive index as a function of depth. It is pertinent to note that although the lens of the fish eye is known to be spherical in shape, the diameters of the lens as measured by OCT were different along the axial and lateral directions. This is because, while in axial direction the measured diameter is the optical length of the lens (geometrical path x effective refractive index), in the lateral direction it

is the true geometrical diameter. The difference in the ratio of the measured diameters can be used to estimate the effective index of refraction of the lens medium. From the image shown in Figure 4.2b, effective refractive index of ~ 1.43 was estimated for the Zebrafish crystalline lens at the centre wavelength of the source (840 nm). The crystalline lens of the fish is usually assumed to be spherical with a gradient refractive index that varies from approximately 1.35–1.38 at the surface to 1.55–1.57 at the core of the lens [70,71].

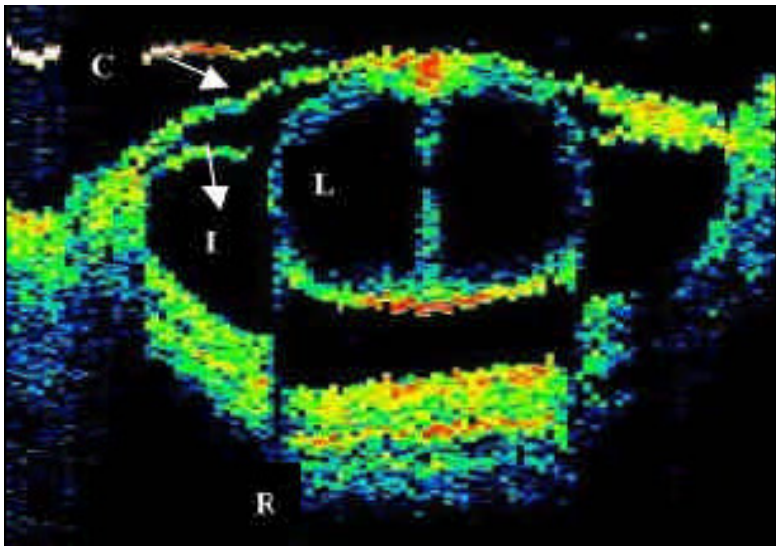

Figure 4.4: OCT image of whole eye of Zebrafish. Size of the image is 3 mm in axial and 2.2 mm in lateral direction.

The refractive index of the fish lens was also measured using focus-tracking method described by Wang *et al.* [72]. The sample arm light was focused using a high numerical aperture microscopic objective (20X) with the focal plane set initially at the top surface of the lens. This was achieved by monitoring the intensity of the A-scan peak, and maximizing the corresponding peak of the lens surface. Once the focus was set at the top of the lens surface, the objective was moved a distance Δx such that the bottom surface of the lens came in focus. The corresponding change in the reference mirror position (Δy) to

get the A-scan peak intensity was noted. The effective refractive index was determined using the expression [72]

$$n^2 = \frac{1}{2}\left[NA^2 + \sqrt{NA^4 + 4\left(n_0{}^2 - NA^2\right)\left(\frac{\Delta y}{\Delta x}\right)^2} \right] \tag{4.1}$$

where n_0 is the refractive index of the surrounding medium of the tissue. Before applying this technique to fish lens, we used it to measure the refractive index of quartz window. The measured value of 1.445 @840 nm was found to be in good agreement with the reported value [72].

From the measurements, we estimate the effective (integrated) refractive index of the fish lens as ~ 1.43 @ 840 nm within 3% rms deviations. The effective refractive index can also be computed assuming the refractive index variation along the beam direction to be of parabolic form [73] given by

$$n(z) = n_0 \sqrt{1 - z^2 / a^2} \tag{4.2}$$

where n_0 is the maximum refractive index at the centre of the lens and a is a constant that indicates the steepness of the gradient in the refractive index. The effective refractive index of the lens (n_{eff}) as seen by the OCT beam is then given by

$$n_{eff} = \frac{\int_{-r}^{+r} n(z)dz}{2r} \tag{4.3}$$

is the total optical path along the apex of the lens as seen by the OCT beam and r is the radius of the spherical lens. Using OCT, r was measured to be 0.46 mm. The index of the lens surface is reported to be in the range 1.35–1.38 at 632.8 nm [70,71]. As the OCT reflection (@ 840 nm) from the lens surface was feeble, we assume the index at the lens surface to be close to water. We calculated the effective refractive index from equation 4.3 using different values of core index n_0 in the range 1.54– 1.59. Using n_0 = 1.54 yields

effective refractive index n_{eff} ~ 1.47, closer to the experimentally measured value. The relative error in the estimation of effective refractive index of the crystalline lens using the OCT method can be estimated by

$$\frac{\delta n_{eff}}{n_{eff}} = \frac{\delta D_z}{D_z} - \frac{\delta D_x}{D_x} \tag{4.4}$$

where D_z is the diameter of the lens along the axial direction, D_x is the diameter of the lens along the lateral direction, and dD_z and dD_x are the uncertainties in measurement of the diameters along the axial and lateral directions respectively. Using the values dD_z ~ 11 µm (axial resolution), and dD_x ~ 27 µm (lateral resolution with 5× objective), the relative error $|dn_{\text{eff}}/n_{\text{eff}}|$ is estimated to be ~ 2%. Taking the measured value of n_{eff} ~ 1.43, the absolute error in the effective refractive index estimate is dn_{eff} ~ 0.03. To the best of our knowledge, there are no experimental measurements of refractive index of intact Zebrafish lens. Even though the fish could not be revived after these measurements, it did not require separation of the lens from the fish eye unlike the previous studies by Garner *et al.* [70], where MRI was used for determination of graded index of fish lens after physical separation.

4.3 Measurement of gradient refractive index profile of Zebrafish crystalline lens

It is known that the spherical lens of Zebrafish has a gradient refractive index profile for correcting the large spherical aberrations to be expected from a spherical lens. There exists considerable interest in determining the refractive index profile of crystalline lenses. Several techniques are employed for this purpose such as the Abbe refractometer, interference technique, and laser ray tracing methods [70,74,75]. These require either

sectioning or resection of the lens. Magnetic resonance imaging (MRI) can be used for non-invasive measurement of the refractive index profile of the fisheye lens. However, it is not suitable for measuring the refractive index in the core region of the lens due to the absence of free water [70]. Recently a tomographic method reported for the measurement of the gradient refractive index of a spherically symmetric lens which later has been extended to rotationally symmetric lenses [71,76]. Here, we present the use of OCT for non-invasive measurement of the gradient refractive index profile. In OCT, the backscattered signal is detected only when the optical path length of the light in the reference and the sample arm matches within the coherence length of the source [10,14]. Since, the path length in the reference arm is known, the optical path length in the sample arm and thus the position of the reflecting structure can be calculated. OCT can thus detect the backscattered or reflected light at front and back surfaces of the lens, respectively, and provides a direct measurement of the optical path length of the ray passing through the lens. The optical path of the ray inside the lens can be computed using ray tracing, assuming a polynomial form refractive index profile. Thus by fitting the measured optical path length with the optical path calculated using a ray tracing algorithm, coefficients of the index profile can be extracted. The approach has been employed for determining the index profile of a fisheye lens under both resected and intact (*in-vivo*) conditions. The slow speed TDOCT setup which uses a motorized translation based reference arm scanning for depth ranging was used to image Zebrafish eye. The details of the setup are discussed in chapter 2 of the thesis. In the sample arm was collimated focused on to the sample with a 5× microscopic objective (NA ~ 0.1). It should be noted that to achieve depth of focus ~ 1mm as required for this study, we purposely under filled the objective to reduce its effective NA. While the clear aperture of the objective was 5 mm, we kept the width of the collimated beam incident on it ~ 1 mm, so that NA reduces to ~0.02. This

resulted in a focal spot size (Δx) ~ 27 µm and the corresponding depth of focus was ~ 1.3 mm. Due to the large depth of focus, the beam size can be assumed to be constant throughout the lens.

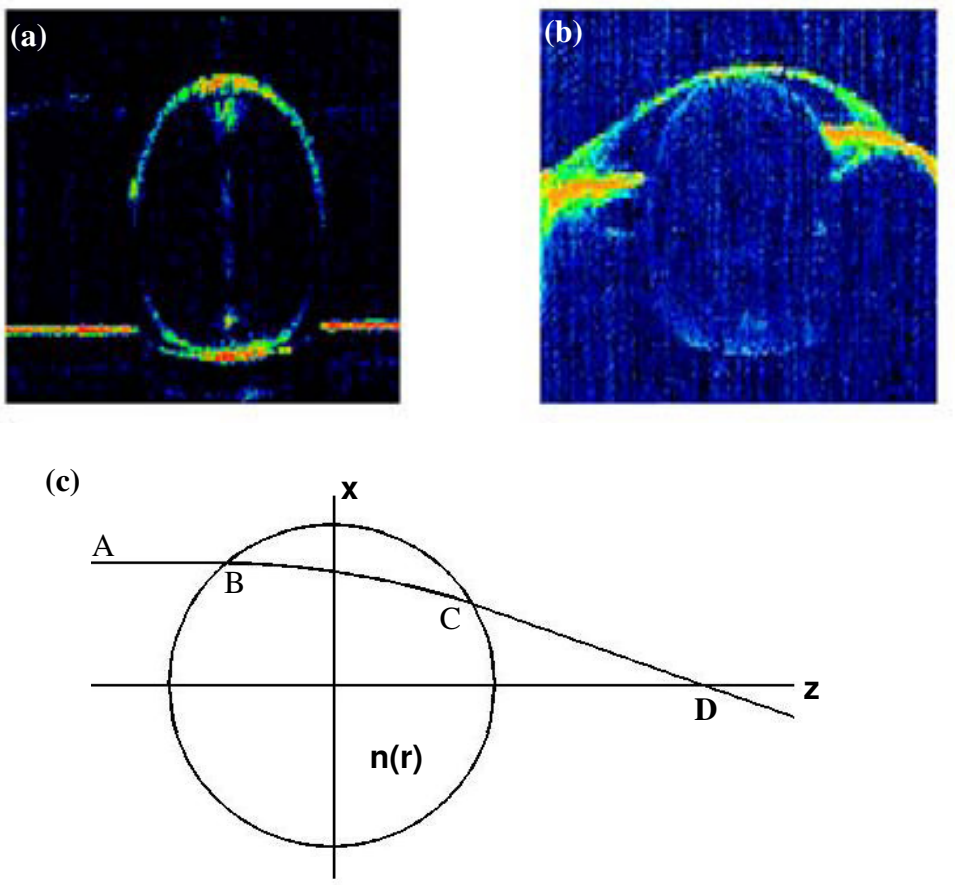

Figure 4.5: OCT images of (a) resected and (b) *in-vivo* Zebrafish eye lens; (c) ray diagram of light propagation through a graded refractive index spherical lens.

In order to acquire a two-dimensional image of the lens, the fish/resected eye lens was put on a linear translation stage that was controlled by a stepper motor. Unlike angular scanning of the beam for two-dimensional retinal imaging used in OCT, a parallel beam of light was translated across the pupil for imaging of the lens. For *in-vivo* imaging, the fish

was anaesthetized using clove oil as discussed in the previous section. Following the loss of physical movement (within 10 minutes.) and response to physical stimulus, it was transferred to a petri dish for imaging. After imaging, the fish was transferred back to a fresh water tank for its revival. A typical OCT image of a resected fisheye lens is shown in Figure 4.5 a. Figure 4.5 b shows the image of a fisheye structure in the meridional plane acquired *in-vivo*. The images consist of a number of A-scans (depth scans) at different transverse locations of the sample. From these images, the optical path length of the incident light rays that travelled through the lens was measured. These measured data was then used as the experimental input data for fitting with the path calculated from the assumed polynomial form refractive index profile [77]. To retrieve the gradient refractive index profile, we consider a spherical lens with radius *R*. In a radial gradient medium, the gradient refractive index profile is normally represented by a polynomial with only even powers of *r* [75, 78]:

$$n(r) = \sum_{j=0}^{3} a_j r^{2j} = a_0 + a_1 r^2 + a_2 r^4 + a_3 r^6 \tag{4.5}$$

and $r = \dfrac{\left[(x^2 + z^2)^{1/2}\right]}{R}$

where *r* is the normalized radial distance from center to edge. This is attributed to the fact that if a linear term in *r* was present, the paraxial theory would no longer apply and no useful imaging can be obtained and in presence of the other odd terms the effect on aberrations can be serious [79].

Consider a collimated beam of light passing through the lens as shown schematically in Figure 4.5 c. The ray A experiences refraction at point B on the surface of the lens. Afterwards, due to the refractive index gradient of the crystalline lens, the ray follows a curved path. It emerges from point C at the back surface of the lens and intersects the optic

axis at point D. The optical path inside the lens can be obtained evaluating $\int_B^C n(r)ds$ where *ds* is arc length along ray path [80]. For retrieval of the refractive index, optical path lengths measured from the OCT images i.e. BC_{expt} needs to be fitted with the calculated theoretically optical paths i.e. BC_{theo} for a given gradient refractive index profile. The theoretical optical paths i.e. BC_{theo} were calculated using the ray tracing method reported by Sharma *et al*. [80] in the following manner:

In gradient refractive index medium the propagation of the ray is governed by the following expression [80]

$$\frac{d}{ds}\left[n(r)\frac{dr}{ds}\right] = \nabla n(r) \tag{4.6}$$

where $n(r)$ is the gradiented index medium, $\boldsymbol{r}$ is the position vector and ds is the length along the ray. Equation 4.6 can be modified to transform it in a numerically solvable form:

$$\frac{d^2R}{dt^2} = \frac{1}{2}\nabla n^2 \approx n\nabla n \tag{4.7}$$

Where $t = \int \frac{ds}{n}$ or $dt = \frac{ds}{n}$;

The modified variables R and D are defined such that the above equation 4.6 transform in to a second order differential equation as below:

$$\frac{d^2R}{dt^2} = D(R) \tag{4.8}$$

Where $R = (x, z)$; and $D = n(dn/dx, dn/dz)$. An optical ray vector $T = n(dx/ds, dz/ds)$ can be defined as $T \equiv dr/dt \equiv ndr/ds \equiv \hat{i}n\cos\alpha + \hat{k}n\cos\gamma$, where α and γ are angles ray direction makes with xy and z axes respectively. The above matrix Equation 4.8 can be

solved to generate successively (R_1, T_1), (R_2 ,T_2), …, (R_n.T_n) points for a given initial condition using (R_0,T_0) using Runge-Kutta algorithm as below [80]:

$$R_{n+1} = R_n + \Delta t[T_n + \frac{1}{6}(A + 2B)],$$

$$T_{n+1} = T_n + \frac{1}{6}(A + 4B + C), \tag{4.9}$$

where the matrices A, B, and C are defined as

$$\begin{aligned} A &= \Delta t D(R_n); \\ B &= \Delta t D\left(R_n + \frac{\Delta t}{2}T_n + \frac{1}{8}\Delta t A\right); \\ C &= \Delta t D\left(R_n + \Delta t T_n + \frac{1}{2}\Delta t B\right) \end{aligned} \tag{4.10}$$

where Δt is the step size for the computation for desired accuracy. Optical path BC_{theo} can be calculated by measuring the arc length for every step along the ray (inside the lens only) and multiplying it with refractive index calculated for that particular point in the lens. The coefficients a_j were retrieved with the use of the nonlinear least squares curve-fitting algorithm that minimizes the difference between theoretically calculated optical path (BC_{theo}) and the optical path length measured experimentally (BC_{expt}) from the acquired OCT images i.e.

$$\sum_{m=1}^{M}[BC_{theo}^{m} - BC_{\text{exp}t}^{m}]^2 \tag{4.11}$$

where M is the total number of rays measured for different lateral shifts and

$$BC_{theo} = \sum\left(\sum aj\left|\frac{(R_{n+1} + R_n)}{2}\right|^{2j}\right) \times \left|R_{n+1} - R_{n-1}\right| \tag{4.12}$$

where R_n is the position vector of a grid point and n is chosen such that R_n is within the lens. For quantitative estimation of the errors, random noise corresponding to

measurement inaccuracy of 11 μm was added to the optical path length data. This leads to uncertainties in the coefficients of the refractive index profile (i.e., a_j) ~ 10^{-3}. The maximum error in refractive index due to these uncertainties was estimated to be ~ 0.013. The size of the beam also affects the uncertainties in the refractive index estimation. For a beam width of ~ 27 μm at the sample, the maximum error in refractive index was estimated to be ~ 0.012. The increase in beam width reduces the number of data points and therefore increases the uncertainties in estimating the coefficients, and hence the refractive index. For example, for a spot size ~ 100 μm the error in the refractive index was estimated to be ~ 0.016. We have also used the images for the measurement of the index profile in the *Y–Z* plane. As expected, the refractive index profiles in the two orthogonal planes were found to be the same.

Table 4.1: Optimized coefficients for refractive index profile

Samples		Radius (mm)	a_0	a_1	a_2	a_3
In-vitro	1	0.46	1.545	-0.117	-0.034	-0.034
	2*	0.46	1.540	-0.109	-0.032	-0.037
	3	0.45	1.545	-0.119	-0.033	-0.033
	4	0.62	1.543	-0.113	-0.033	-0.032
In-vivo	5	0.48	1.544	-0.116	-0.035	-0.036
	6	0.48	1.545	-0.125	-0.031	-0.029

* Measurement for orthogonal plane of sample 1

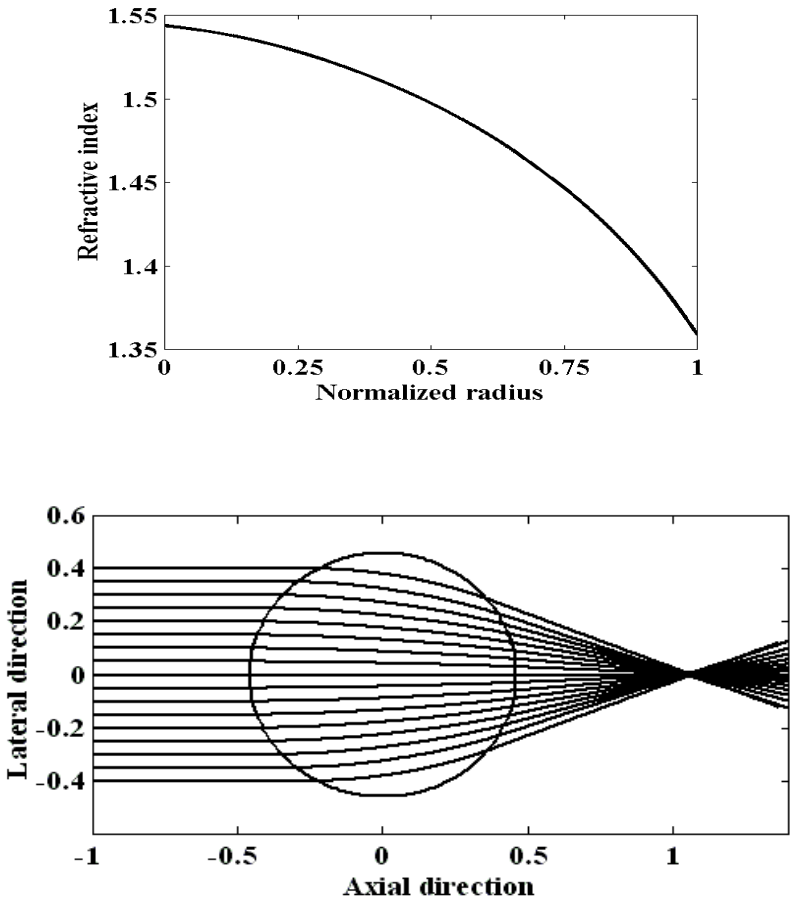

Figure 4.6: (a) Refractive index profile obtained from the mean values of coefficients of Table 4.1. (b) Ray paths for the refractive index profile shown in (a).

The optimized coefficients of index profile obtained from the resected lens and the *in-vivo* measurements are shown in Table 4.1. The polynomial form refractive index profile obtained from the mean values of coefficients (Table 4.1) is shown in Figure 4.6 a. A gradual decrease in refractive index from ~ 1.54 to 1.36, from the core to the edge of the lens, can be seen in the figure. The difference between the group and phase index values for the case of the crystalline lens of the fisheye, was estimated to be ~ 0.05 using the reported ocular dispersion values [81]. The ray paths for a polynomial form refractive index profile obtained from the mean values of coefficients are shown in Figure 4.6 b. The

equivalent focal length (distance from center of lens to focal point) of the lens is seen to be 1.06 mm and the corresponding Matthiessen's ratio, defined as the ratio of the focal length of the lens to its radius, was estimated to be~ 2.30. These values are in very good agreement with the values reported in the literature [78]. It is important to note here that the optimized coefficients of the gradient refractive index profile indeed lead to small spherical aberrations (longitudinal and transverse). The marginal rays focus closer to the lens than the paraxial rays. For an aperture of 0.85*R*, the calculated values of longitudinal spherical aberration (LSA) defined as the distance between the focal point of the marginal rays and the focal point of the paraxial rays is ~ 55 μm which significantly smaller for a lens of size ~ 0.9 mm.

4.4 *In-vivo* imaging of Zebrafish brain

The real time OCT setup was used to acquire two-dimensional cross sectional images (XZ plane, as shown in Figure 4.7) of the brain of anesthetized Zebrafish and a 3D model of Zebrafish brain was reconstructed. About 90 cross-sectional images of the brain were acquired by moving the sample in the Y direction. The acquisition time for each 2D cross-sectional image was 0.125 s. Around 90 images were acquired in the XZ plane by manually moving (50 μm) a micrometer controlled stage along Y-axis. The major lobes of the brain such as bulbus olfactorius, telencephalon, tectum opticum, cerebellum, frontal bone and eminentia granularis were clearly distinguishable in these images [82]. The raw images were thresholded for minimizing the speckle noise. Using these images, a three-dimensional model of the Zebrafish brain was constructed (Figure 4.8) with AMIRA software. The iso-surface brain model so developed was found to be in resemblance to the model reported previously [83]. We also compare the OCT images with the Zebrafish brain images posted on the VCCRI fishnet website [84] database. The images shown on

fishnet website are of 17 mm length (adult) fish taken with optical projection tomography [85]. The fishnet data base images do not clearly show the structure of bulbus olfactorius and Eminentia granularis. The other structures such as telencephalon, frontal bone, tectum opticum and cerebellum are resolved better in OCT images than the reported images on fishnet database. The cavity inside tectum opticum is clearly distinguishable in our images compared to the fishnet database. Due to the presence of a highly scattering layer in the hind portion of the Zebrafish brain the structures beyond the cerebellum such as crista cerebellaris, medulla spinalis, parasphenoid, palatoquardrate, etc. were not clearly distinguishable. It is pertinent to note that the adult Zebrafish used in this study was ~35 mm long. In a fish of smaller size (few days old) the internal structures of brain could be better visualized with good contrast. Further, using OCT set up with higher sensitivity (~ 110 dB), one can distinguish the anatomical structures more effectively. The 3D imaging of the internal structures of brain helps rendering of data for better visualization and understanding of the features. *In-vivo* 3D imaging of an adult Zebrafish brain demonstrates the capability of OCT to monitor the developmental changes even for adult Zebrafish when it becomes turbid and unable to visualize under microscopy techniques.

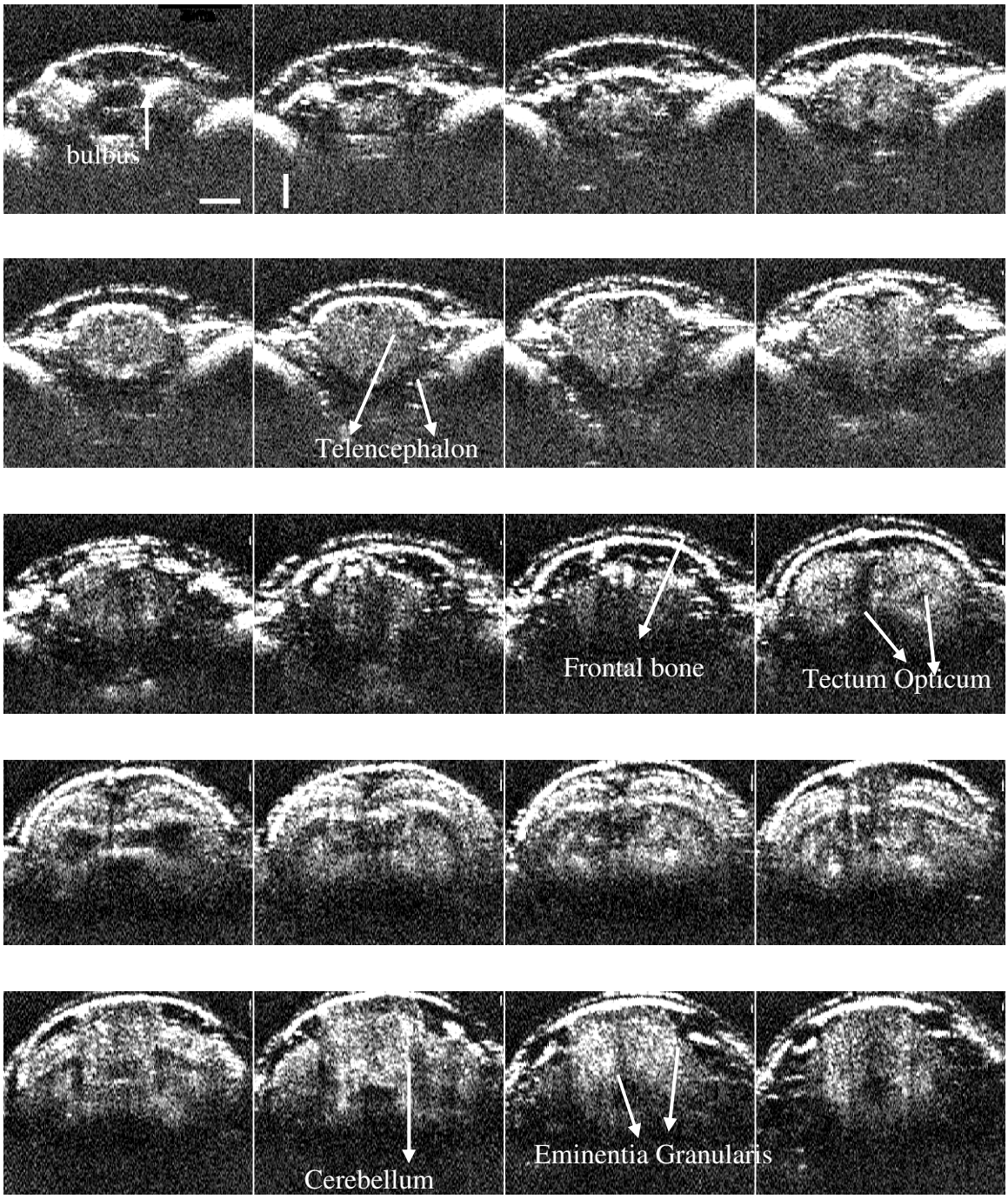

Figure 4.7: Cross-sectional images of Zebrafish brain displayed at an interval of 150 μm (The horizontal and vertical bars denote 0.5 mm length)

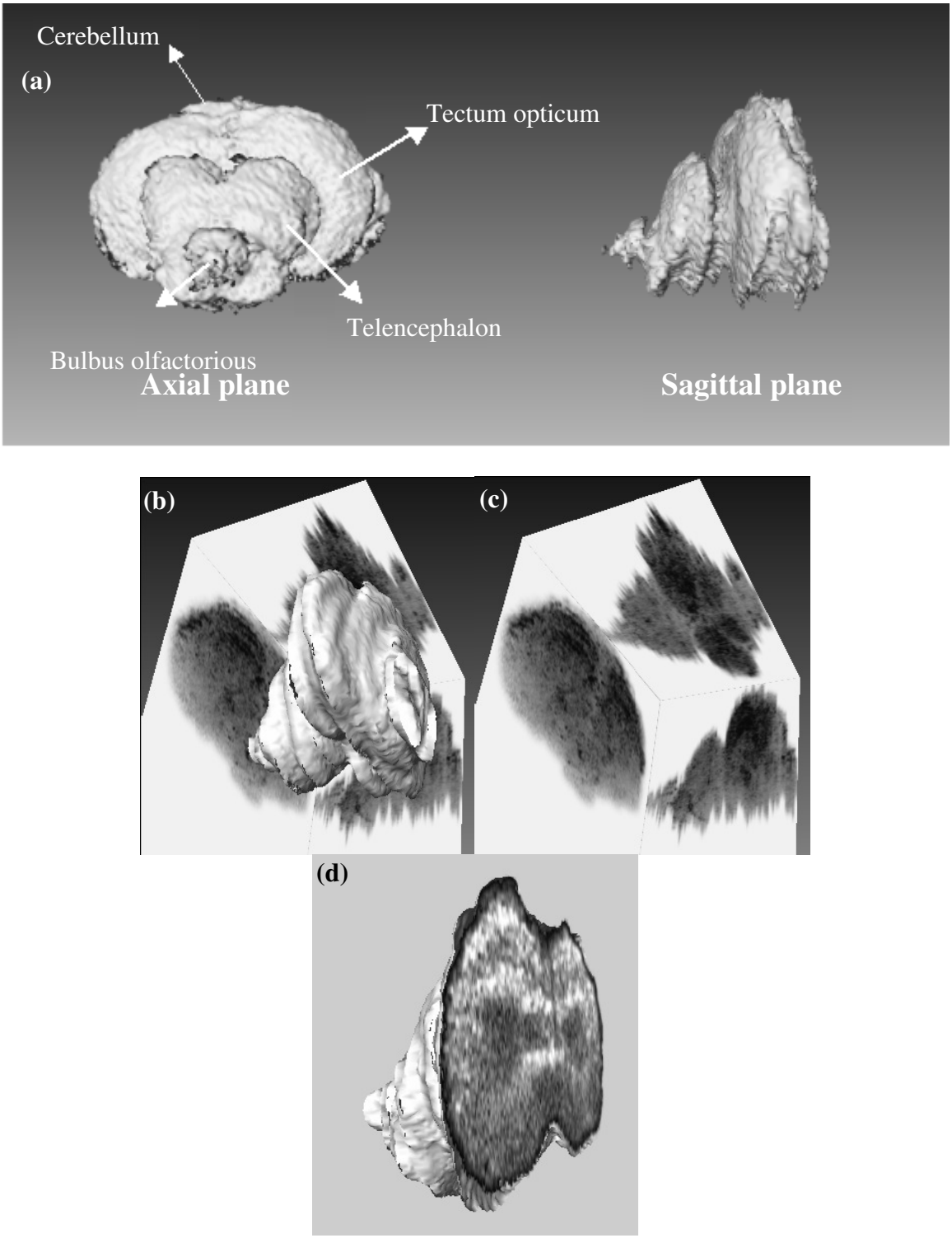

Figure 4.8: (a) 3-D image of adult Zebra fish brain in axial and segittal plane, (b-c) Orthogonal projection image of brain; (d) crossection of brain in axial plane.

4.5 Summary

We have utilized the OCT setups developed by us to image the various ocular structures of Zebrafish eye such as cornea, iris, eye lens and retina with an axial resolution of ~10 µm and measured various ocular parameters such as corneal thickness, retinal thickness and equivalent refractive index of Zebrafish eye lens. We also successfully demonstrated the use of OCT for non-invasive measurement of the refractive index profile of the eye lens. For the latter we exploited the fact that since OCT provides direct measurement of the optical path length, the gradient refractive index profile can be retrieved by iterative fitting of optical path calculated by ray tracing method with that experimentally measured using OCT at various lateral locations of the sample. The 3D optical imaging of brain at speed (@ 8 fps) and with resolution significantly better than obtained by other techniques like MRI and computed tomography was also demonstrated. The three dimensional images of Zebrafish brain reconstructed using two dimensional OCT images clearly show the major structures of the brain such as bulbus olfactorius, telencephalon, tectum opticum, cerebellum, frontal bone and eminentia granularis.

CHAPTER 5: UTILIZATION OF OCT SETUPS FOR MEASUREMENT OF BIREFRINGENCE AND ELASTIC PROPERTIES OF BREAST TISSUES AND FOR MONITORING GROWTH DYNAMICS OF TUMOR SPHEROIDS.

Abstract: In this chapter we describe the use of OCT for quantitative assessment of the birefringence and elastic properties of resected human breast tissue samples. The estimated values of birefringence obtained from the PSOCT imaging showed that the benign breast tissue samples have significantly higher birefringence as compared to the malignant tissue samples. Further, using OCT based elastography measurements, the stiffness coefficients of these tissue samples were also quantified. A significant difference in the stiffness coefficients of the three breast pathologies, normal, benign and malignant, was observed. The use of OCT to monitor the growth dynamics of tumor spheroid non-invasively is also discussed. Here, the study showed that in comparisons with microscopy (which provides only 2D information) the volume estimates provided by OCT were in much better agreement with the total cell count of tumor spheroids measured using hemocytometer.

5.1 Introduction

It is known that breast cancer is often accompanied by fibrosis [86]. Since collagen fibers are birefringent, it is expected that the neoplastic changes would lead to changes in the polarization parameters which can be monitored by polarization sensitive measurements. Further, since the mechanical properties of breast tissue depends on its structural organization, any alteration in the organization results in significant variation in the mechanical properties of different pathological tissues. These macroscopic differences in the mechanical properties of the breast tissues have been the basis of the conventional approach of manual palpation for the detection of breast tumors. We have investigated the use of the OCT and PSOCT setups for measurements of the birefringence and stiffness coefficients of the breast tissues to discriminate among the normal, malignant and benign tissue sites.

We have also used OCT to monitor growth dynamics of tumour spheroids. Tumor spheroids are three-dimensional cell cultures that mimic the avascular solid tumours. Studies have shown that the tumour spheroids exhibit structural, metabolic, functional and growth patterns similar to that of solid tumours. These are therefore, a good model system for understanding tumor growth and its organization. Tumour spheroids are also being increasingly used for studying response of solid tumours to photodynamic therapy [87, 88, 89].

5.2 Resected human breast tissue samples

Pathologically characterized tissue samples were obtained from the Pathology Department of CHL-Apollo Hospital, Indore. The tissue samples were kept preserved in formalin

(10%) at room temperature (~ 24° C). Tissue samples from only those patients were included in the study for which the histopathological diagnosis was unambiguous. The histo-pathological report provided by the histopathologist was taken as the gold standard for this study. The samples were of three categories: normal fatty adipose tissues, fibroadenoma (benign tissues) and invasive ductal carcinoma (malignant tissues). The normal tissue samples were obtained from uninvolved areas of the resected cancerous and benign specimens based on histopathologist's assessment.

5.3 Measurement of birefringence of breast cancer tissue using PSOCT

In Figure 5.1 we show the intensity images of breast tissue samples of different pathologies. The intensity and birefringence (or retardation) images of breast cancer tissues were acquired using PSOCT setup discussed in chapter 2 (section 2.6.1). The OCT image of normal tissue, which is primarily composed of large sized lipid-filled adipocytes [90], is shown in Figure 5.1A (i). The spatially periodic highly scattering boundaries seen in the image can be attributed to the large adiposities. In contrast to the low-scattering patterns of adipocytes of normal tissue, the abnormal tissues (malignant Figure 5.1A (ii) & fibroadenoma 5.1A (iii)) show relatively dense and homogeneous scattering which could be due to increased cell density in tumor tissue [90]. Using the intensity image, while it was possible to discriminate abnormal from normal it was difficult to discriminate between malignant and the benign tumor tissue. The retardation images of the same tissue samples in gray scale are show in Figure 5.1B. For normal breast tissue as in the OCT intensity image, the retardation images show the adipocytes boundaries only. However for malignant and benign tumor, in contrast to intensity images the retardation images show

marked differences. The transition from black to white band in benign PSOCT image represents the change in the accumulated phase retardation from 0 to π/2.

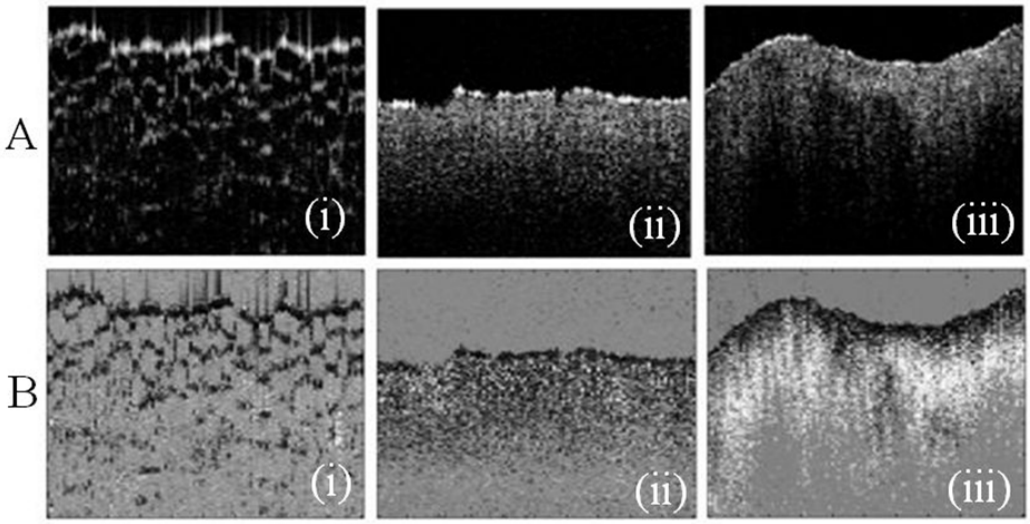

Figure 5.1: (A): Intensity images (i) normal, (ii) malignant, and (iii) benign of resected breast tissue samples. (B): Retardation images (i) normal, (ii) malignant, and (iii) benign of resected breast tissue samples. Image size: 1 mm (depth) × 2mm (lateral).

Figure 5.2 shows the calculated phase retardation as a function of the depth for malignant and benign samples respectively. The malignant tissue samples display a phase retardation plot increasing at a slower rate in comparison to benign tissue samples, indicating a lower birefringence. The birefringence (Δn) of the sample can be calculated by a measurement of the slope of the phase retardation profile along the depth using the following expression [91]

$$\Delta n = slope \times \lambda / 2\pi \tag{5.1}$$

where λ is the wavelength of the source used.

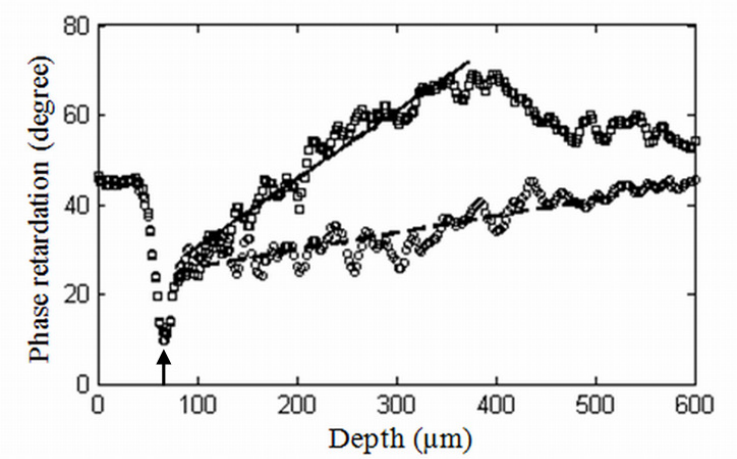

Figure 5.2: Phase retardation depth profile of malignant (circle) and benign (square) breast tissue. The linear fitting of the depth profile is shown by solid (benign) and dashed (malignant) lines. The arrow shows tissue top surface.

The mean birefringence value of benign samples averaged over 12 different samples ($4 \pm 1 \times 10^{-4}$) was significantly higher ($p < 0.001$, t-test) than that of the malignant tissue ($8.0 \pm 3.0 \times 10^{-5}$). These changes can be attributed to the fact that the fibroadenoma has more ordered collagen which contributes to an increased birefringence as compared to the malignant breast tissue [92,93]. The results indicate that the PSOCT can be used as a potential tool for effective discrimination of breast tissue samples.

The feasibility of PSOCT to discriminate the normal, benign and malignant breast tissue samples has significant potential for tissue diagnosis and identification of tumor margins of normal and abnormal tissue. In Figure 5.3 we show a representative image or identifying the tumor margin. The arrows in the image differentiate the normal tissue from the tumor tissue. The image region left side of the arrows shows the cell boundaries of the adipocytes cells while the right region of the image shows the dense scattering of tumor tissue.

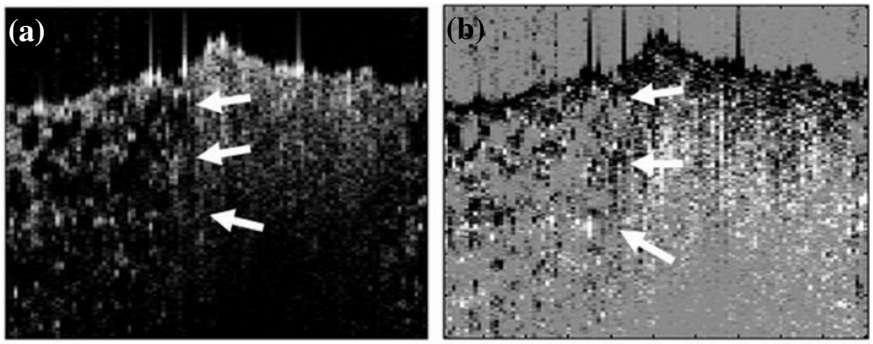

Figure 5.3: (a) Intensity and (b) retardation images of breast tissue. Arrows show the tumor margin. Image size: 1 mm (depth) × 2 mm (lateral).

5.4 Measurements of elastic properties of resected human breast tissue samples

Several elastography techniques such as ultrasound elastography, magnetic resonance elastography, etc. have been used to estimate or assess the changes in the mechanical properties of the tissues under compression at a microscopic level. These techniques are based on the principle that by applying a known pressure on the tissue sample and by measuring the induced strain in the sample, information about the mechanical properties (e.g. tissue stiffness) can be extracted. Optical elastography which includes micro-/nano-speckle method (electron speckle photography), diffusing wave spectroscopy (DWS), etc., offers the potential for increased spatial resolution and better strain resolution as compared to ultrasound and magnetic resonance elastography techniques. OCT has also been used for elastographic measurement of the biological tissues. Schmitt [94] reported the measurements of displacements as small as a few micrometers in heterogeneous gelatin phantoms containing scattering particles in addition to human skin as a function of depth

under a compressive load using OCT-elastography. This technique has also been applied for the investigation of arterial wall biomechanics [95,96], atherosclerotic plaques [97,98], and engineered tissues [99].

For measurement of stiffness coefficients, OCT has been used to image displacements induced within the resected human breast tissue samples subjected to external axial compressive loads. A speckle-tracking technique based on two-dimensional cross correlation of successive OCT images (pre-compressed and post-compressed) was employed for a quantitative measurement of the induced local speckle displacements. Resultant strains at each pixel have been calculated using the two-dimensional displacements maps for normal, benign and malignant breast tissue samples. The stiffness of each sample has been quantified in terms of the modulus of elasticity using the stress-strain relationship. To validate the methodology of OCT elastography measurements including the speckle-tracking method, the overall data reduction approach has been examined by estimating the elastic properties of tissue-mimicking gelatin phantoms. The procedures applied for phantom preparation and OCT elastography measurements are based on the method suggested by Rogowska *et al*. [98].

Figure 5.4(a) shows a schematic diagram of the loading arrangement employed to compress the tissue samples. The tissue compression unit consists of an L-shaped metallic plate mounted on a stepper motor vertical translation stage. The resolution of the motorized translation stage is 4 μm. Here the metallic plate acts as the loading component. The translation stage traverses in the vertical direction, which in turn moves the metallic plate, and the plate compresses the tissue sample in the axial (downward) direction. The horizontal arm of the L-shaped metallic plate has a clear hole of about 5 mm diameter in the middle to allow the OCT probe beam to pass through. A cover slip placed on the top of

the sample serves as an optical window as well as a compression plate. The objective lens in the sample arm of the OCT setup focuses the light beam on the tissue sample. As the translation stage is lowered, an approximately uniform pressure is applied to the sample, compressing its surface along the axis of the sample beam. Axial load exerted on the sample (after correcting for the weight of the sample holder) is monitored using a load cell kept below the sample holder. The resolution and maximum capacity of the load cell employed in the present work are 4.9×10^{-4} N and 4.9 N respectively. In the experiments, the relaxation of load for a particular imposed displacement was found to be quite small ($\leq$ 5%). Furthermore, this variation has been taken care of by using an average of initial and final values of axial compressive loads for the determination of elastic properties of the tissue samples. To monitor the uniformity of the pressure applied on the tissue surface, the displacements of the top layer of the tissue was measured for different values of compressive loads. Across the region of imaging (~ 2 mm), nearly uniform displacement of the top layer in the downward direction was observed for a given value of compressive load, confirming the uniformity of the pressure applied. This also confirms the establishment of full contact of the metallic plate with top surface of the tissue samples. The response of the breast tissue samples under axial compressive loading is shown in Figure 5.4 (b). The figure shows average displacements of the top surface of normal and malignant samples with respect to the axial load. It can be seen that the tissues exhibit nearly linear mechanical behaviour up to a value of ~ 0.30 mm of the average displacement of the top layer under compression. In the experiments reported in the present work, the maximum displacement of the top surface of the tissue samples (corresponding to the maximum load applied) was about 240 µm. The analysis for the determination of elastic coefficients of tissue samples was carried out within this limit wherein the force-displacement response of the samples is nearly linear.

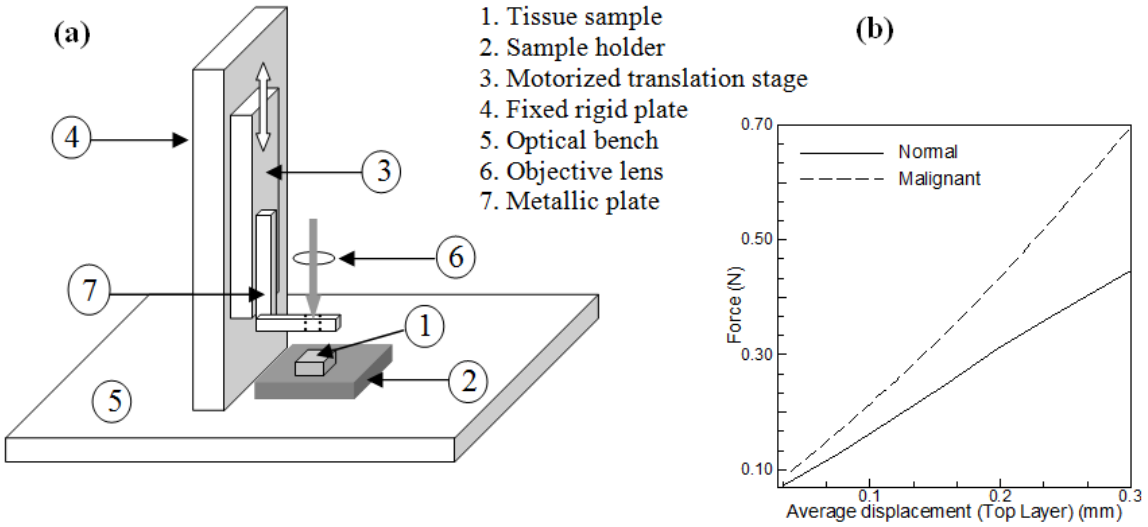

Figure 5.4: (a) Schematic of arrangement for compressive loading of tissue samples; (b) plot of the force versus average displacement of the top surface of normal and malignant breast tissue samples.

5.4.1 Phantom preparation

For preparation of tissue phantoms, a mixture of gelatin (800 mg) and agarose (100 mg) was dissolved in 6 ml of boiling water and the solution was continuously stirred to avoid the formation of lumps within the solution. A fixed amount of activated charcoal particles (25 mg) was added in the solution as the scattering centers. The mixture was poured into a Petri dish (40 mm diameter) and refrigerated for several hours. After refrigeration, the phantoms were cut into 20 mm × 20 mm × 4 mm thick squares, covered with a glass slide of thickness ~1.5 mm and were subjected to axial compressive loading using an arrangement schematically shown in Figure 5.4(a). The original and compressed phantoms were scanned with OCT at an axial resolution of 11 µm.

5.4.2 Displacement and strain calculation

The interpretation of OCT images is usually based on the visualization of the two-dimensional, cross-sectional microstructures within the tissue samples. To derive quantitative information from the recorded OCT images, several data processing steps are required. In the present work, a speckle-tracking method based on two-dimensional cross-correlation technique has been employed to derive displacement and strain information from the OCT images of pre-compressed and post-compressed breast tissue samples and tissue-mimicking phantoms.

Cross-correlation is a standard pattern matching approach to identify structures in the initial image and track them in the successive images. For each pair of images, a two-dimensional window (kernel) of dimension $m \times n$ (*width* × *height*) is defined in the initial OCT image (pre-compressed). This window is centered at every pixel in the successive images (post-compressed) and a 2-D array of cross-correlation coefficients is calculated.

Mathematically, the cross-correlation coefficient at a position (i, j) on the image can be expressed as

$$C(i,j) = \frac{\sum_{jj=1}^{m}\sum_{ii=1}^{n}(\text{kernel}[ii+n][jj+m] - \overline{\text{kernel}})(image[i+ii][j+jj] - \overline{\text{image}})}{\sqrt{\sum_{jj=1}^{m}\sum_{ii=1}^{n}(\text{kernel}[ii+n][jj+m] - \overline{\text{kernel}})^2 (image[i+ii][j+jj] - \overline{\text{image}})^2}} \quad (5.2)$$

Here, $\overline{\text{kernel}}$ and $\overline{\text{image}}$ are the mean values of the pixels under an area of dimensions $m \times n$ in the pre-compressed and post-compressed images respectively. The cross correlation coefficient is maximum for the identical regions and displays minima for the uncorrelated regions. Over the entire image, an array of correlation coefficients is calculated and the point of highest cross-correlation magnitude corresponds to the

displacement of pixel (*i*, *j*) in the post-compressed OCT image in the axial and lateral dimension. The axial and lateral displacements can be combined to form vectors, which in turn, can be graphically represented as displacement vector maps. In the present work, six different kernel sizes (11×11, 21×21, 31×31, 41×41, 51×51 and 61×61) were employed for the gelatin phantoms for comparison and to test the accuracy of the measured displacements. Here the first and second numbers represent the number of pixels in the axial and lateral directions respectively. The optimum kernel size was selected by comparing the mean axial displacement as calculated from the displacement maps for the six kernels and the actual (measured) displacement of the top layer of the phantom under axial compression.

Local strain value *(ε)* at a given pixel (*i*, *j*) in the image has been calculated from the 2-D axial displacement maps as:

$$\varepsilon = \frac{d_{i+1,j} - d_{i,j}}{\Delta z} \tag{5.3}$$

Here, $d_{i,j}$ and $d_{i+1,j}$ are the displacement magnitudes of two successive pixels in the axial direction under the effect of applied load, Δz being the original distance between these two successive pixels.

5.4.3 Validation experiments with gelatin phantoms

Figure 5.5 shows the OCT images of gelatin phantom subjected to axial compressive load. The pre-compressed image is shown in Figure 5.5 (a) while the displaced OCT images have been displayed in Figure 5.5 (b-f). The phantom-cover slip interface is labelled in Figure 5.5 (a). Compressive load corresponding to the successive displacement (~ 20 μm) as observed in the experiments is about 245 N/m^2. However, for better visualization of displacement of the top layer of phantoms, images corresponding to alternate load values

(490 N/m^2) have been shown in the figure. Bright speckle patterns as seen in the images are due to the presence of the distributed activated charcoal particles embedded in the phantom. A gradual shift of these speckle patterns in the axial direction due to the compressive loading can be seen from the displaced images.

Figure 5.6 show the displacement vector maps for the gelatin phantoms for 31×31, 41×41 and 51×51 kernel sizes. The maps correspond to the images shown in Figure 5.5. A comparison of all the six kernel sizes in terms of accuracy in the measurement of the mean axial displacement has been summarized in Table 5.1. The axial displacement map presented in the figure quantifies the trajectories of the speckle patterns of the phantom and gives a measure of the degree of particle displacement subjected to compressive loading. It is to be seen that with the increasing size of the kernel, the displacement vector maps are less noisy and the vectors are more clearly defined. This transition can be attributed to the fact that the large kernel sizes tend to average out the differences in the displacement of small particles in the phantom. However, larger kernel sizes also limit the ability of the technique to assess the microstructural movement of small speckles within the tissue phantoms. For the selection of the best kernel size, the mean axial displacement has been calculated from the displacement maps of successively displaced OCT images and compared with the actual displacement of the top layer of the phantom. The actual displacement has been measured directly from the recorded OCT images by noting the downward shift in the top layer of the phantom before and after the application of the axial compressive load (245 N/m^2). In terms of the percentage error between the calculated and measured displacements, minimum error was observed for 41×41 kernel dimensions (~ 5%) whereas the errors were seen to be considerably higher for 11×11 (~ 45%), 21×21 (~ 30%), 31×31 (~ 10%), 51×51 (~15%) and 61×61 (~25%) kernel sizes (Table 1). Based on

these results, a kernel size of 41×41 pixels was chosen as the optimum for the cross correlation technique and also employed for the analysis of resected breast tissue samples.

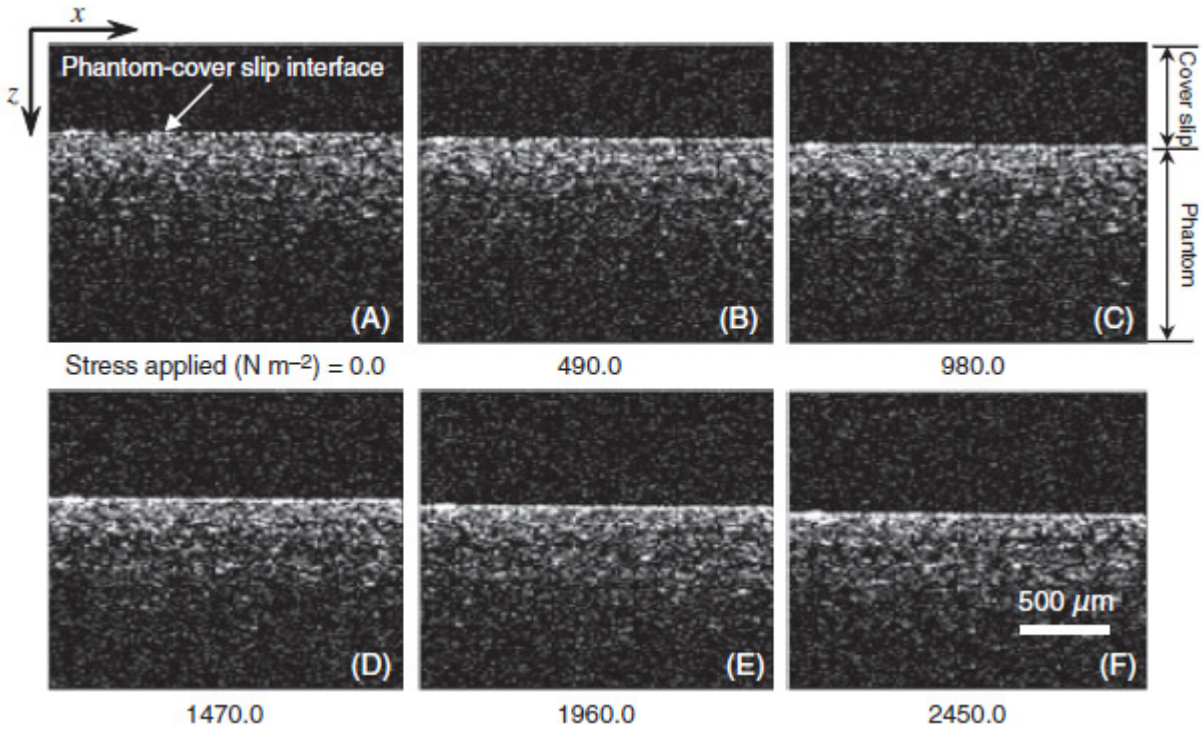

Figure 5.5: Original (a) and post-compressed (b-f) OCT images of gelatin phantoms. Axial load (in steps of ~ 245 N/m^2) is applied along z-direction to compress the phantoms. For better clarity, OCT images corresponding to alternate load values have been shown above. The displacement of the top layer of the phantom (phantom-cover slip interface) in successive images shown above is about 40 µm.

Table 5.1: Percentage error between calculated mean axial displacement and measured axial displacement for six different kernel sizes.

Kernel size (Pixels)	Calculated mean axial displacement (µm)	Measured axial displacement (µm)	Percentage error
11×11	11	20	45
21×21	14	20	30
31×31	18	20	10
41×41	21	20	5
51×51	23	20	15
61×61	25	20	25

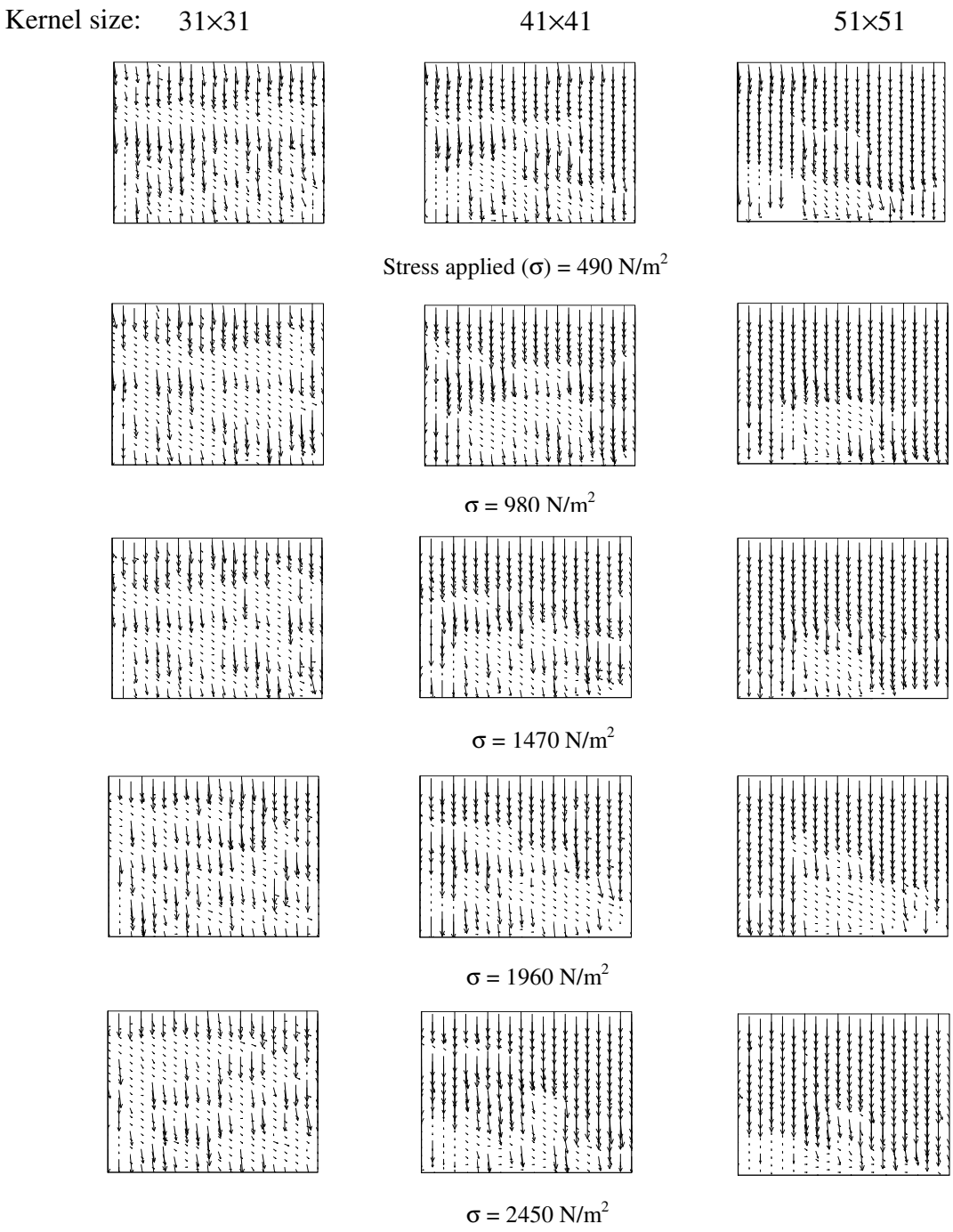

Figure 5.6: Displacement vector maps for a series of axial compressive loads as obtained for gelatin phantoms by cross correlation technique with three different kernel sizes (31×31, 41×41 and 51×51 pixels). The maps correspond to the OCT images shown in Figure 5.5. (Vertical dimension of each plot (from top to bottom): 1.38, 1.34, 1.30, 1.26 and 1.22 mm. Horizontal dimension: 2.0 mm. Numbers below each row indicate the compressive stress applied in N/m^2.)

5.4.4 Measurements on breast tissue samples

OCT images of the normal, benign and malignant breast tissue samples were acquired with tissues subjected to compressive loading in the axial direction. The cross correlation technique was used to determine the axial displacement and strain for the breast tissue samples. The elastic properties of normal, benign and malignant tissue samples were calculated using the stress-strain relationship and have been reported in terms of the modulus of elasticity. The present analysis is valid under the assumption that the tissue is incompressible [100,101]. This implies that the Poisson ratio for breast tissue samples is approximately 0.5, and hence, only an elastic modulus is required to characterize the tissue.

Figure 5.7 shows the OCT images of normal, benign and malignant resected breast tissues samples. The pre-compressed images have been shown in Figure 5.7(a) and the successively displaced images due to compressive loading are presented in Figure 5.7(b). The spatially periodic highly scattering boundaries, as seen in the normal breast tissue OCT images (column 1), are primarily due to the presence of large lipid-filled adipocytes cells. Columns 2 and 3 in Figure 5.7 show the OCT images of benign and malignant breast tissues respectively. These images show relatively dense scattering compared to the OCT images of normal samples. The scattering differences between malignant and the benign tissues are not very significant hence these two pathological variations cannot be distinguished based on the qualitative assessment of OCT images alone.

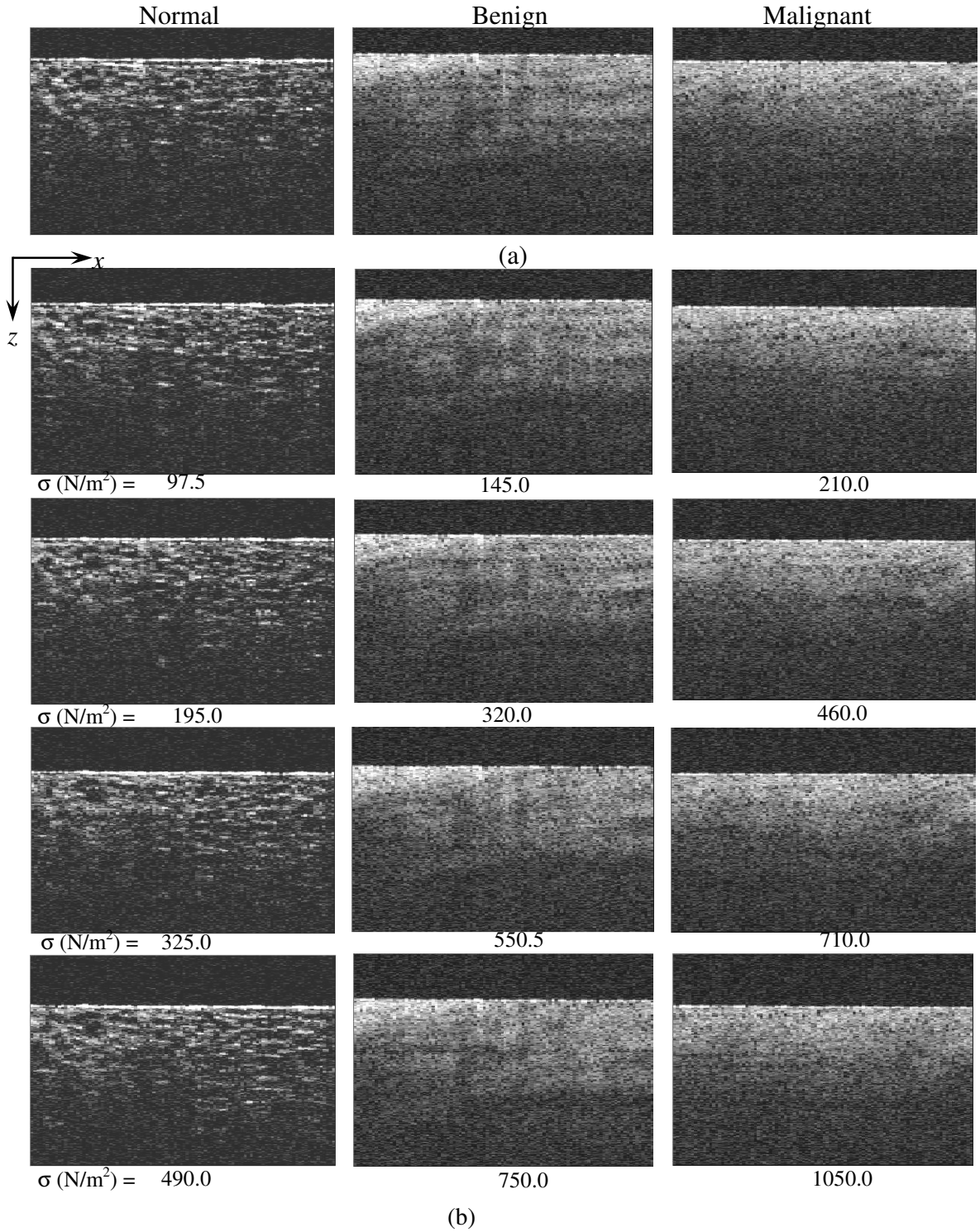

Figure 5.7: Original (a) and post-compressed (b) OCT images of normal, benign and malignant breast tissue samples. The compressive stress is applied along z-direction (axial). Displacement in successive images shown above is about 40 μm.

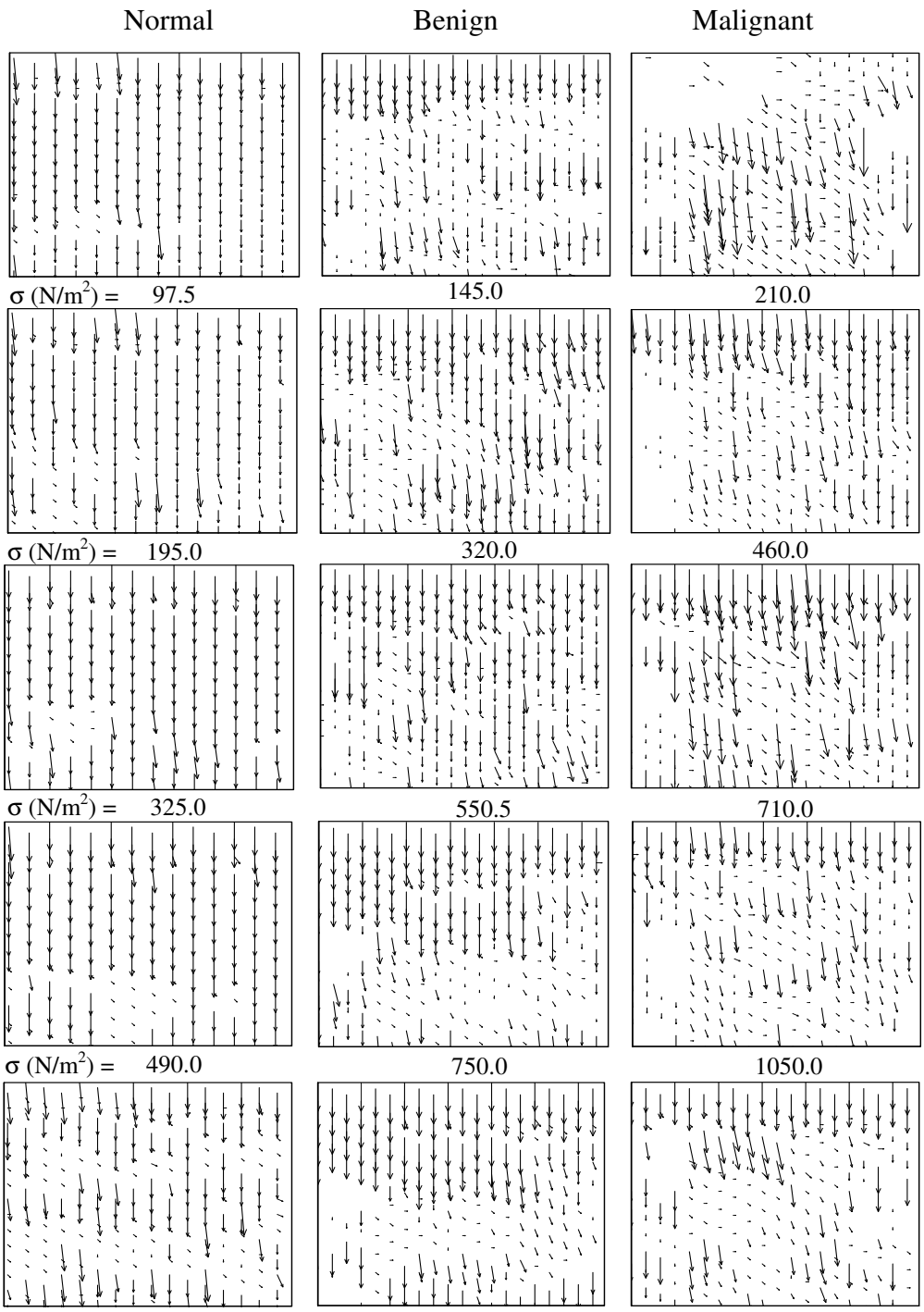

Figure 5.8: Displacement vector maps for a series of axial compressive loads as obtained for normal, benign and malignant breast tissue samples by cross correlation technique. (Kernel size= 41×41 pixels). (Vertical dimension of each plot (from top to bottom): 1.66, 1.63, 1.59, 1.54 and 1.50 mm. Horizontal dimension: 2.0 mm). The number below each image indicates the compressive stress applied in units of N/m^2.)

Figure 5.8 shows the axial displacement vector maps for normal, benign and malignant breast tissue samples. The displacement vector maps for the normal class show a well-defined movement of the speckle patterns in the axial direction. On the other hand, the displacement vectors are not so uniformly distributed for benign, and especially for the malignant samples. For these samples, the vector maps qualitatively highlight the presence of regions where net displacement is either very small or negligible. A comparatively larger variation is also to be seen in the magnitude of axial displacements within a given vector plot for malignant samples. These differences in the distribution of axial displacements of the speckle patterns between the three classes of tissue samples could be attributed to the differences in the elastic properties of the samples as well as to the degree of heterogeneity within a given tissue sample (that was large for the malignant samples considered in the present work).

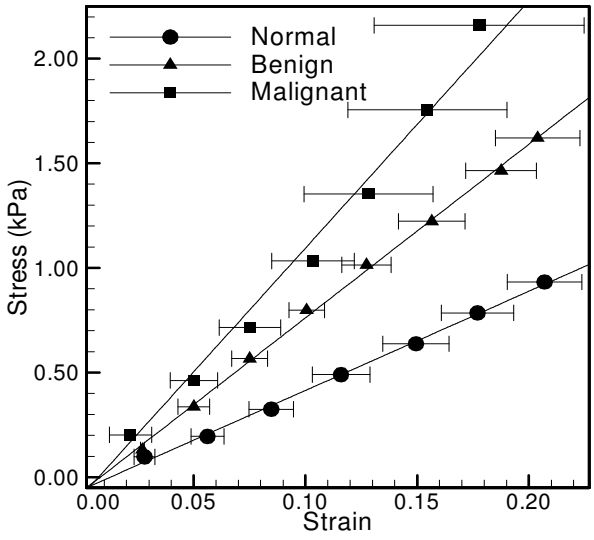

Figure 5.9: Stress-strain curves for normal, benign and malignant breast tissue samples.

Quantitative assessment about the relative differences between the elastic properties of normal, benign and malignant breast tissue samples can be made by

estimating the modulus of elasticity for these samples. In the present work, the Young's modulus for each class of breast tissue samples has been estimated by measuring the slope of the respective stress-strain curves. Figure 5.9 shows the stress-strain curves for normal, benign (*fibroadenoma*) and malignant (*invasive ductal carcinoma*) breast tissue samples subjected to compressive loading. The stiffness coefficients (Young's modulus) for each class of tissue samples were estimated by calculating the slope of the respective stress-strain curve using a linear fit. The analysis was performed on 12 samples and the means and standard deviations for each category have been presented. It is to be stated here that for each compressive load, an average of local strain values over all the pixels has been calculated and this value is used for plotting the stress-strain curve for each of the three classes. In quantitative terms, it can be seen that the curve for malignant breast tissue sample is the steepest (slope, a measure of elastic modulus: 16.45 kPa (mean) ± 1.103 (standard deviation)) revealing highest stiffness coefficient among the three classes whereas the curve for benign sample (slope: 9.03 ± 0.215 kPa) falls between the normal (slope: 4.17 ± 0.074 kPa) and malignant. It is to be noted that the values of the standard deviation are relatively low in all the cases, which confirms the repeatability of the experiments and the data reduction approach. These values are also summarized in Table 5.2. The numerical values of Young's modulus for malignant breast tissue samples are approximately four times higher than the normal tissues whereas for benign tissue samples, it is about 2 times higher than the normal samples. These results are qualitatively consistent with the previous reports on elastic properties of breast tissue by Krouskop [100], Manduca *et al*. [102], Lorenzen *et al*. [103] and Samani *et al.* [104].

Table 5.2: Means and standard deviations of the estimated modulus of elasticity for the three classes of breast tissue samples identified as normal, benign (fibroadenoma), and malignant (invasive ductal carcinoma).

	Normal	Benign (Fibroadenoma)	Malignant (Invasive ductal carcinoma)
Elastic modulus (kPa)	4.17 ± 0.074	9.03 ± 0.215	16.45 ± 1.103

5.5 Imaging tumor spheroids using OCT

Multicellular tumour spheroids are three-dimensional cell cultures that resemble avascular solid tumours [105]. Studies have shown that these spheroids exhibit structural, metabolic, functional and growth pattern similarities to solid tumours [106,107]. Tumour spheroids are therefore a good model systems for studying therapeutic effects of radiation.

For effective testing of drugs being explored for treatment of solid tumours, rapid methods of generation and analysis of spheroids are crucial. For studying the response of tumour spheroids to drugs, the most widely used method is to measure their size and volume by microscopy. However, volume estimation by this method may not be accurate because spheroids formed by different techniques may not be perfect spheres. Histology is also used for studying the response of tumour spheroids to different treatments. This however, is not only laborious and time consuming but is also destructive. Non-invasive techniques that could periodically monitor the size and the shape of spheroids are required for speeding up the process. In the direction, Yu *et al.* have used holographic optical imaging technique for imaging rat osteogenic sarcoma tumour spheroids [108]. We have

used OCT setup for studying the dynamics of tumour spheroid formation, as it can provide high resolution cross-sectional images non-invasively.

Tumor spheroids generated by modified hanging drop method were used for imaging growth dynamics [109]. Single cell suspension (Human colon adenocarcinoma, colo-205 cells) was prepared by trypsinizing cells grown in monolayers with 0.25% trypsin (w/v) (Himedia). Cell count in the suspension was determined using Hemocytometer and the suspension was diluted in growth medium to have ~ 1.75×10^6 cells ml-1. For generating cellular aggregates, 20µl of the cell suspension having ~35,000 cells was placed as drops on the lids of 60 mm Petri dishes (Tarson, India). The lids with drops were inverted over the dishes containing 2 ml of growth medium and then incubated at 37^0 C in 5% (v/v) CO_2 incubator. After 24 h of sedimentation, the cellular aggregates were picked up using a pipette. These were transferred to agar coated Petri dishes containing 5 ml of growth medium and allowed to form spheroids. For growing spheroids by the liquid overlay technique, 1×10^6 cells were plated on the agar coated Petri dishes containing 5ml of growth medium. Clusters of cells could be observed within three to four days of incubation. These were allowed to grow for 7 to 14 days.

The growth dynamics of tumour spheroid formation were imaged using conventional microscopy and OCT imaging setup. In Figure 5.10 (A) we show the OCT images of the spheroids grown for different durations. In all the images, scattering from the agar base is clearly visible. The initially cellular aggregates appear flat with slight curvature towards the edge. With increase in the age of the spheroids, the thickness of the cell layers in the axial direction was observed to increase whereas lateral diameter decreased. In contrast to OCT images, the cellular aggregates and the growing spheroids appeared spherical under microscope (Figure 5.10 B (a-e)). The diameter of each spheroid was estimated by

measuring the geometric mean of the two orthogonal diameters using a calibrated eyepiece reticule (Figure 5.11). The images were taken with a camera mounted on the top of the inverted microscope. Volume of the spheroid images with microscope (50X) was calculated using the formula $V=4/3\pi r^3$ for a sphere where 'r' is the radius. The spheroids appeared translucent up to 3 days. Beyond this time point, two distinct regions could be seen in the microscopic images. The central region was dark compared to the outer region. In six-days old spheroids, the area of the dark center increased and diffuse light could be seen only from rim of the spheroids (Figure 5.10B (d)). The observed decrease in the light transmitted through spheroid is due to an increase in thickness. However, actual thickness could not be estimated by microscopic method.

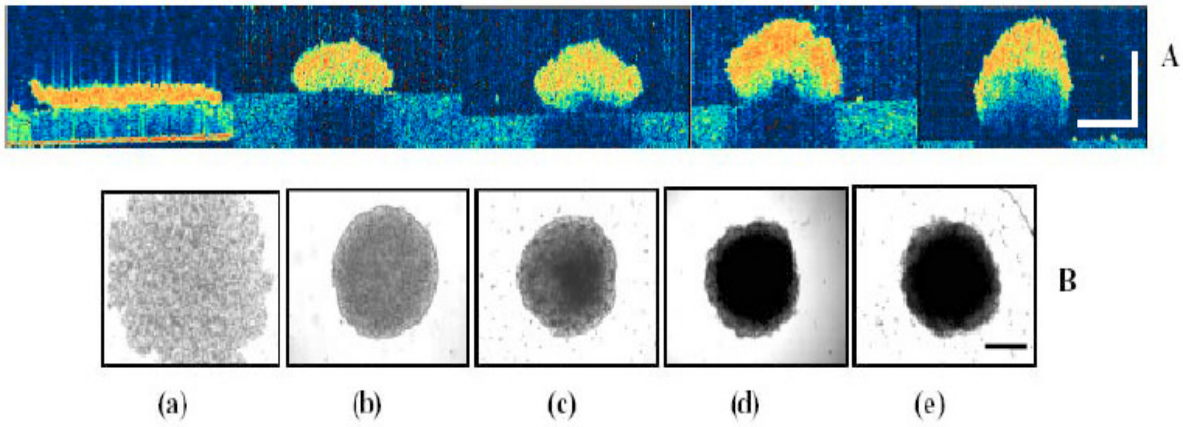

Figure 5.10: Images of spheroids grown for different durations (a) 0, (b) 4, (c) 5, (d) 6 and (e) 7 days; A) OCT and B) Phase contrast images. Zero day represents time when cell aggregate is transferred from hanging drop to agar coated petridishes. Scale bar: 500 µm

The measurements made by OCT on the axial thickness of spheroids with growth are shown in Figure 5.11. Since OCT images revealed that the tumour spheroids were not spherical, volume was calculated using the formula for oblate spheroid, $V=4/3\pi a^2 b$, where 'a' and 'b' are the radius for the long and short axis respectively. The OCT images provide

the optical depth (physical depth multiplied by refractive index of the medium) hence the physical depth of the spheroid was determined by taking its refractive index to be 1.36 same as for the tissue [110]. Although axial thickness was seen to increase with growth, lateral diameter of spheroids measured by both microscopic and OCT methods reduced with increase in age and were found to be almost constant after 4 days (Figure 5.11). The reduction in lateral diameter may arise because, the non-adherent agar base prevents the cell attachment to surface and therefore even if cell growth expands laterally, layer of cells fold onto itself and grow only in the axial direction [109]. Another reason for the observed decrease in lateral thickness of spheroids may be the increase in cohesiveness of cells in the spheroids. This arises because of an enhanced expression of cadherins and integrin proteins in cells comprising spheroids [111].

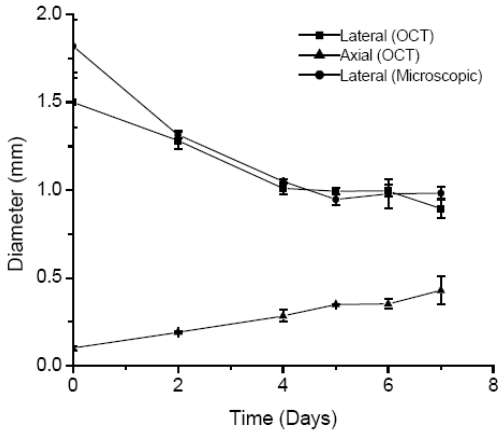

Figure 5.11: Comparison of dimensions of spheroids measured by microscopy and OCT.

Volumes of the spheroid determined by OCT increased with increase in growth and correlated with increase in cell number (Figure 5.12 a). Total number of cells in the spheroids at different time points was evaluated by microscopic counting using hemocytometer (Figure 5.12b). It is interesting to note that for the spheroids prepared by

the method followed by us, although the cell number increased with time, volume determined by microscopy decreased with growth (Figure 5.12a and b). This may be because in this method, a large numbers of cells are used for the hanging drop preparation. This result in formation of large two dimensional cell aggregates and acquires three-dimensional structure on transfer to non-adherent agar by growing only in the axial direction. Since microscopic measurements cannot evaluate the depth accurately, the lateral diameter used for calculation may wrongly estimate a decrease in volume with increase in time of growth. It is also pertinent to note that although the volume measured by OCT method was slightly lower than the microscopic method the difference in the two measurements decreased with an increase in the age of the spheroid. This may be due to a lower axial thickness of the spheroid as compared to its lateral diameter.

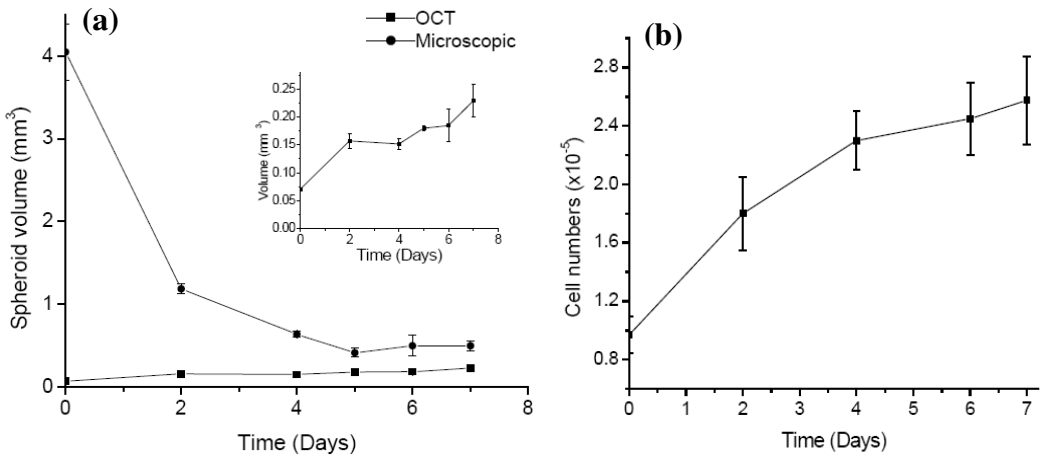

Figure 5.12: (a) Volume of spheroids determined by microscopy and OCT. Inset shows volume of spheroids determined by OCT in expanded scale. (b) Total number of cells in spheroids grown for different days. Cell count was determined using Hemocytometer.

Spheroids generated by the liquid overlay and spinner culture method develop necrotic centers due to the low levels of oxygen and nutrients. With an increase in the age

of spheroids the size of necrotic centers increases [112]. To evaluate the possibility of the use of OCT for studying the morphological changes, we imaged 10 days old spheroids (~200 µm, diameter) prepared by liquid overlay method (Figure 5.13). For identifying the necrotic regions in spheroids, these were stained with 10 µg/ml of propidium iodide (Molecular Probes Inc) for 15 min. These were then examined under a fluorescence microscope (Axiovert 135, Zeiss) using 540 nm band pass excitation and 590 nm long pass emission filters to detect fluorescence from propidium iodide. Spheroids, which showed fluorescence were used for imaging by OCT. The OCT images showed distinct high intensity scattering in some regions. Since these spheroids also showed propidium iodide fluorescence, the high scattering regions can be considered to be necrotic.

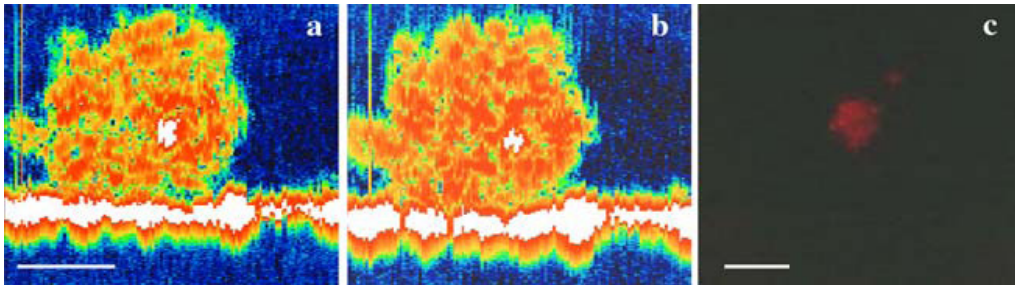

Figure 5.13: OCT cross sectional images of the spheroid grown by liquid over-lay method (a-b), a & b are OCT images of same spheroid acquired twice to show the reproducibility of high scattering regions, fluorescence image of a typical spheroid grown for 10 days time stained with propidium iodide. Scale bar: 50 µm (c). Spheroids were stained with propidium iodide (10 $\mu g ml^{-1}$) for 15 min. The fluorescence was viewed under microscope using 540 nm band pass excitation and 590 nm long pass emission filters respectively. Scale bar: 40 µm.

5.6 Summary

We have carried out OCT and PS-OCT imaging of resected human breast tissue samples belonging to different pathologies. The measured values of birefringence show that the benign (fibroadenoma) breast tissue samples have significantly higher birefringence than

that in malignant (invasive ductal carcinoma) tissue samples. Similarly, the stiffness coefficients of these tissue samples were quantified in terms of the elastic modulus estimated using the measured displacement vector and axial strain. The results of the experiments performed on resected breast tissue samples reveal that the stiffness coefficient for benign samples, as calculated from the stress-strain relationship, is found to be about 2 times higher than the normal samples, whereas for malignant samples, it is approximately 4 times. These results indicate that PSOCT imaging and OCT based elastography can be used as the potential tool for effective discrimination of breast tissue samples.

We have also used OCT to monitor the growth dynamics of tumour spheroid formation. Volume of spheroids estimated by OCT correlated well with the increase in cell number as a function of the growth. OCT images also revealed heterogeneous structures in the 200 µm spheroids that correlated with necrotic regions observed by the fluorescence of propidium iodide. The use of OCT imaging for monitoring the growth of spheroids may prove to be useful for evaluating the drug response on tumour spheroids. Compared to histology, this technique provides a non-invasive and rapid method for evaluating tissue changes.

CHAPTER 6: NON-INVASIVE MONITORING OF WOUND HEALING USING OCT

Abstract: In this chapter we first describe the use of PSOCT imaging of tissues resected from Staphylococcus aureus infected and uninfected wounds, at different healing times, to assess the morphological changes and collagen remodeling at various stages of wound healing. Next we describe the use of a time domain real time (~ 8 frames/s) OCT set up for monitoring the healing of wounds non-invasively without sacrificing the animal. These measurements showed that compared to the uninfected wounds, the infected wounds had prominent edematic regions which leads to a significant delay in re-epithelization and collagen remodeling phases of wound healing. The OCT measurements were found to be consistent with the corresponding histological measurements demonstrating the potential of OCT for non-invasive monitoring of the progression of wound healing.

6.1 Introduction

Cutaneous wounds e.g., burns, chronic skin ulcers and surgical wounds are among the most common wounds in clinical medicine [113,114]. Wound healing is a complex and dynamic process that can be roughly divided into three phases – inflammation, proliferation and tissue remodeling. In the normal wound-healing process, after the inflammatory phase, re-epithelialization, thickening of the newly formed epidermis and remodeling of collagen fibers occur in a timely fashion [115]. However, in a chronic wound, these healing processes are disrupted at one or more points, resulting in a delay in

healing beyond the anticipated time. Bacterial infection is one of the main predisposing factors for the development of chronic wounds [116] and infected wounds could severely compromise the overall health of an individual, and may cause increased trauma and higher treatment costs [117]. Staphylococcus aureus is one of the most common human pathogens responsible for a variety of cutaneous and systemic infections including postoperative or injury wound infections [118] resulting in impairment of wound healing [119]. Clinical manifestations in infected wounds mainly arise due to the host response to the toxins secreted by bacteria [120].

In clinical practice, wound size, colour, odour, and drainage are used for gross evaluation of wound healing. These methods, however, do not provide structural information below the wound surface and can be very subjective [121]. Histology is the standard method for obtaining the structural details of the wound tissues [122] however biopsy is disruptive, may contaminate the wound, and also introduces a new wound, thereby prohibiting repeated assessment of the healing process in the same wound [123]. Other methods include measurements of the tensile strength and electrical impedance of the wound. Because of invasiveness, these methods are also not common in clinical practice [124]. To facilitate a timely decision for correct therapy, it is important to accurately monitor the morphological changes in the infected wounds using non-invasive tools. Several noninvasive methods have been investigated, which include high-resolution ultrasound, thermography, laser Doppler imaging, polarization imaging, fluorescence imaging [125], confocal microscopy, [126] and magnetic resonance imaging [127]. Although ultrasound imaging is used to examine wound healing, the depth resolution achievable (~75 μm) is insufficient to monitor fine structural changes like reepithelialization. Additionally, ultrasound requires matching media in direct contact with the wound surface, which may cause mechanical damage to wound tissue [126]. The morphological changes of wounds

can also be measured using OCT or using PSOCT which can also monitor changes in the ordering of collagen matrix. These structural and birefringence changes can be used to characterize the different phases of the wound healing and could provide a basis for non-invasive wound healing assessment.

The use of PS-OCT for quantitative evaluation of collagen denaturation induced by a thermal injury, for visualization of collagen fiber regeneration and for quantification of various drug effects during wound healing has been demonstrated [128]. While these previously mentioned studies have demonstrated the utility of PS-OCT for monitoring the normal wound healing process, the use of this technique for evaluating the morphological changes associated with bacteria infected wounds has not been investigated. Further, it has been demonstrated that bacterial toxins have a detrimental effect on wound tensile strength and have been found to decrease collagen deposition and cross-linking [129] that may show up as birefringence changes in PS-OCT imaging. We have therefore used PSOCT and real-time OCT imaging setups to characterize the different phases of healing of uninfected and S. aureus-infected superficial skin wounds under *ex-vivo* and *in-vivo* conditions respectively. The PSOCT setup was used to investigated the changes in collagen birefringence in the uninfected and S. aureus infected wounds while the realtime OCT imaging on samples were performed for studying the kinetics of healing of infected wounds under *in-vivo* conditions.

6.2 Staphylococcus aureus bacterial culture

S. aureus MTCC No. 740 (equivalent to ATCC 9144) was obtained from the Institute of Microbial Technology, Chandigarh, India. Bacteria used for infection were grown overnight in Tryptic Soya broth (TSB, Himedia, Mumbai, India) under aerobic conditions at 37º C using a shaker incubator.

6.3 Wound creation and bacterial infection

Animal infection experiments were performed in accordance with institutional and national guidelines on animal care. Six- to 8-weeks-old female Swiss albino mice were used for all experiments. The mice were anesthetized by an intraperitoneal injection of Ketamine (80 mg/kg) and Xylazine (10 mg/kg). The tape-stripping wound model was generated according to the procedure described by Kugellberg et al. [130]. For tape stripping wounds, hair was removed from an area of ~ 2 cm^2 from the back of the mice using a depilatory cream after anesthetizing the animals. The skin was then cleansed with Betadine. For wound generation, the skin was stripped 12–15 times with Tensoplast (Johnson & Johnson, Mumbai, India). Following this procedure, the skin became visibly damaged and appeared red and glistening but no bleeding was observed. Microscopically, this procedure resulted in the partial removal of the epidermal layer. Infection was initiated by placing a 50 mL of stationary-phase culture of S. aureus suspension containing ~5×10^8 cells on the tape-stripped skin. To confirm the establishment of wound infection, mice were euthanized at different time points and ~ 2 cm^2 wounds were excised. Wound tissue was divided into two parts. One part was used for determining bacterial counts by colony-forming units (CFU) and the other part was used for PSOCT and histological studies. The number of CFU in the wounds was assessed at different post-infection time points.

For CFU determination, the tissue was homogenized in 2 ml of phosphate-buffered saline (PBS) using a hand homogenizer. Homogenized samples were diluted in PBS and an appropriate volume of the diluted sample was plated on TSB agar plates to determine the CFU. The bacterial counts obtained were normalized with respect to the weight of the infected wound tissue. About 10^8CFU/gm were recovered from the wound at 24 h

following the application of S. aureus (Figure 6.1). The number of CFU decreased by 1.5 log at 48 h. The bacterial count recorded (~ 10^6 CFU/gm) at this time point indicated the successful colonization of bacteria in the wound [117]. Beyond 96 h, the bacterial counts were negligible.

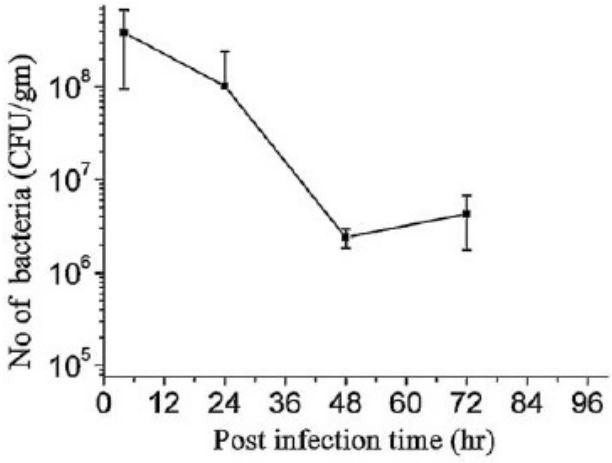

Figure 6.1: Post-infection time-dependent bacterial counts obtained from wounded skin tissue of mice. The error bar represents the standard deviation around the mean calculated from three different experiments. Data represented at each infection time point are obtained from three mice.

6.4 *Ex-vivo* imaging of healing of wounds using PSOCT and Histology

The PSOCT setup used for the *ex-vivo* imaging is described in chapter 2 of the thesis. Briefly, it measures the polarization components of the back scattered light from sample and calculates the intensity or reflectivity images and the birefringence images of tissue samples. For imaging, resected wounded skin was marked with an ink pen at regions of interest and placed on a linear translation stage.

In order to characterize the histopathology of the wound model, wounded skin close to the OCT imaged regions was excised on days 2, 4 and 10 of tape stripping and fixed in formalin (4%). The formalin-fixed biopsy specimens were processed using a standard histological procedure and stained with hematoxylin and eosin. The slides were examined under a microscope to determine tissue changes such as inflammation and reepithelization.

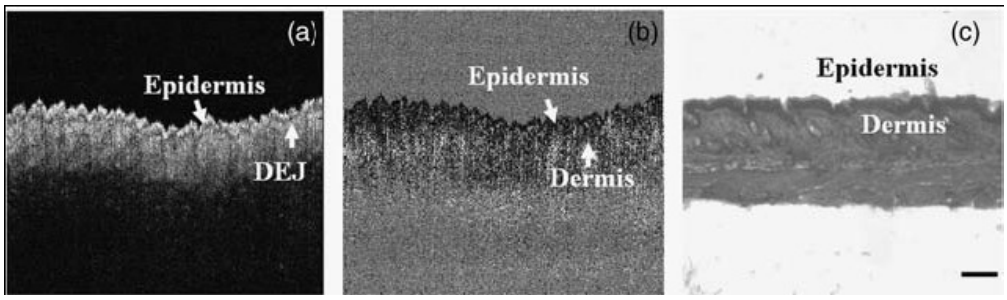

Figure 6.2: PSOCT image of the normal mice skin. Back scattered (a; image size: 1.5 mm × 3 mm), optical retardation (b; image size: 1.5 mm × 3 mm) OCT images of resected mice skin and the histology image (c) of the corresponding tissue. Scale bar: 200 µm.

Figure 6.2 (a) shows the backscattered intensity OCT images of normal mice skin. The upper layers in the skin correspond to the epidermis, which is approximately 50 ± 12 µm. The relatively higher scattering region of ~ 250 ± 12 µm below the epidermis corresponds to the dermis. The corresponding cumulative optical retardation (i.e. phase difference induced in the two orthogonally polarized light beams in the given thickness of the tissue) is shown in Figure 6.2 b. The transition from black to white bands in the PSOCT image of the dermal region represents the change in the accumulated phase retardation from 0 to $\pi/2$. This can be attributed to higher collagen density or organized collagen [128]. Figure 6.2 c shows the histology of the skin section imaged with OCT. The thicknesses of the epidermis and the dermis measured in this image are 30 ± 12 µm and

150 ± 15 µm, respectively. These values are lower (~ 1.5 times) than the values measured from the OCT images. This is attributed to the shrinkage of the tissue caused by histological processing [131].

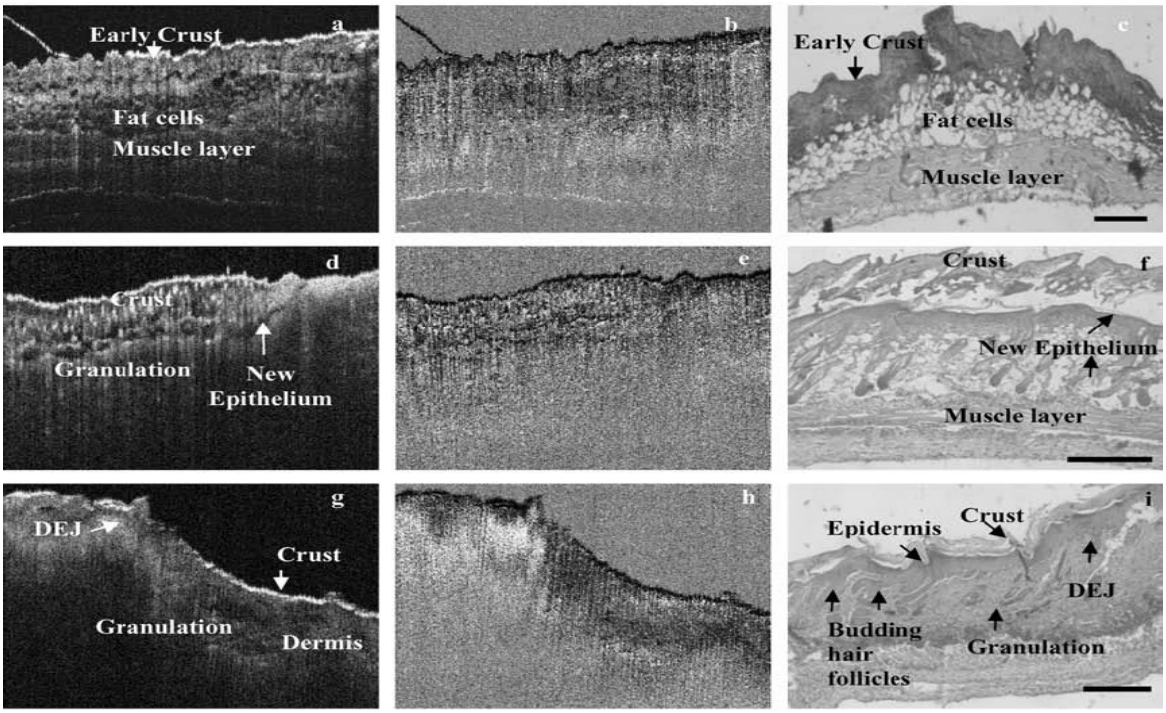

Figure 6.3: Time-dependent structural changes in uninfected wound skin of mice. Left (a, d, g), middle (b, e, h) and right (c, f, i) panels represent backscattered intensity OCT images, PSOCT images and histological images, respectively. Top (a–c), middle (d–f) and lowermost (g–i) rows represent images of resected wounded skin sample imaged on days 2, 4 and 10 of wounding, respectively. OCT images; image size: 1.5 mm × 3 mm. Histology images; scale bar: 100 µm.

Figure 6.3 shows the representative backscattered intensity (a, d, g), birefringence (b, e, h) and the corresponding histological images of uninfected wounded skin on days, 2, 4 and 10. On day 2, a bright scattering discontinuous layer appeared at the top that corresponded with the early crust (Figure 6.3; a–c). The back-scattered intensity in the epidermis and dermis region of the wound tissue (Figure 6.3; a) was lower and more nonuniform than that of normal skin, which indicated loosening of the tissue matrix due to

tissue inflammation [132]. In addition, several signal-free regions were also observed in these images (arrows), which may be due to the development of edema. These scattering changes were comparable with the histological images (Figure 6.3; c). Further, in contrast to normal tissue, scattering changes corresponding to adipocytes and the muscle layers below the dermis were clearly observed. This indicated an increase in imaging depth. In the corresponding PS-OCT image, accumulated phase retardation decreased with respect to that of the normal skin, indicating randomization in collagen (Figure 6.3; b). On day 4, the backscattered intensity of the top layer appeared brighter and continuous as compared with day 2, indicating the presence of a continuous crust layer (Figure 6.3; d). Inflammation at this time point was much lower as compared with that of day 2. In addition, a new scattering layer appeared below the edematic regions of the dermis corresponding to a new epithelial layer formation as observed in the histology image (Figure 6.3; f). The appearance of a high scattering layer below the newly formed epithelial layer suggested the formation of granulation tissue [132]. The PS-OCT image at this time point showed an increase in retardation with respect to that of day 2, indicating an increase in tissue compactness (Figure 6.3; e, f). With an increase in the post wounding time (day 10), the intensity of back-scattered light increased. In the OCT images, the granulation tissue appeared more uniform compared with that of the earlier time points, and the dermis epidermis junction (DEJ) was clearly visible (Figure 6.3; g). A relatively higher retardation observed on day 10 (Figure 6.3; h) indicated the recovery of collagen morphology. The histology image showed an almost reconstituted dermis and some budding hair follicles (Figure 6.3; i).

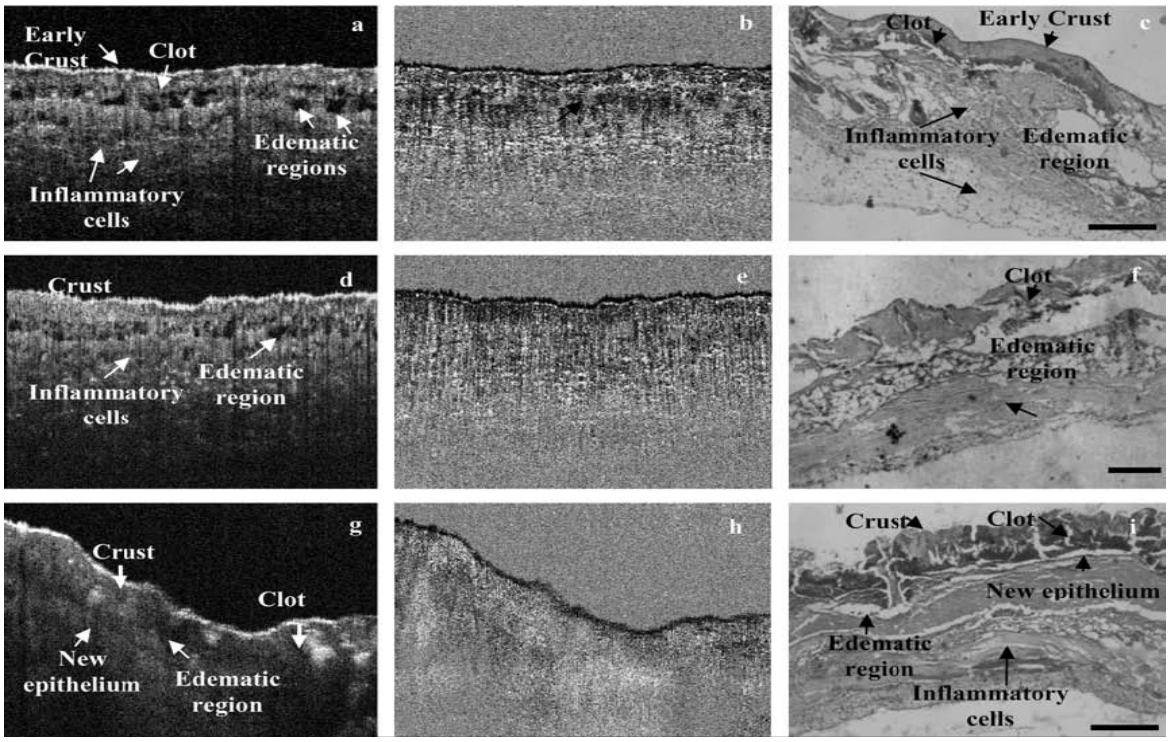

Figure 6.4: Postinfection time-dependent structural changes in infected wound skin of mice. Left (a, d, g), middle (b, e, h) and right (c, f, i) panels represent backscattered intensity OCT images, PS-OCT images and histological images, respectively. Top (a–c), middle (d–f) and lowermost (g–i) rows represent images of resected infected skin sample imaged on days 2, 4 and 10 of wounding, respectively. Image size: 1.5 mm × 3 mm.

Figure 6.4a shows the backscattered images of an infected wound on day 2. Compared with the uninfected wound, the back-scattered intensity from the dermis regions of infected wound tissue was significantly lower. Inflammatory, edematic regions in the dermis below the crust were clearly observed in these images (Figure 6.4 a, b). These observations were comparable with the histology images (Figure 6.4 c). On day 4 (Figure 6.4 d), the severity of edema and inflammation did not show a significant change compared with that of day 2. However, in comparison with the uninfected counterpart, the severity was higher. Further, unlike in the uninfected wound, reepithelialization and granulation tissue were not observed at this time point. Compared with the uninfected

wound, nonuniform scattering and many signal-free regions (Figure 6.4 g) were still evident on day 10 in the infected wound skin, and phase retardation images also showed a disordered collagen morphology. However, the new epithelium started to appear at this time point. These morphological features were comparable with the histology features (Figure 6.4 i) that showed the presence of an incompletely reconstituted dermis.

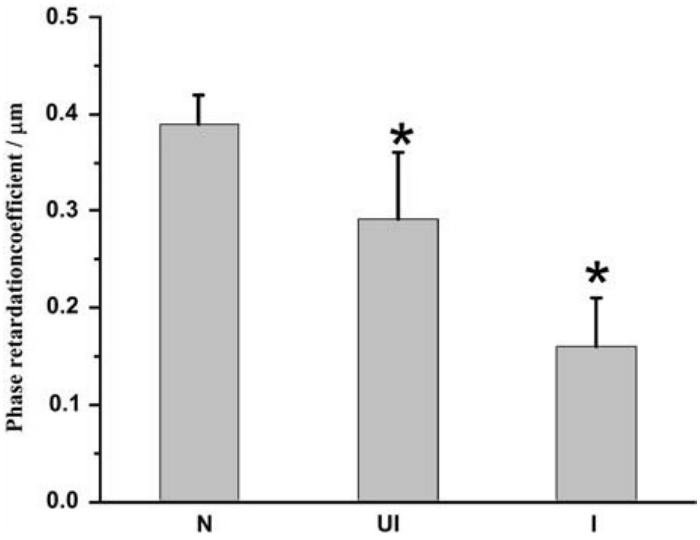

Figure 6.5: Measured mean phase retardation of normal (N), wound skin without (UI) and with infection (I) measures along the skin depth on day 10 of wound creation. Individual columns represent the mean value per sample measured from six different images taken from two different experiments. The scale bars represent standard deviation around mean. The statistical significance was determined using oneway ANOVA (*Po 0.05).

In Figure 6.5, a comparison of the phase retardation values of normal, uninfected and infected wounds on day 10 is shown. A significant reduction in phase retardation was observed in both infected and uninfected wounds, with infected wounds showing a lower value (~45%). Student's t-test was used to determine the significance of the difference between two means. One-way ANOVA was used to compare the significance of the

difference in the phase retardation values of different groups. The level of significance was set at Po 0.05.

6.5 *In-vivo* monitoring of wound healing

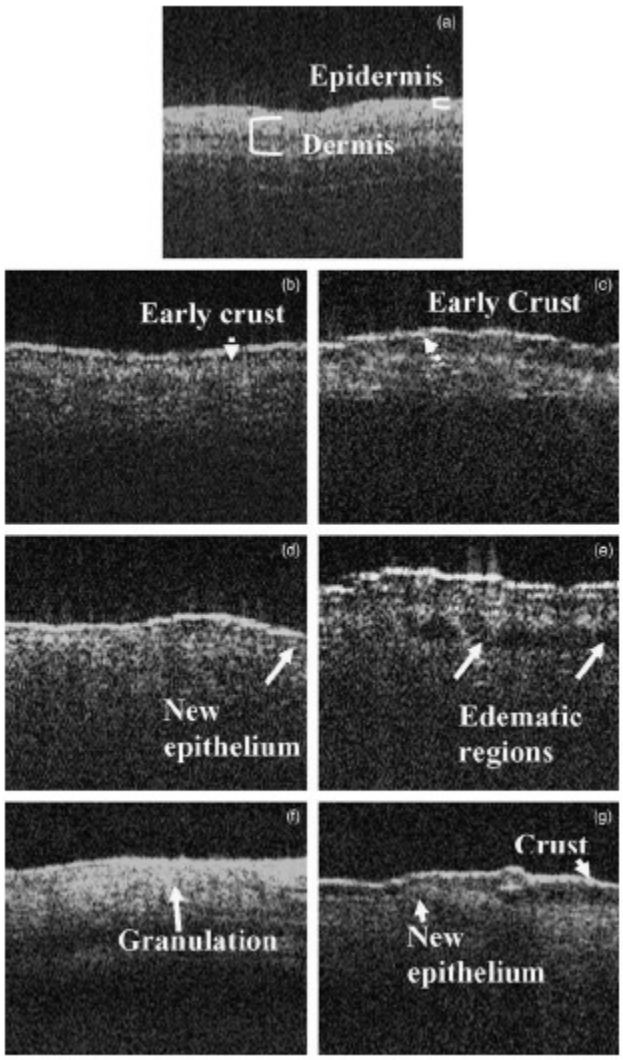

Figure 6.6: Kinetics of healing of uninfected and infected wound imaged using real-time OCT. Top panel (a): image of normal skin. Image size: 1.5 mm × 3 mm. The images show, compared with uninfected infected wounds, a delay in different phases of wound healing.

Wound-healing in infected and uninfected mice under *in-vivo* conditions were also investigated using a real-time OCT imaging setup, the details of which are presented in

chapter 3. In each group (uninfected and infected), a single mouse was used for monitoring the morphological changes during wound healing. Before OCT imaging, the mice were anesthetized and placed on the XY stage. Figure 6.6 shows the back-scattered intensity (*in-vivo*) images of uninfected (left panel) and infected mice (right panel) skin on days 2 (b, c), 4 (d, e) and 10 (f, g). The discontinuous scattering observed from the new epithelium of uninfected mice on day 4 becomes uniform on the 10^{th} day. The back-scattered intensity images of normal skin, uninfected and infected wounds monitored using real-time OCT were comparable to that of resected normal and wounded skin imaged using the PSOCT set up.

6.6 Discussion

In this study, PS-OCT and real-time OCT imaging were used to characterize the different phases of healing of uninfected and S. aureus-infected superficial skin wounds under *ex-vivo* and *in-vivo* conditions. The changes observed in the OCT images of wounded skin on day 2, such as an increase in imaging depth compared with normal skin and the presence of signal-free regions (Figure 6.3; a–c) corresponding to edema, indicate an early inflammatory response of the wound tissue. The inflammatory phase is the first step in the wound-healing process comprising both a vascular and a cellular response [133]. The vascular response involves local vasodilatation, blood and fluid extravasations into the extra vascular space, and blockage of lymphatic drainage leading to the development of edema. The cellular response of inflammation, which normally starts within 24–48 h of wound, is characterized by infiltration of neutrophils and other immune cells. In the OCT images, the non-uniform dermal back scattering (Figure 6.3; a) observed on day 2 is an indication of the presence of inflammatory cells [132]. The migration of immune cells is

accompanied by the production of matrix-degrading hydrolytic enzymes, which initiate the degradation of the provisional matrix [134]. This may have contributed to the low and random birefringence observed on day 2 (Figure 6.3; b). The crust layer was also visible in the OCT images at this time point. These observations are in agreement with the wound-healing-associated morphological changes in mice reported using ultra-high-resolution OCT [128]. In the OCT images, the presence of a noticeable bright scattering layer below the crust layer of wound on day 4 (Figure 6.3; d) indicated the formation of a new epithelial layer [135]. This corresponded with the proliferative phase of wound healing. During this phase, the epidermis is restored following a cutaneous injury. In addition, below the new epithelial layer, a relatively uniform high scattering layer was observed. This indicated the onset of granulation on the fourth day after wound creation in uninfected wounds (Figure 6.3, d) during which new collagen is synthesized [115]. On day 4, the increase in birefringence, tissue compactness and decrease in imaging depth (Figure 6.3, d) also correlated with the formation of granulation tissue. More intense backscattering and ordered birefringence observed on day 10 in the wounded tissue than on previous days suggests restoration of collagen corresponding to the remodeling phase of wound healing. It has been reported that 2–3 days after wound infliction, collagen is deposited [136]. This is randomly oriented initially and becomes reoriented in an orderly fashion during the late granulation stage [133]. In some regions, higher birefringence than that of normal skin was also observed, suggesting an increase in collagen synthesis. Previous studies have shown that the collagen content increases during early wound repair, peaks around 2–3 weeks after injury and returns to the preinjury morphology over a longer period [115]. Concurrent with these dermal changes, on day 10, the reepithelialization was almost complete and was in agreement with the histology (Figure 6.3; i). The results presented in this study showed that the structural changes associated with the healing of

infected wounds were different as compared with the uninfected wounded tissue. Unlike the uninfected wounds, infected wound tissue showed persistence of inflammation and edema on day 10 even when the bacterial count was negligible after day 4. It may also be noted that in the uninfected wound, the reepithelialization and granulation started around day 4, but in the infected wound, both the processes were delayed almost by a week. The lower phase retardation value (Figure 6.5) and the higher imaging depth observed on day 10 in the infected wound in comparison with that of the uninfected counterpart are suggestive of a degraded collagen matrix and a delay in the collagen remodelling phase. Our real-time OCT images (Figure 6.6) also showed kinetics of wound healing under *in-vivo* conditions that had features like edema and reepithelialization similar to that observed in resected tissue using PS-OCT. Our OCT results also showed that even in the epidermal wounds generated by tape stripping, the collagen morphology was disturbed, which was repaired during the healing process. The appearance of epidermal invaginations observed in the epithelial layer of wounded skin during the healing process in the histology images confirms the renewal of hair follicle growth. This observation shows that the dermis and the dermal appendages were recycled during the repair of epidermal wound healing. These results are in agreement with the epidermal wound healing reported by Sugata *et al*. [137], wherein they have shown the involvement of dermal papilla in the restoration of the epidermal layer using confocal microscopy.

6.7 Summary

PSOCT imaging was used to monitor the differences in the morphological and birefringence changes in resected tissues from bacteria-infected and uninfected wounds. The observed results have been validated by histological studies. A real-time OCT was

also used to monitor the progress of healing during infection in a single animal. This imaging technique can provide a rapid assessment of morphological changes, thereby facilitating timely treatment planning.

CHAPTER 7: REFRACTIVE INDEX MEASUREMENTS WITH COMMON PATH PHASE SENSITIVE FDOCT SETUP

Abstract: In this chapter we describe the use of a common path phase sensitive FDOCT set up. The phase measurements of interference spectrum fringes, acquired with common path FDOCT setup, were used to achieve optical path length measurements with resolution of ~2 nm. The setup has been used for the measurement of refractive index of biomimetic materials (glucose solution in water having intralipid as the scattering medium) and single biological cells (keratinocyte).

7.1 Introduction

There has been considerable interest in the use of interferometric techniques for in situ measurement of the refractive index of the biomaterials [72,138]. Since the resolution of the OPL measured by a standard OCT setup is limited to the coherence length of the source (i.e. a few micrometer) the accuracy of refractive index measurement by this approach for an imaging depth of a few mm is limited to ~ 10^{-3} [72]. To further improve the accuracy of the refractive index measurements the resolution with which OPL can be

measured needs to be improved. This can be done if phase information is retrieved in addition to the measurement of the amplitude of the interference fringes [139]. In a typical time domain OCT setup, which involves scanning of the reference arm for depth imaging, precise phase measurements are made difficult due to the considerable phase jitter induced by vibration and noise generated due to the scanning process. Much improved phase stability is obtained in Fourier domain optical coherence tomography setups as these do not require reference arm scanning for depth ranging [140]. This also makes common path configuration easy to implement in the FDOCT approach. Indeed Choma *et al.* used a common path FDOCT setup to demonstrate picometer level OPL measurements by retrieval of phase information of the interferometric signal [141]. However, the OPL measurement range of their technique was restricted to one half of the source wavelength owing to the 2π ambiguity. In order to measure a larger OPL, the measured phase needs to be unwrapped which requires that either the phase shifts gradually or a mechanism like synthesizing the beat frequency needs to be used to account for the 2π ambiguity [142]. Zhang *et al*. have successfully demonstrated phase unwrapping by incorporating the phase retrieval in spectral domain (wavenumber space) instead of depth domain [143]. Unlike depth domain where the phase changes discontinuously, the phase varies gradually in wavenumber space. Since the approach demonstrated by Zhang *et al*. can measure large OPL with high precision it is well suited for the measurement of the refractive index of the biomaterials.

In this chapter, we describe the utilization of a common path FDOCT setup for the measurement of the refractive index of a biomimetic material (glucose solution in water having intralipid as the scattering medium) and a single biological cell (keratinocyte).

7.2 Common path FDOCT system

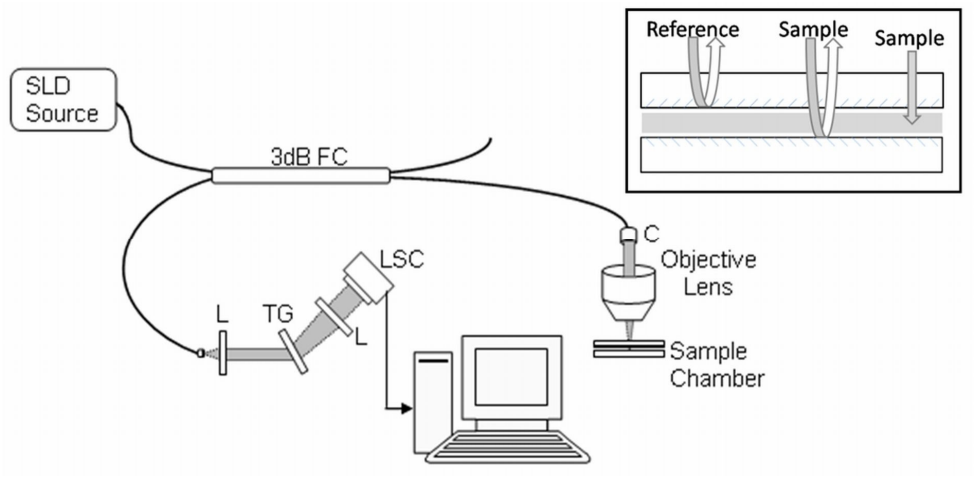

Figure 7.1: Schematic of the common path spectral domain interferometer. SLD, FC, C, L, TG, LSC are the abbreviations for superluminescent diode, fiber-optic coupler, collimating lens, lens, transmission grating and line scan camera respectively. Inset picture shows the sample chamber along with the paths of interfering (reference and sample) beams.

A schematic diagram of the common path FDOCT setup, which is modified version of the FDOCT setup described in chapter 3, is shown in Figure 7.1. It employs an SLD operating at 840 nm with ~ 40 nm bandwidth. The output of the SLD was coupled in to a 3 dB fiber coupler. One arm of the coupler is left open while the other arm is used as common path interferometer to eliminate the common mode noises in the sample and the reference light [141]. As shown in the inset of Figure 7.1 the sample chamber itself provides the reference beam required for the interference. Since the technique is depth resolved, the interference arising due to the beam reflected from the different interfaces of the chamber can be easily separated. A 5X microscopic objective (NA: 0.1) was used to focus light on the sample. The back-reflected components of the reference and sample light are coupled back to fiber coupler. In the detection arm, the interferometric signal was acquired using a spectrometer which comprises a transmission grating (1200 lines per mm, Wasatch Photonics), a 150 mm focal length lens (for focusing the diffracted beam) and a

line scan camera (LSC, *Atmel Aviiva*). Since the spectral resolution of the spectrometer used for acquiring the spectrum of the interference fringes was ~ 0.1 nm, the imaging depth is restricted to a value of ~ 2 mm [17]. As the sample chamber used for common path configuration was made of ~ 1.5 mm thick glass plates with a separation of ~ 300 µm, only the interference from the inner surfaces of the sample chamber is within the measurable depth range of the setup. The measured OPL is an average value for the illumination sample area which in our case is estimated to be ~ 25 µm for 5X objective. A low numerical aperture (NA) lens was chosen to have a large depth of field across the sample chamber.

7.2.1 Phase sensitive OPL measurement

The spectral distribution of light at the detector has a sinusoidal interference pattern ($u(k) \propto \cos(2kz)$ where $k=2\pi/\lambda$) superimposed on the broad source spectrum. The phase information of the interferometric fringes can be retrieved using Hilbert transformation, defined as $w(k)=u(k)+iHT\{u(k)\}$ [144]. The phase Φ(k) of the interference signal can be calculated as $\Phi(k) = \tan^{-1}[\mathrm{Im}(w(k)/\mathrm{Re}(w(k))]$. The calculated phase is wrapped and varies between – π to + π. The absolute phase can be recovered by unwrapping the calculated phase as discussed in Ref [145]. The unwrapped phase of a sinusoidal function ($u(k)$) varies linearly and the absolute optical path (z) can be obtained by linear fitting of the Φ-k curve. The slope of the linear fit gives the OPL ($z = \frac{1}{2}\frac{d\Phi}{dk}$) [146]. The OPL thus measured was used as the approximate value to determine the integer reference to remove the 2π ambiguity. More precise value of OPL (z') can be obtained by including the actual phase value along with the phase slope as follows [143,147]

$$z' = \frac{1}{2k}\left[\Phi - 2\pi\,\mathrm{int}\left(\frac{\Phi - 2kz}{2\pi}\right)\right] \tag{7.1}$$

The interference spectra recorded for the empty (solid line) and water filled sample chamber (dash-dot line) are shown in Figure 7.2A and in Figure 7.2B we show the variation of unwrapped phase retrieved using Hilbert transformation for the same. The observed change in the slope of the unwrapped phase versus wave number is due to the optical path difference between the empty and water filled chambers. Inset of Figure 7.2B shows the stability of the measured optical path length of a coverslip (thickness 115 µm) over 100 measurements for a coverslip of thickness 115 µm. The OPL of the coverslip was used to calibrate the system.

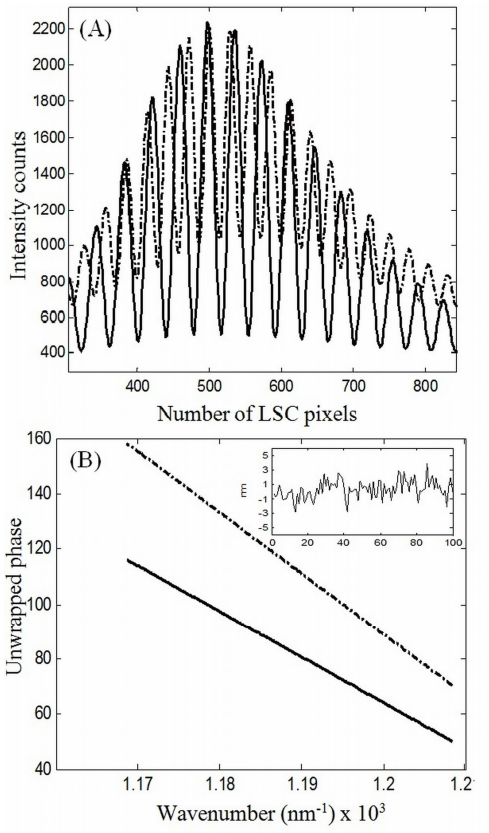

Figure 7.2: (A) The spectral interference fringes are shown for empty (solid line) and water filled (dash-dot line) sample chamber, (B) the unwrapped phase and wave number curve shows change in slope for the empty (black line) and water filled sample chamber (dash-dot line). Inset picture shows the stability of the optical path length (OPL) calculated over 100 measurements for a coverslip of thickness 115 µm.

Figure 7.3 shows a comparison of the fluctuations in the values of OPL measured using a conventional interferometer (where the open arm of the 3 dB fiber coupler was used as reference arm) and with the common path interferometer. As expected in the common path interferometer the fluctuations in OPL are significantly reduced to ~ 2 nm as compared to ~ 4 µm for the conventional dual arm interferometer.

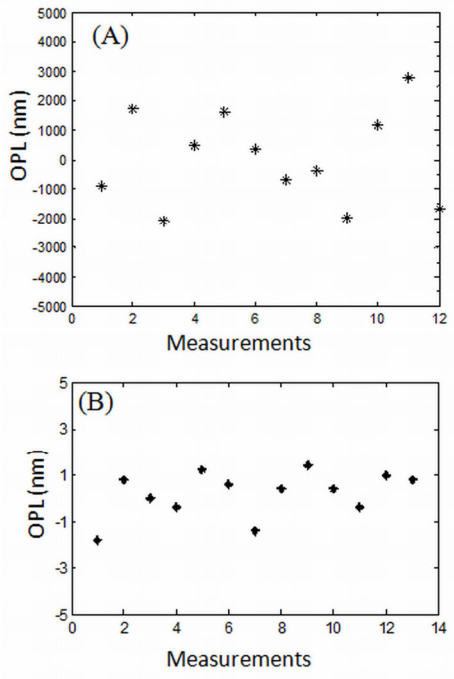

Figure 7.3: Fluctuations in measurements of OPL using (A) separate reference and sample arm and (B) with common path interferometer.

7.2.2 Measurements on coverslips

The setup was used to measure the thickness and the refractive index of a borosilicate glass coverslip. For this, we first measured the optical path lengths of the sample chamber when a coverslip of thickness 115 µm (thickness measured with 1 µm resolution digital micrometer gauge) was placed inside the sample chamber and then the OPL of the empty chamber was measured by carefully removing the coverslip from the sample chamber without disturbing the location of sample chamber. The FFTs of the recorded

interferograms are shown in Figure 7.4. To measure the thickness and the refractive index of the coverslip we need the optical path of coverslip and the change in optical path length of the sample chamber. The peak marked by letter *A* corresponds to the OPL of coverslip while *B* and *B'* are the peaks corresponding to the optical thickness of the sample chamber before and after removing of the coverslip from sample chamber. The other peaks are because of the interference among the reflections of the coverslip and sample chamber interfaces. The optical path lengths corresponding to the coverslip and the chamber were measured by filtering out the undesired peaks using Fourier filtering. Using the measured optical thickness of the coverslip and the change in optical thickness of the sample chamber (before and after removing the coverslip) the refractive index of the coverslip was worked out to be 1.52757 ± 0.00002. It is to be noted that the repeatability obtained in our case is an order of magnitude better than that obtained by Na *et al.* [148] where a self-referencing approach was employed for reducing the noise arising due to the variations in the environmental conditions. In the approach used by us, the use of phase retrieval for higher resolution OPL measurement coupled with the common path interferometry leads to the enhanced repeatability.

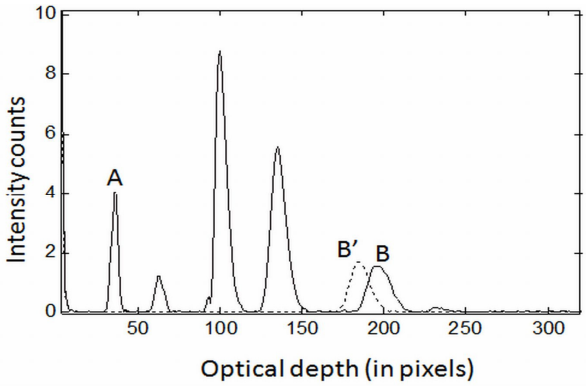

Figure 7.4: FFT of the acquired spectrum before (solid line) and after (dotted line) remove coverslip from the sample chamber. The peak marked by letter A corresponds to the OPL of the coverslip while B and B' are the peaks corresponding to the thickness of the sample chamber before and after removing the coverslip respectively.

7.3 Refractive index sensing of glucose solutions

For refractive index measurements we made a solution of glucose in water. For this, we made 100 mM aqueous solutions of glucose (Sigma-Aldrich chemicals) as a base solution. The different dilutions of the base solution were made to get 0 to 100mM glucose solution. To prepare biomimetic medium, 0 to 100 mM glucose solutions were prepared in 0.5% and 1% of intralipid solutions (Fresenius Kabi Austria GmbH Graz, Austria, 10% dilution).

To measure the RI of glucose solution, the OPLs were measured first with an empty chamber of geometrical thickness *t,* followed by liquid filled chamber to estimate the optical thickness (i.e. $n \times t$). In view of the fact that the glass plates used to make sample chamber may have non-uniform thickness, the OPLs were measured at the same location. The observed changes in RI for different glucose concentrations in water and in two different concentrations of intralipid (0.5% & 1%) are shown in Figure 7.5A and Figure 7.5B respectively. As expected, a linear increase in RI was observed with an increase in concentrations of glucose. The slope of the curve, its intercept and the residuals of the linear fit are tabulated in Table 7.1. From Table 7.1, it can be observed that with the addition of intralipid scattering medium the RI of a given glucose concentration increased. This is because of the presence of glycerol, fat, etc. in intralipid solution. There is no significant variation in the slope of the RI measurement with glucose concentration for the three solutions (water, 0.5% and 1% intralipid solution). With an increase in intralipid concentrations the residual values also increased because the increase in the scattering coefficients in the medium leads to a decrease in the interference signal. The goodness of the linear fit (R-square value) obtained for water, 0.5% and 1% intralipid solution were 0.998, 0.994, 0.988 respectively. The refractive indices of the glucose solutions could be

measured with a standard deviation of ~ 1.5×10^{-4}. The measured slope of the variation of RI with Glucose concentration (2.40×10^{-5}) is reasonably close to the previously reported values of ~ 2.20×10^{-5} [149,150].

Table 7.1: Linear fitting parameters for glucose sensing in water and in intralipid solutions.

Parameters	Water	0.5% Intralipid	1% Intralipid
Slope (dn/dC)	2.4e-5	2.4e-5	2.3e-5
Intercept	1.3366	1.3372	1.3377
Residuals	9.1e-5	1.5e-4	2.2e-4

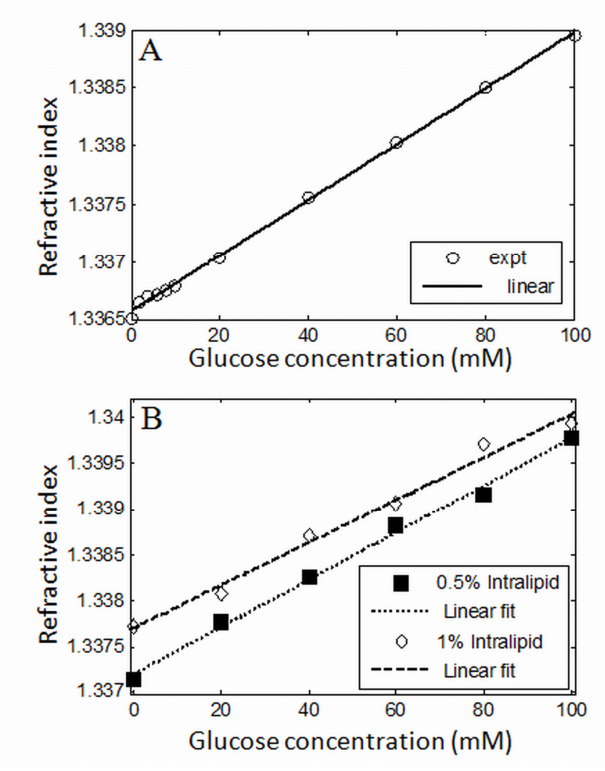

Figure 7.5: The RI data obtained for different concentrations are shown for (A) water (B) 0.5% intralipid (square), and 1% intralipid (diamond). The linear fit to data obtained in water is shown in solid line and that of 0.5% intralipid and 1% intralipid are shown in dotted and dashed lines respectively.

7.3.1 Single cell refractometry

To measure the RI of single cell, we coupled a microscope with the common path phase sensitive interferometer as shown in Figure 7.6. A CCD was placed in the viewing port of the microscope to get the bright field image from the same objective lens with which OCT signal was collected. For cell refractometry experiments, human keratinocyte cells (HaCaT cells, NCCS, Pune, India) were used. These were grown on 35-mm-diameter petridishes in F-12/DMEM (1:1) media supplemented with 10% fetal bovine serum, antibiotics. The cells were incubated at 37 °C in an incubator humidified with 5% CO_2. After 48h, cells were harvested using Trypsin Versene Glucose solution. These cells were suspended in F-12/ DMEM medium (without serum) for using in the experiments.

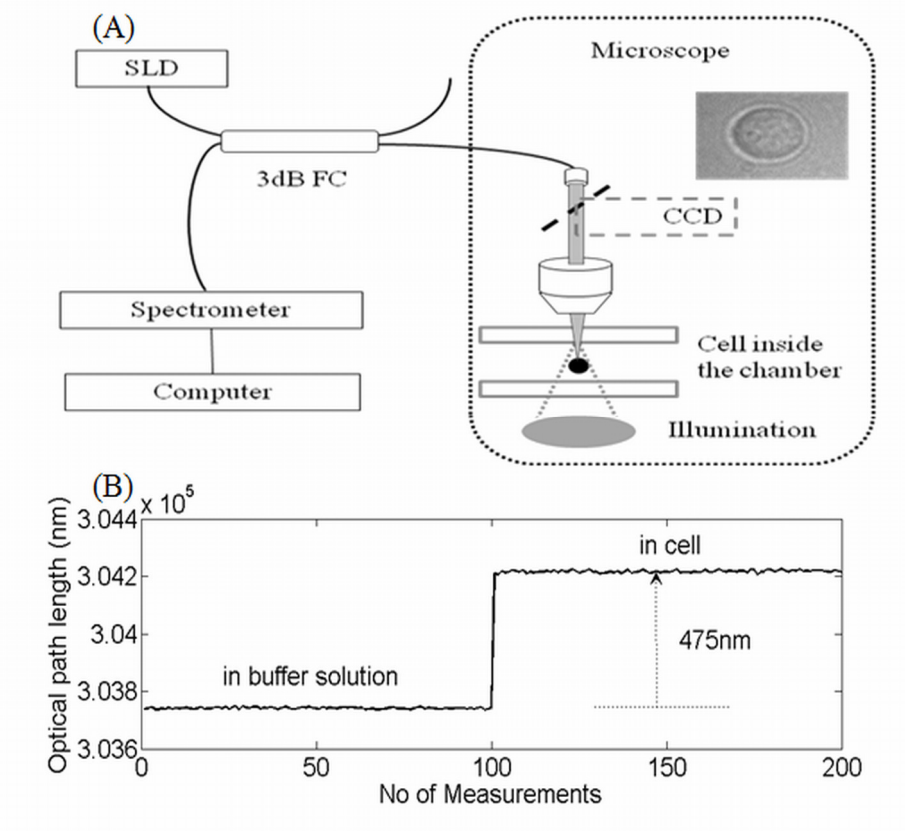

Figure 7.6: (A) The schematic diagram of single cell refractive index measurement setup. (B) The measured change in OPL when light passes through the cell and outside the cell.

Figure 7.6A shows an image of a single keratinocyte cell suspended in cell media, recorded by the CCD camera. For the measurement of RI of single cell we used a 20X objective lens due to the small size of the cell and to take care of the low depth of field for the high NA objective, the chamber thickness was decreased to ~200 µm. The cell diameter (CS) of keratinocyte cells was measured using the bright field CCD image assuming the suspended cells are spherical in shape. In order to measure the RI, we measured the OPLs of the sample chamber when the light passes through the cell (L_c) and outside it (L_s). From these measurements the refractive index of the cell can be derived as

$$n_c = n_s + \frac{(L_c - L_s)}{CS} \tag{7.2}$$

where n_c is the refractive index of the cell, n_s is the refractive index of the cell media. In Figure 7.6B we show the results for the 100 measurements carried out for L_c and L_s for a given cell. The variation in the OPL measurements through cell is ~10 nm (Figure 7.6B) which corresponds to refractive index precision of ~ 4 x10^{-4}. Measurements made on 15 cells gave an average refractive index of keratinocyte cells of 1.38±0.02. This observation is consistent with the results of Rappaz *et al.* [151] where they have used digital holographic microscopy to measure the RI of neuronal cells with a precision of ~3 x10^{-4} but cell to cell variation in RI of ~0.01.

7.4 Conclusions

We have used common path phase sensitive spectral domain optical coherence tomography setup to measure optical path lengths with 2 nm precision. The set up could be used to measure refractive index of a biomimetic material (0 to 100 mM concentration of glucose in water having 0.5% and 1% intralipid as the scattering media) with a repeatability of ~ 0.00015. By coupling the common path interferometer with a

microscope, refractive index of single keratinocyte cell was also measured with a repeatability of ~ 0.0004 As this technique uses broadband SLD light source, it is free from coherent noise associated with the laser light used in digital holography microscopy, which severely reduces the optical quality of the resulting images [152]. Further, in view of its simplicity compared to the digital holography approach it can be easily integrated with micro-fluidic devices and thus may find applications in rapid screening of refractive indices of biological fluids and cells.

CHAPTER 8: SUMMARY

In this thesis we have described the development of OCT setups and their utilization for applications in biomedical imaging like imaging of Zebrafish organs (eye and brain), monitoring of wound healing and discrimination of pathologies of tumour tissues. Towards this objective, we first developed a TDOCT setup. It uses a mechanical scanning reference arm mirror using motorized translation stage for axial or depth scan. Major advantage with this linear translation based scanner is that it facilitates large imaging depth range suitable for imaging transparent samples like eye. The TDOCT setup was used for imaging various ocular structures of Zebrafish eye such as cornea, iris, eye lens and retina. Several ocular parameters such as corneal thickness and retinal thickness were measured from the acquired ocular images. OCT imaging provides direct measurement of optical path length of the light travelled inside the medium. This information was used to estimate the effective or integrated refractive index of the lens for formalin fixed Zebrafish. The study was also extended for *in-vivo* measurement of the refractive index profile of Zebrafish eye lens. The gradient refractive index profile was retrieved by iterative fitting of optical path calculated by ray tracing method with that experimentally measured using OCT. We have also investigated the use of chemically etched tapered fiber and demonstrated the improvement in resolution by visualization of chloroplasts in Elodea densa plant leaf.

The slow imaging speed (~ one minute per image) of the TDOCT setup hampered its use for *in-vivo* imaging of biological tissues. To overcome this, a high-speed OCT system was developed where a rapid scanning FDODL was introduced in reference to achieve scan rates of ~ 4000 scans/s which leads to imaging at 8 frames per second with 500 A-scans per frame. The setup was used for 3D optical imaging of brain with resolution (~20 μm) significantly better than obtained by other techniques like MRI and computed tomography. The setup was also used for monitoring the healing of wounds non-invasively without sacrificing the animal and demonstrated the applicability of the technology for rapid assessment of the wound healing to facilitate timely treatment planning. The high speed image acquisition using resonant scanning FDODL requires large detection bandwidth that compromises the sensitivity of the system. To implement fast image acquisition without significantly compromising the detection sensitivity OCT system based on Fourier domain approach was also developed. This approach eliminates the need for scanning in reference arm and thus facilitates enhanced image acquisition speed with better signal to noise ratio. The FDOCT setup was used to image *in-vivo* samples like skin and nail with 10 frames per second with 1000 A-scans per image. The A-scan rate can further be increased up to ~29 kHz (limited by the read out rate of the LSC) that is sufficient to achieve video rate (32 fps) imaging. The standard OCT setup is only sensitive to the refractive index variation of the tissue. Many biological tissues exhibit birefringence which can modify the polarization state of the incident light. Therefore, we developed a time domain PSOCT setup, which measures orthogonal polarizations of the scattered light, to monitor the birefringent constituents (collagen, tendon, etc.) of the tissue. The PSOCT setup was used for monitoring of collagen remodelling during wound healing progression in the resected tissues of bacterial infected and uninfected mice models. The setup was also used to monitor the changes in the

collagen that take place in malignancy and based on these measurements normal, benign and malignant breast tissue samples were discriminated. Further, OCT based system was also used to measure mechanical properties of breast tissues and significant differences in the stiffness coefficients of normal, benign and malignant tissue were obtained.

In addition to the polarization and elastography information, phase sensitive measurements of OCT interference was also explored. The phase sensitive measurements help to retrieve optical path length changes beyond the restriction of the coherence length of the source. The nanometer scale optical path lengths, obtained using phase sensitive measurements of the interference fringes, were used for the measure of refractive index of biomimetic materials and single biological cell (keratinocyte cells).

The present work can be further extended along the following directions:

We used PSOCT setup for monitoring wound healing. However, for the ease of imaging in a clinical environment, a fiber based high speed PSOCT imaging setup would be better. It will also be interesting to incorporate the Doppler measurements[153] with PSOCT as it would also provide information regarding micro-circulation and angiogenesis of wound healing in addition to the collagen remodelling and morphological changes. Since, formation of new blood vessels is essential for several physiological and pathological events, e.g. embryogenesis, wound healing and tumor growth and metastasis, it would also be a useful tool to visualize the tumor microvasculature and developmental studies on Zebrafish embryos also.

We have used the polarisation sensitive and elastography based measurements with OCT imaging to discriminate the normal, benign and malignant tissue pathologies. Another interesting line of research can be to explore the use of optical contrast agents like nanoparticles to further enhance the diagnostic imaging capabilities of OCT. These

contrast agents may enable site-specific labelling of tissue structures, and thus improve the visualization of early-stage and metastatic tumors and tumor margins to help image-guided surgical resections. Incorporation of the OCT with other imaging modalities such as confocal fluorescence microscopy, laser induced fluorescence, Raman spectroscopy, multi photon microscopy, etc. will also be a worthwhile objective as it will help simultaneous characterization of the 3-D tissue morphology and its biochemical composition [154,155]. These biochemical and morphological information would be useful for fast screening of the normal and diseased tissue at an early stage.

We made use of phase sensitive measurement of the interferometric fringes to measure the refractive index of bio-mimetic materials and single cells. By incorporation of 2D galvo-scanner (for raster scanning of beam) in the setup, it will be possible to measure the two dimensional distribution of the optical path lengths across the biological cells. This would help high resolution imaging of the microscopic objects like cells without staining or affecting them [156]. The studies could be performed to assess the variation in optical path length of the cellular objects affected by different treatments or by the environmental factors such as temperature or pH. It can also be used for label free quantitative and qualitative apoptosis studies which begin with a variety of morphological changes that differs from viable cells.

REFERENCES

1 A. Elliott, “Medical imaging”, Nuclear Instruments and Methods in Physics Research A 546, 1–13, (2005).

2 R. R. Alfano, S. G. Demos, and S. K. Gayen, “Advances in optical imaging of biomedical media”, in Annals of the New York Academy of Sciences 820, 248-271 (1997).

3 J. C. Hebden, S.R. Arridge, D.T. Delpy, “Optical imaging in medicine: 1. Experimental techniques”, Physics in Medicine and Biology 42, 825 – 840 (1997).

4 C. Dunsby and P M W French, “Techniques for depth-resolved imaging through turbid media including coherence-gated imaging”, J. Phys. D: Appl. Phys., 36, R207–R227 (2003).

5 I. W. Rudolph and M. Kempe, “Topical review: trends in optical biomedical imaging”, J. Mod. Opt. 44, 1617-1642 (1997).

6 S. G. Demos and R. R. Alfano, “Optical polarization imaging”, Appl. Opt. 36, 1, 150-155 (1997)

7 V. Cerny, Z. Turek, and R. Parizkova, “Orthogonal Polarization Spectral Imaging”, Physiol. Res. 56: 141-147, (2007).

8 A. F. Fercher, W. Drexler, C. K. Hitzenberger and T. Lasser, “Optical coherence tomography—principles and applications”, Rep. Prog. Phys. 66, 239–303 (2003).

9 P. H. Tomlins and R. K. Wang, “Theory, developments and applications of optical coherence tomography”, J. Phys. D: Appl. Phys. 38, 2519–2535 (2005).

10 D. Huang, E. A. Swanson,C. P. Lin, J. S. Schuman, W. G. Stinson, W. Chang, M. R. Hee, T. Flotte, K. Gregory, C. A. Puliafito, and J. G. Fujimoto, “Optical coherence tomography”, Science 254, 1178-1181 (1991).

11 B. Bouma, and G. Tearne, (Eds.). Handbook of Optical Coherence Tomography. Marcel Dekker, 2002.

12 J. W. Goodman. Statistical Optics. John Wiley and Sons, 1985.

13 G Tearney, M. Brezinski, B. Bouma, S. Boppart, C. Pitris, J. Southern and J. G. Fujimoto, “In vivo endoscopic optical biopsy with optical coherence tomography”, Science 276, 2037–39 (1997).

14 A. G. Podoleanu,“Optical coherence tomography: review” Brit. J. Radiology 78, 976-988 (2005).

15 M. H. Frosz, M. Juhl, M. H. Lang, “Optical Coherence Tomography: System Design and Noise Analysis”, A report of Risø National Laboratory, Roskilde, Denmark, Risø-R-1278(EN), July 2001.

16 R. K. Wang, X. Xu, V. V. Tuchin, and J. B. Elder, “Concurrent en-hancement of imaging depth and contrast for optical coherence tomography by hyperosmotic agents,” J. Opt. Soc. Am. B 18, 7, 948– 953 (2001).

17 R. Leitgeb, C. K. Hitzenberger, and A. F. Fercher, “Performance of Fourier domain vs. time domain optical coherence tomography”,Opt Exp, 11,889-894 (2003).

18 M. A. Choma, M. V. Sarunic, C. Uang, and J. A. Izatt, “Sensitivity advantage of swept source and Fourier domain optical coherence tomography,” Opt. Express 11, 2183-2189 (2003),

19 J. F. de Boer, B. Cense, B.H. Park, M. C. Pierce, G. J. Tearney, and B. E. Bouma, “Improved signal-to noise ratio in spectral-domain compared with time-domain optical coherence tomography,” Opt. Lett. 28, 2067-2069 (2003).

20 M. Wojtkowski, R. Leitgeb, A. Kowalczyk, T. Bajraszewski, and A. F. Fercher, “In vivo human retinal imaging by Fourier domain optical coherence tomography,” J. Biomed. Opt. 7, 457-463 (2002).

21 M. R. Hee and D. Huang, “Polarization-sensitive low-coherence reflectometer for birefringence characterization and ranging”, J. Opt. Soc. Am. B 9, 903-908 (1992).

22 J. F. de Boer, T. E. Milner, M. J. C. van Gemert, and J. S. Nelson, “Two-dimensional birefringence imaging in biological tissue by polarization-sensitive optical coherence tomography”, Opt. Lett. 22, 934-936 (1997).

23 W. Drexler, D. Stamper, C. Jesser, X. Li, C. Pitris, K. Saunders, S. Martin, M. B. Lodge, J. G. Fujimoto, and M. E. Brezinski, “Correlation of collagen organization with polarization sensitive imaging of in vitro cartilage: implications for osteoarthritis”, J. Rheumatol. 28, 1311 (2001).

24 M. C. Pierce, J. Strasswimmer, B. H. Park, B. Cense, and J. F. de Boer, “Birefringence measurements inhuman skin using polarization-sensitive optical coherence tomography”, J. Biomed. Opt. 9, 287 (2004).

25 Y. Chen, L. Otis, D. Piao, and Q. Zhu, “Characterization of dentin, enamel, and carious lesions by a polarization-sensitive optical coherence tomography system”, Appl. Opt. 44, 2041 (2005).

26 Z. Chen, T. E. Milner, D. Dave, and J. S. Nelson, “Optical Doppler tomographic imaging of fluid flow velocity in highly scattering media”, Opt. Lett. 22, 64-66 (1997)

27 Y. Wang, B. A. Bower, J. A. Izatt, O. Tan, D. Huang D., “In-vivo total retinal blood flow measurement by Fourier domain Doppler optical coherence tomography”, J Biomed Opt. 12, 041215 (2007).

28 D. C. Adler, T. H. Ko, P. R. Herz, and J. G. Fujimoto, “Optical coherence tomography contrast enhancement using spectroscopic analysis with spectral autocorrelation”, Opt. Exp 12, 5487-5501 (2004).

29 A. F. Fercher, C. K. Hitzenberger, W. Drexler, G. Kamp and H. Sattmann, “In-vivo optical coherence tomography”, Am. J. Ophthalmol. 116, 113–14 (1993).

30 E. A. Swanson, J. A. Izatt, M. R. Hee, D. Huang, C. P. Lin, J. S. Schuman, C. A. Puliafito and J. G. Fujimoto, “In-vivo retinal imaging by optical coherence tomography”, Opt. Lett. 18, 1864–66 (1993).

31 M. R. Hee, C. A. Puliafito, C. Wong, J. S. Duker, E. Reichel, J. S. Schuman, E. A. Swanson, J. G. Fujimoto, “Optical coherence tomography of macular holes”, Ophthalmology 102, 748 (1995).

32 M.R. Hee, C.R. Baumal, C.A. Puliafito, J.S. Duker, E. Reichel, J.R. Wilkins, J.G. Coker, J.S. Schuman, E.A. Swanson, J.G. Fujimoto, “Optical coherence tomography of age-related macular degeneration and choroidal neovascularisation”, Ophthalmology 103, 1260 (1996).

33 J. Welzel, E. Lankenau, R. Birngruber, R. Engelhardt, “Optical coherence tomography of the human skin”, J Am Acad Dermatol 37, 958-63 (1997).

34 T. Gambichler, G. Moussa, M. Sand, D. Sand, P. Altmeyer, K. Hoffmann, “Applications of optical coherence tomography in dermatology”, Journal of Dermatological Science 40, 85-94 (2005).

35 S. M. Srinivas, J. F. de Boer, B. H. Park, K. Keikhanzadeh, H. L. Huang, “Determination of burn depth by polarization-sensitive optical coherence tomography”, J Biomed Opt 9, 207—12 (2004).

36 V. X. D. Yang, J. Pekar, S. S. W. Lo, M. L. Gordon, B. C. Wilson, A. Vitkin, “Optical coherence and Doppler tomography for monitoring tissue changes induced by laser thermal therapy——an in vivo feasibility study”, Rev Sci Instrum 74, 437—40 (2003).

37 M. E. Brezinski, G. J. Tearney, S. A. Boppart, E. A. Swanson, J. F. Southern, J. G. Fujimoto, “Optical biopsy with optical coherence tomography, feasibility for surgical diagnostics”, J Surg Res 71, 32–40 (1997).

38 S. A. Boppart, B. E. Bouma, C. Pitris, J. F. Southern, M. E. Brezinski, J. G. Fujimoto, “Intraoperative assessment of microsurgery with three-dimensional optical coherence tomography”, Radiology 208, 81–86 (1998).

39 F. I. Feldchtein, G. V. Gelikonov, V. M. Gelikonov, R. V. Kuranov, A. Sergeev, N. D. Gladkova, A. V. Shakhov, N. M. Shakova, L. B. Snopova, A. B. Terenteva, E. V. Zagainova, Y. P. Chumakov, I. A. Kuznetzova , "Endoscopic applications of optical coherence tomography", Opt. Exp. 3, 257 (1998).

40 A. M. Rollins, A. Chak, C. K. Wong, K. Kobayashi, M. V. Sivak, R. Ung-arunyawee, J. A. Izatt, "Real-time in vivo imaging of gastrointestinal ultrastructure using endoscopic optical coherence tomography with a novel efficient interferometer design", Opt. Lett. 24, 1358–1360 (1999).

41 A. F. Fercher and E. Roth, "Ophthalmic laser interferometry", Proc. SPIE 658, 48–51 (1986).

42 Website www.superlumdiodes.com/pdf/sld_overview.pdf

43 J. M. Schmitt "Optical Coherence Tomography (OCT): a review", IEEE J. Sel. Top. Quantum Electron 5, 1205 (1999).

44 P. Hoffmann, B. Dutoit, and R.P. Salathe, "Comparison of mechanically drawn and protection layer chemically etched optical fiber tips", Ultramicr. 61, 165-170 (1995).

45 J. W. Goodman, Introduction to Fourier Optics, (Mc-Graw Hill, NY, 1968).

46 P. Lambelet, A. Sayah, M. Pfeffer, C. Philipona, and F. Marquis-Weible, "Chemically etched fiber tips for near-field optical microscopy: a process for smoother tips", App. Opt. 37, 7289-7292 (1998).

47 R. Stockle, C. Fokas, V. Deckert, R. Zenobi, B. Sick, B. Hecht, and U. P. Wild, "High-quality near-field optical probes by tube etching", Appl. Phys. Lett. 75, 160 (1999).

48 S. Patane, E. Cefali, A. Arena, P.G. Gucciardi, M. Allegrini, “Wide angle near-field optical probes by reverse tube etching”, Ultramicroscopy 106,475–479 (2006).

49 A. Lazarev, N. Fang, Qi Luo, and X. Zhang, “Formation of fine near-field scanning optical microscopy tips. Part I. By static and dynamic chemical etching”, Rev. Sci. Instr. 74, 3679-3683 (2003).

50 R. Dasgupta, S. K. Mohanty, and P. K. Gupta, “Controlled rotation of biological microscopic objects using optical line tweezers”, Biotechnol. Lett. 25, 1625-1628 (2003).

51 C. Fan, Yi. Wang, and R.K. Wang, “Spectral domain polarization sensitive optical coherence tomography achieved by single camera detection”, Opt. Exp, 15, 7950 (2007).

52 E. Collett, Polarized Light: Fundamentals and Applications (New York, Marcel Dekker Inc. 1993).

53 C. K. Hitzenberger, E. Gotzinger, M. Sticker, M. Pircher, and A. F. Fercher, ‘‘Measurement and imaging of birefringence and optic axis orientation by phase resolved polarization sensitive optical coherence tomography,’’ Opt. Exp. 9, 780–790 (2001).

54 J. T. Oh, S.W. Lee, Y.S. Kim, K.B. Suhr, and B.M. Kim, “Quantification of the wound healing using polarization-sensitive optical coherence tomography”, J. Biomed. Opt. 11, 041124 (2006).

55 B. Hyle Park, Mark C. Pierce, Barry Cense, Seok-Hyun Yun, Mircea Mujat, Guillermo J. Tearney, Brett E. Bouma, Johannes F. de Boer, “Real-time fiber-based multi-functional spectral-domain optical coherence tomography at 1.3 μm”, Opt Exp 13, 3931-3944 (2005).

56 E. A. Swanson, D. Huang, M. R. Hee, J. G. Fujimoto, C. P. Lin, C. A. Puliafito, "High-speed optical coherence domain reflectometry", Opt Lett 17, 151–153 (1992).

57 G. J. Tearney, B. E. Bouma, S. A. Boppart, B. Golubovic, E. A. Swanson, and J. G. Fujimoto, "Rapid acquisition of in-vivo biological images by use of optical coherence tomography", Opt. Lett. 21, 1408-1410 (1996).

58 A. M. Rollins, M. D. Kulkarni, S. Yazdanfar, R. Ung-arunyawee and J. A. Izatt, "In vivo video rate optical coherence tomography", Optics Express 3 219-29 (1998).

59 Andrew M. Rollins and Joseph A. Izatt, "Optimal interferometer designs for optical coherence tomography", Opt. Lett. 24, 1484-86 (1999).

60 S. H. Yun, G. J. Tearney, B. E. Bouma, B. H. Park, and J. F. de Boer, "High-speed spectral-domain optical coherence tomography at 1.3 μm wavelength", Opt. Exp. 11, 3598-3604 (2003).

61 M. Wojtkowski, R. Leitgeb, A. Kowalczyk, T. Bajraszewski, and A. F. Fercher, "In vivo human retinal imaging by Fourier domain optical coherence tomography", J. Biomed. Opt. 7, 457–63 (2002).

62 A. S. Glass and R. Dham, "The Zebrafish as model organism for eye development", Ophthalmic Res. 36, 4–24, (2004).

63 R. L. Mayden, K. L. Tang, K. W. Conway, J. Freyhof, S. Chamberlain, M. Haskins, L. Schneider, M. Sudkamp, "Phylogenetic relationships of Danio within the order Cypriniformes: A framework for comparative and evolutionary studies of a model species", Journal of Experimental Zoology Part B: Molecular and Developmental Evolution 308 B**,** 642–54 (2007).

64 C. McMahon, E. V. Semina, and B. A. Link, “Using Zebrafish to study the complex genetics of glaucoma”, Comp. Biochem. Physiol. Part C: Toxicol. Pharmacol. 138, 343–350 (2004).

65 P. Goldsmith, and W. A. Harris, “The Zebrafish as a tool for understanding the biology of visual disorders”, Semin. Cell Dev. Biol. 14, 11–18 (2003).

66 S Kabli, A Alia, H.P.Spaink, FJ Verbeek, HJM De Groot, “Magnetic resonance microscopy of the adult Zebrafish”, Zebrafish, 3, 431 (2006).

67 J. Grush, D. L. G. Noakes and R. D. Moccia, “The efficacy of clove oil as an anesthetic for the Zebrafish, Danio rerio (Hamilton)”, Zebrafish, 46–53 (2004).

68 S. K. Swamynathan, M. A. Crawford, Jr. W. G. Robinson, J. Kanungo, and J. Piatigorsky, “Adaptive differences in the structure and macromolecular compositions of the air and water corneas of the ‘four-eyed’ fish”, FASEB J. 17, 1996–2005 (2003).

69 B. A. Link, M. P. Gray, R. S. Smith, and S. W. M. John, “Intraocular pressure in Zebrafish: comparison of inbred strains and identification of a reduced melanin mutant with raised IOP”, Invest. Ophthalmol. Vis. Sci. 45, 4415–4422 (2004).

70 L. F. Garner, G. Smith, S. Yao, and R. C. Augusteyn, “Gradient refractive index of the crystalline lens of the Black Oreo Dory (Allocyttus niger): comparison of magnetic resonance imaging (MRI) and laser ray-trace methods”, Vision Res. 41, 973–979 (2001).

71 E. Acosta, D. Vazquez, L. Garner, and G. Smith, “Tomographic method for measurement of the gradient refractive index of the crystalline lens. I. The spherical fish lens”, JOSA A 22, 424– 433 (2005).

72 X. Wang, C. Zhang, L. Zhang, L. Xue, and J. Tian, “Simultaneous refractive index and thickness measurements of bio tissue by optical coherence tomography”, J. Biomed. Opt. 7, 628–632 (2002).

73 M. P. Rowe, N. Engheta, Jr. S. S. Easter, and Jr. E. N. Pugh, “Graded-index model of a fish double cone exhibits differential polarization sensitivity”, JOSA A 11, 55–70 (1994).

74 C.E. Jones, D.A. Atchison, R. Meder, J.M. Pope, “Refractive index distribution and optical properties of the isolated human lens measured using magnetic resonance imaging (MRI)”, Vision Res. 45, 2352 (2005)

75 B. K. Pierscionek, A. Belaidi, H. H. Bruun, “Refractive index distribution in the porcine eye lens for 532 nm and 633 nm light”, Eye 19, 375 (2005).

76 D. Vanquez, E. Acosta, G. Smith, L. Garner, “Tomographic method for measurement of the gradient refractive index of the crystalline lens. II. The rotationally symmetrical lens,” J. Opt. Soc. Am. A 23, 2551 (2006).

77 M. K. Suresh, “Studies on Crystalline Lens of Zebrafish Eye Using Optical Coherence Tomography (OCT)”, M. Phil. Thesis submitted to Department of Optoelectronics, University of Kerala, Thiruvananthapuram, India.

78 W.S. Jagger, “The optics of the spherical fish lens”, Vision Res. 32, 1271 (1992).

79 E.W. Marchand, “Axicon gradient lenses”, Appl. Opt. 29, 4001-4002 (1990).

80 A. Sharma, D. Vizia Kumar, A. K. Ghatak, “Tracing rays through graded-index media: a new method”, Appl. Opt. 21, 984-987 (1982).

81 W.S. Jagger, P.J. Sands, “A wide-angle gradient-index optical model of the crystalline lens and eye of the rainbow trout”, Vision Res. 36, 2623-39 (1996).

82 A. Alex, “In VivoBiological Tissue Imaging Using Real-time Optical Coherence Tomography” a project report submitted to Centre of Excellence in Lasers and Optoelectronic Sciences, University of Science and Technology, Cochin, India.

83 B. Rupp, M. F. Wullimann and H. Reichert, “The zebrafish brain: a neuroanatomical comparison with the goldfish**”,** Anat.Embryol.194, 187–203 (1996).

84 www.fishnet.org.au

85 R. J. Bryson-Richardson, S. Berger, T. F. Schilling, T. E. Hall, N. J. Cole, A. J. Gibson, J. Sharpe, and P. D. Currie, BMC Biology5, 34 (2007).

86 R. S. Cotran, V. Kumar, and S. L. Robbins, (1989) Robbins Pathologic Basis of Disease (Saunders, Philadelphia), 4th Ed., pp. 1189, 1195

87 C. Dubessy, J. M. Merlin, C. Marchal, F. Guillemin, “Spheroids in radiobiology and photodynamic therapy”, Crit. Rev. Oncol. Hematol. 36,179-192 (2000).

88 W. Mueller-Klieser, “Tumour biology experimental therapeutics”, Crit. Rev. Oncol. Hematol. 36,123-139 (2000).

89 L. A. Kunz-Schughart, M. Kreutz, and R. Knuechel, “Multicellular spheroids: a three-dimensional in vitro culture system to study tumour biology”, Int. J. Exp. Pathol. 79, 1-23 (1998).

90 B. D. Goldberg, N. V. Iftimia, J. E. Bressner, M. B. Pitman, E. Halpern, B. E. Bouma, G. J. Tearney, “Automated algorithm for differentiation of human breast tissue using low

coherence interferometry for fine needle aspiration biopsy guidance", J. Biomed. Opt. 13, 014014 (2008).

91 C.C. Wu, Y.M. Wang, L.S. Lu, C.W. Sun,C.W. Lu, M.T. Tsai, and C.C. Yang, "Tissue birefringence of hypercholesterolemic rat liver measured with polarization-sensitive optical coherence tomography", J. Biomed. Opt. 12, 064022 (2007).

92 J. F. de Boer, T. E. Milner, "Review of polarization sensitive optical coherence tomography and Stokes vector determination", J. Biomed. Opt. 7, 359 (2002).

93 A. S. Haka, K. E. Peltier, M. Fitzmaurice, J. Crowe, R. R. Dasari, and M. S. Feld, "Diagnosing breast cancer by using Raman spectroscopy", PNAS 102, 12371 (2005).

94 J. M. Schmitt, "OCT elastography: Imaging microscopic deformation and strain of tissue", Opt. Express 3, 199-211 (1998).

95 R. C. Chan, A. H. Chau, W. C. Karl, S. Nadkarni, A. S. Khalil, N. Iftimia, M. Shiskkow, G. J. Tearney, M. R. Kaazempur-Mofrad, and B. E. Bouma, "CT-based arterial elastography: Robust estimation exploiting tissue biomechanics", Opt. Exp. 12, 4558-4572 (2004).

96 A. S. Khalil, R. C. Chan, A. H. Chau, B. E. Bouma, and M. R. Kaazempur-Mofrad, "Tissue elasticity estimation with optical coherence elastography: Toward mechanical characterization of in vivo soft tissue", Ann. Biomed. Eng. 33, 1631-1639 (2005).

97 A. H. Chau, R. C. Chan, M. Shishkov, B. MacNeill, N. Iftima, G. J. Tearney, R. D. Kamm, B. E. Bouma, and M. R. Kaazempur-Mofrad, "Mechanical analysis of atherosclerotic plaques based on optical coherence tomography", Ann Biomed. Eng. 32, 1494-1503 (2004).

98 J. Rogowska, N. A. Patel, J. G. Fujimoto, and M. E. Brezinski, , “Optical coherence tomographic elastography technique for measuring deformation and strain of atherosclerotic tissues”, Heart 90, 556-562 (2004).

99 H. Ko, W. Tan, R. Stack, and S. A. Boppart, “Optical coherence elastography of engineered and developing tissue”, Tissue Engineering 12, 63-73 (2006).

100 T. A. Krouskop T. M. Wheeler , F. Kallel, B. S. Garra, and T. Hall , “Elastic moduli of breast and prostate tissues under compression”, Ultrason. Imaging 20, 260-274 (1998).

101 Y. C. Fung, (1993) Biomechanics: Mechanical properties of living tissues, 2nd Edition, Springer Verlag, NY.

102 A. Manduca, T. E. Oliphant, M. A. Dresner, J. L. Mahowald, S. A Kruse, E. Amromin, J. P. Felmlee, J. F. Greenleaf, and R. L. Ehman, “Magnetic resonance elastography: Non-invasive mapping of tissue elasticity”, Medical Image Analysis 5, 237–254 (2001).

103 J. Lorenzen, R. Sinkus, M. Lorenzen, M. Dargatz, C. Leussler, P. Roschmann, and G. Adam, “MR elastography of the breast: preliminary clinical results”, Rofo. Fortsch.r Geb. Rontgenstr. Neuen Bildgeb. Verfahr 174, 830–834 (2002).

104 A. Samani, J. Zubovits, and D. Plewes, “Elastic moduli of normal and pathological human breast tissues: an inversion-technique-based investigation of 169 samples”, Physics in Medicine and Biology 52, 1565-1576 (2007).

105 R. M. Sutherland , J. A. McCredie and W. R. Inch WR, “Growth of multicellular spheroids in tissue culture as a model of nodular carcinomas”, J. Natl. Cancer Inst. 46, 113-120 (1971).

106 G. Li, K. Satyamoorty, M. Herlyn, “N-cadhrin mediated intercellular interactions promote survival and migration of melanoma cells” Cancer Res. 61, 3819-3825 (2001).

107 H. Dertinger, D. F. Hulser, “Intracellular communication in spheroids”, Recent Results Cancer Res. 95, 67-83 (1984).

108 P. Yu, M. Mustata, L. Peng, J. J. Turek, M. R. Melloch, P. M. French , D. D. Nolte, “Holographic optical coherence imaging of rat osteogenic sarcoma tumor spheroids, Appl. Opt. 43, 4862-4873 (2004).

109 D. Del Duca, T. Werbowetski, R. F. Del Maestro, “Spheroid preparation from hanging drops: characterization of a model of brain tumor invasion”, J. Neurooncol. 67, 295-303 (2004).

110 J. Mobley, and T. Vo-Dinh, (2003) Optical properties of tissue. In: T Vo-Dinh (Ed), Biomedical Photonics Handbook, Boca Raton, FL CRC Press pp. 36

111 E. E. Robinson, K. M. Zazzali, S. A. Corbett, R. A. Foty “ά5β1 integrin mediates strong tissue cohesion”, J. Cell Sci. 116, 377- 386 (2003).

112 H. B. Frieboes, X. Zheng, C. H. Sun, B. Tromberg, R. Gatenby, V. Cristini, “An integrated computational/experimental model of tumor invasion”, Cancer Res. 66, 1597-1604 (2006).

113 M. S. Granick and R. L. Gamelli, Surgical wound healing and management. New York: Informa Healthcare, 2007: 95–96.

114 A. J. Singer,and R. A. Clark, “Cutaneous wound healing”, N Engl J Med 341, 738–746 (1999).

115 J. Li, J. Chen, and R. Kirsner, “Pathophysiology of acute woundhealing”, Clin Dermatol 25, 9–18 (2007).

116 S. Enoch, and D. J. Leaper, “Basic science of wound healing”, Surgery (Oxford) 26, 31–37 (2008).

117 M. S. Kumar, S. Kirubanandan, R. Sripriya, P. K. Sehgal, “Triphala promotes healing of infected full-thickness dermal wound”, J Surg Res 144, 94–101, (2008).

118 N. Cook “Methicillin-resistant Staphylococcus aureus versus the burn patient”, Burns 24, 91–98 (1998).

119 S. A. Grimble, T. R. Magee, R. B. Galland, “Methicillin resistant Staphylococcus aureus in patients undergoing major amputation”, Eur J Vasc Endovasc Surg 22, 215–218 (2001).

120 K. Iwatsuki, O. Yamasaki, S. Morizane, and T. Oono, “Staphylococcal cutaneous infections: invasion, evasion and aggression, a review”, J Dermatol Sci 42, 203–214 (2006).

121 A. B. Wysocki “Wound measurement”, Int J Dermatol, 35, 82–91 (1996).

122 D. H. Keast, C. K. Bowering, A. W. Evans, G. L. Mackean, C. Burrows , and L. D’Souza, “MEASURE: a proposed assessment framework for developing best practice recommendations for wound assessment, a review”, Wound Repair Regen 12, (Suppl.): S1–S17 (2004).

123 A. J. Singer, Z. Wang, S. A. McClain, and Y. Pan, “Optical coherence tomography: a noninvasive method to assess wound reepithelialisation”, Acad Emerg Med 14, 387–391 (2007).

124 J. E. Olerud, G. F. Odland, E. M. Burgess, C. R. Wyss, L. D. Fisher, and F. A. Matsen,III, “A model for the study of wounds in normal elderly adults and patients with peripheral vascular disease or diabetes mellitus”, J Surg Res 59, 349–360 (1995).

125 S. Monstrey, H. Hoeksema, J. Verbelen, A. Pirayesh, P. Blondeel, “Assessment of burn depth and burn wound healing potential”, Burns 34, 761–769 (2008).

126 H. D. Cavanagh, M. S. El-Agha, W. M. Petroll, and J. V. Jester, “Specular microscopy, confocal microscopy, and ultrasound biomicroscopy: diagnostic tools of the past quarter century: review”, Cornea 19, 712–722 (2000).

127 T. H. Helbich, T. P. Roberts, M. D. Rollins, D. M. Shames , K. Turetschek, H. W. Hopf, M. Muhler, T. K. Hunt, and R. C. Brasch, “Noninvasive assessment of wound-healing angiogenesis with contrast-enhanced MRI”, Acad Radiol 9 (Suppl. 1): S145–S147 (2002).

128 J. T. Oh, S. W. Lee, Y. S. Kim, K. B. Suhr, and B. M. Kim, “Quantification of the wound healing using polarization-sensitive optical coherence tomography”, J Biomed Opt 11, 041124–041127 (2006).

129 Z. Metzger, D. Nitzan, S. Pitaru, T. Brosh, and S. Teicher, “The effect of bacterial endotoxin on the early tensile strength of healing in surgical wounds”, J Endod 28, 30–33 (2002).

130 E. Kugelberg, T. Norstrom, T. K. Petersen, T. Duvold, D. I. Andersson, D. Hughes, “Establishment of a Superficial Skin Infection Model in Mice by using Staphylococcus aureus and Streptococcus pyogenes”, Antimicrob Agents Chemother 49, 3435–3441 (2005).

131 P. L. Hsiung, P. R. Nambiar, and J. G. Fujimoto, “Effect of tissue preservation on imaging using ultrahigh resolution optical coherence tomography”, J Biomed Opt 10, 064033–064042 (2005).

132 M. J. Cobb, Y. Chen, R. A. Underwood, M. L. Usui, J. Olerud, X. Li, “Noninvasive assessment of cutaneous wound healing using ultrahigh-resolution optical coherence tomography”, J Biomed Opt 11, 064002–064011 (2006).

133 B. Steffensen, L. Hakkinen, and H. Larjava, “Proteolytic events of wound-healing coordinated interactions among matrix metalloproteinases (MMPs), integrins, and extracellular matrix molecules”, Crit Rev Oral Biol Med12, 373–398 (2001).

134 M. Tomic-Canic, M. S. Agren, O. M. Alvarez, “Epidermal repair and chronic wound”, In: Rovee DT, Maibach HI, eds. Epidermis in wound healing. Boca Raton, FL: CRC Press, 2004: 25–57.

135 M. L. Usui, R. A. Underwood, J. N. Mansbridge, L. A. Muffley, W. G. Carter, and J. E. Olerud, “Orphological evidence for the role of suprabasal keratinocytes in wound reepithelialisation”, Wound Repair Regen13, 468–479 (2005).

136 P. Betz, A. Nerlich, J. Wilske, “The time-dependent rearrangement of the epithelial basement membrane in human skin wounds-immunohistochemical localization of collagen IV and VII”, Int J Legal Med 105, 93–97 (1992).

137 K. Sugata, T. Kitahara, Y. Takema, “Changes of human skin in subepidermal wound healing process”, Skin Res Technol 14, 436–439 (2008).

138 A. M. Zysk, S. G. Adie, J. J. Armstrong, M. S. Leigh, A. Paduch, and D. D. Sampson, F. T. Nguyen and S. A. Boppart, “Needle-based refractive index measurement using low-coherence interferometry”, Opt. Lett. 32, 385-387 (2007).

139 M. Pircher, B. Baumann, E. Götzinger, H. Sattmann, and C. K. Hitzenberger, “Phase contrast coherence microscopy based on transverse scanning”, Opt. Lett. 34, 1750-1752 (2009).

140 C. Joo, T. Akkin, B. Cense, B. H. Park, and J. F. de Boer, “Spectral-domain optical coherence phase microscopy for quantitative phase-contrast imaging”, Opt. Lett. 30, 2131-2133 (2005).

141 M. A. Choma, A. K. Ellerbee, C. Yang, T. L. Creazzo, J. A. Izatt, “Spectral domain phase microscopy”, Opt. Lett. 30, 1162-1164 (2005).

142 C. Yang, A. Wax, R. R. Dasari, and M. S. Feld, “2π ambiguity-free optical distance measurement with subnanometer precision with a novel phase-crossing low coherence interferometer”, Opt. Lett. 27,77-79 (2002).

143 J. Zhang, B. Rao, L. Yu, Z. Chen, "High-dynamic range quantitative phase imaging with spectral domain phase microscopy", Opt. Lett. 34, 3442-3444 (2009).

144 T. Ikeda, G. Popescu, R. R. Dasari, and M. S. Feld, “Hilbert phase microscopy for investigation of fast dynamics in transparent systems”, Opt. Lett. 30, 1165-1167 (2005).

145 M. Takeda, H. Ina and S. Kobayashi, “Fourier-transform method of fringe-pattern analysis for computer-based topography and interferometry”, J. Opt. Soc. Am. 72, 156-160 (1982).

146 S. W. Kim, and S. W. Kim, “Absolute distance measurement by dispersive interferometry using a femtosecond pulse laser”, Opt. Exp. 14, 5954-5960 (2006).

147 S. K. Debnath, M. P. Kothiyal, S. W. Kim, “Evaluation of the spectral phase in spectrally resolved white-light interfrometry: Comparative study of single frame techniques”, Optics and Lasers in engineering 47,1125-1130 (2009).

148 J. Na, H. Y. Choi, E. S. Choi, C. Lee, and B. H. Lee, “Self-referenced spectral interferometry for simultaneous measurements of thickness and refractive index”, App. Opt. 48, 246124-67 (2009).

149 R. O. Esenaliev, K. V. Larin, I. V. Larina, M. Motamedi, “Noninvasive monitoring of glucose concentration with optical coherence tomography”, Opt. Lett. 26, 992-994 (2001).

150 K. V. Larin, T. Akkin, R.O. Esenaliev, M. Motamedi, T. E. Milner, “Phase-sensitive optical low-coherence reflectometry for the detection of analyte concentrations”, App. Opt. 43, 3408-3414 (2004).

151 B. Rappaz, P. Marquet, E. Cuche, Y. Emery, C. Depeursinge, P. Magistretti, “Measurement of the integral refractive index and dynamic cell morphometry of living cells with digital holographic microscopy”, Opt. Exp. 13, 9361-9373 (2005).

152 F. Dubois, L. Joannes, and J. C. Legros “Improved three-dimensional imaging with a digital holography microscope with a source of partial spatial coherence”, App. Opt. 7085-7094 (1999).

153 S. Monstrey, H. Hoeksema, J. Verbelen, A. Pirayesh, P. Blondeel, “Assessment of burn depth and burn wound healing potential”, Burns 34, 761–769 (2008).

154 D. Kang, M. J. Suter, C. Boudoux, P. S. Yachimski, B. E. Bouma, N. S. Nishioka, and G. J. Tearney, "Combined spectrally encoded confocal microscopy and optical frequency domain imaging system," Proc. SPIE 7172, 717206, 717206-7 (2009).

155 L. P. Hariri, E. R. Liebmann, S. L. Marion, P. B. Hoyer, J. R. Davis, M. A. Brewer, and J. K. Barton, "Simultaneous optical coherence tomography and laser induced fluorescence imaging in rat model of ovarian carcinogenesis," Cancer Biol. Ther. 10(5), 438–447 (2010).

156 T. Colomb, F. K. Charrirere, P. Marquet,and C. Depeursinge, "Advantages of digital holographic microscopy for real-time full field absolute phase imaging", In: Three-Dimensional and Multidimensional Microscopy: Image Acquisition and Processing XV. Proceedings of SPIE Volume: 6861, Conchello, J.-A.; Cogswell, C.J.; Wilson,T. & Brown, T.G., (Eds.)